A Measurement of the Cross-section Ratio of the W and Z Muonic Decays and the Total Width of W at $\sqrt{s} = 1.8$ TeV

A Dissertation Presented

by

Ting Hu

to

The Graduate School

in Partial Fulfillment of the Requirements

for the Degree of

Doctor of Philosophy

in

Physics

State University of New York
at
Stony Brook

August 1996

Copyright © by
Ting Hu
1996

State University of New York
at Stony Brook

The Graduate School

Ting Hu

We, the dissertation committee for the above candidate for the Doctor of Philosophy degree, hereby recommend acceptance of the dissertation.

dissertation director
Professor Roderich J. Engelmann
Department of Physics

chairman of defense
Professor Michael Rijssenbeek
Department of Physics

committee member
Professor Jack Smith
Department of Physics

outside member
Professor Darien R. Wood
Department of Physics
Northeastern University

This dissertation is accepted by the Graduate School.

Graduate School

Abstract of the Dissertation

A Measurement of the Cross-section Ratio of the W and Z Muonic Decays and the Total Width of W at $\sqrt{s} = 1.8$ TeV

by

Ting Hu

Doctor of Philosophy

in

Physics

State University of New York at Stony Brook

1996

This thesis describes the $W \to \mu\nu$ and $Z \to \mu\mu$ cross-section analysis for Run 1B (1994-1995) in the DØ experiment. The sample corresponds to a total integrated luminosity of 38.3pb^{-1}. The results are (the errors quoted are statistical errors, systematic errors, and – for cross sections only – the luminosity errors):

$$\begin{aligned} \sigma_W \cdot Br(W \to \mu\nu) &= 2.283 \pm 0.038 \pm 0.160 \pm 0.194 \ \text{nb} \\ \sigma_Z \cdot Br(Z \to \mu\mu) &= 0.198 \pm 0.014 \pm 0.020 \pm 0.016 \ \text{nb} \\ R_\mu &= 11.55 \pm 0.87 \pm 0.81 \end{aligned}$$

Using Standard Model inputs, we further find

$$\begin{aligned} \Gamma(W \to \mu\nu)/\Gamma(W) &= (11.68 \pm 0.49)\% \\ \Gamma(W) &= 1.93 \pm 0.20 \text{ GeV} \end{aligned}$$

This enables us to set an upper limit of 307 MeV on the contribution of the unexpected decays to $\Gamma(W)$ at 95% confidence level.

By comparing our results with the $\sigma_W \cdot Br(W \to e\nu)$ measurement at DØ, we find

$$\frac{g_\mu}{g_e} = 0.979 \pm 0.008 \pm 0.039$$

which is consistent with the lepton universality statement that $g_\mu/g_e = 1$.

To my mom and dad

Contents

List of Figures . . . . . **xv**

List of Tables . . . . . **xviii**

Acknowledgements . . . . . **xix**

1 Introduction **1**

1.1 The Standard Model 1

1.2 W and Z Cross Sections 6

1.3 W and Z Cross Section Ratio 11

1.4 W Total Width 12

1.5 Measurement Scheme 14

2 DØ Detector **16**

2.1 Tevatron 18

2.2 Central Detector 20

2.2.1 Drift Chamber Principles 21

2.2.2 Vertex Detector (VTX) 23

2.2.3 Transition Radiation Detector (TRD) 24

2.2.4 Central Drift Chamber (CDC) 25

2.2.5 Forward Drift Chambers (FDCs) 26

2.3 Calorimeters 28

2.4 Muon Detector 32

2.4.1 Toroids 33

2.4.2 Wide Angle Muon Chambers (WAMUS) 35

2.4.3 Small Angle Muon Chambers (SAMUS) 42

2.5 DØ Trigger and Data Acquisition Systems 43

2.5.1 Level 0 Trigger 43

2.5.2 Level 1 Trigger 45

2.5.3 Level 2 Trigger and Data Acquisition System 48

3 Event Reconstruction 50

3.1 Interaction Vertex 50

3.2 Muon 51

3.2.1 Hit Sorting 52

3.2.2 Track Finding 53

3.2.3 Global Fit 55

3.3 Transverse Missing Energy $\not\!\!E_T$ 58

4 Luminosity 60

4.1 Instantaneous Luminosity 60

4.2 Integrated Luminosity 61

5 Acceptance **64**

5.1 Monte Carlo Event Simulation 65

5.1.1 Event Generator — ISAJET 65

5.1.2 Detector Simulator — DØGEANT 68

5.2 Acceptance 71

5.3 Cuts 72

5.3.1 The Definition of Loose Muon 72

5.3.2 Acceptance Cuts for $W \to \mu\nu$ Events 74

5.3.3 Acceptance Cuts for $Z \to \mu\mu$ Events 76

5.4 Systematic Errors 77

5.4.1 Chamber Efficiencies and Resolutions 77

5.4.2 Parton Distribution Functions 78

5.4.3 W Mass Uncertainty 79

5.4.4 W/Z p_T Distributions 79

5.5 Summary of Acceptance and Errors 80

6 Selection Efficiencies and Trigger Efficiencies **84**

6.1 Reconstruction and Selection Efficiencies 84

6.1.1 Reconstruction Efficiency 85

6.1.2 Selection Efficiency 91

6.2 W/Z Trigger Requirements 104

6.2.1 W Trigger Efficiencies 105

6.2.2 Z Trigger Efficiencies 112

7 Data Samples of $W \to \mu\nu$ and $Z \to \mu\mu$ **116**

8 Background **119**

8.1 W Backgrounds 119

8.1.1 Cosmic Rays and Combinatorics 119

8.1.2 QCD Processes 124

8.1.3 One-legged $Z \to \mu\mu$ 127

8.1.4 $W \to \tau \to \mu$ and $Z \to \tau\tau \to \mu$ 128

8.2 Z Backgrounds 129

8.2.1 Cosmic Rays 130

8.2.2 QCD Processes 130

8.2.3 $Z \to \tau\tau \to \mu\mu$ 131

8.2.4 Drell-Yan Background 131

8.3 Summary of the Background 132

9 Results **134**

9.1 W and Z Cross-sections 134

9.2 R_μ 136

9.3 $\Gamma(W)$ 139

9.4 Lepton Universality 139

9.5 Conclusion 141

A A Note on Least Square Fit **142**

A.1 The Problem 142

A.2 The Solution 144

List of Figures

1.1 W/Z production. The muonic decay diagrams are included here. 7

1.2 Higher order processes: quark gluon scattering, real gluon radiation and gluon vertex correction. 9

2.1 Cutaway view of the DØdetector 17

2.2 The schematic layout of the Tevatron 18

2.3 Central Detector layout. 21

2.4 End view of a Vertex Chamber quadrant. 23

2.5 End view of a Central Drift Chamber section. 25

2.6 Forward Drift Chambers layout. 27

2.7 DØ Calorimeter. 30

2.8 Elevation view of the DØmuon system showing the 5 muon toroids and the A, B and C layers of PDT chambers 33

2.9 Muon System CF toroid. The beamline (not shown) goes through the center of the toroid. The CD and the muon A layer (not shown) are positioned within the toroid, and the muon B and C layer (not shown) are placed outside. 36

2.10 Absorption lengths of calorimeter and muon system as a function of the polar angle. 37

2.11 WAMUS PDT cathode pad structure 38

2.12 WAMUS PDT cell equipotential lines 39

2.13 Assembly of a 3-deck chamber 40

3.1 The sideview of the first top event at DØ. 57

5.1 Data and Monte Carlo η distributions are shown for the EF leg of CF-EF $Z \rightarrow \mu\mu$ events. The top figure is for Monte Carlo events. The bottom one is for the data, where the dark distribution is for the EF muons, the blank distribution is for the overlap muons (not used in this analysis), and the hashed one is for the SAMUS muons(not used in this analysis). . . . 73

5.2 Data(the crosses) and Monte Carlo (the dotted and dash line corresponding to the EARLY and MiDDLE MUSMEAR version respectively) of ϕ distributions are shown for precleaning (top) and postcleaning (bottom) CF data. The precleaning Main Ring hole is not simulated in MUSMEAR. The hole around $\phi = 3.0$ in the postcleaning plot is due to the trigger efficiency drop). 75

5.3 Comparison of the W transverse mass for data and Monte Carlo. The points represent the data. The hashed area shows the contribution of the backgrounds (see Cahpter 8) and the blank area gives the expected signal plus background distribution. The unit for the transverse mass is GeV/c^2. 81

5.4 Comparison of the muon η in the $W \rightarrow \mu\nu$ for data and Monte Carlo (for the CF only). The points represent the data. The hashed area shows the contribution of the backgrounds and the blank area gives the expected signal plus background (see Chapter 8) distribution. 82

5.5 Comparison of the Z invariant mass for data and Monte Carlo. The points represent the data. The hashed area shows the contribution of the backgrounds and the blank area gives the expected signal plus background (see Chapter 8) distribution. The unit for the invariant mass is GeV/c^2. 83

6.1 χ^2 distributions. The top figure is for the signal muons (the other leg in the $Z \rightarrow \mu\mu$ events has to be a "tight" muon). The bottom figure is for the cosmic rays. 92

6.2 $\Delta\theta$ (radians) distributions. The top figure is for the signal muons (the other leg in the $Z \rightarrow \mu\mu$ events has to be a "tight" muon). The bottom figure is for the cosmic rays. 93

6.3 $\Delta\phi$ (radians) distributions. The top figure is for the signal muons (the other leg in the $Z \rightarrow \mu\mu$ events has to be a "tight" muon). The bottom figure is for the cosmic rays. 94

6.4 The bend-view impact parameter (cm) distributions. The top figure is for the signal muons (the other leg in the $Z \rightarrow \mu\mu$ events has to be a "tight" muon). The bottom figure is for the cosmic rays. 95

6.5 The nonbend-view impact parameter (cm) distributions. The top figure is for the signal muons (the other leg in the $Z \rightarrow \mu\mu$ events has to be a "tight" muon). The bottom figure is for the cosmic rays. 96

6.6 The floating time (ns) distributions. The top figure is for the signal muons (the other leg in the $Z \rightarrow \mu\mu$ events has to be a "tight" muon). The bottom figure is for the cosmic rays. . . . 97

6.7 I_μ distributions. The top figure is for the signal muons (the other leg in the $Z \rightarrow \mu\mu$ events has to be a "tight" muon). The bottom figure is for the QCD events. 99

6.8 The halo energy (GeV) distributions. The top figure is for the signal muons (the other leg in the $Z \rightarrow \mu\mu$ events has to be a "tight" muon). The bottom figure is for the QCD events. . . . 100

6.9 Level 1 efficiencies for CF muons for different p_T (GeV/c). The top figure is for pre-cleaning run period, the bottom figure is for post-cleaning run period. 107

6.10 Level 1.5 efficiencies for CF muons for different p_T (GeV/c). The top one is for pre-cleaning run period, the bottom one is for post-cleaning run period. 108

6.11 Level 2 efficiencies for CF muons for different p_T(GeV/c). The top figure is for the pre-cleaning run period, the bottom figure is for the post-cleaning run period. 109

6.12 The $Z \rightarrow \mu\mu$ trigger efficiency versus $\Delta\phi$ (degrees) is shown for CF-CF Monte Carlo events. There is a drop near $\Delta\phi = 180°$. This is caused by the MUCTAG cut removing back-to-back muons. The band is the $Z \rightarrow \mu\mu$ trigger efficiency using the formula (6.2). The solid crosses show the actual efficiencies without the back-to-back cut. The dotted crosses show the efficiencies with the back-to-back cut. 114

7.1 Some kinematic quantities (the crosses are for data, and the histograms are for Monte Carlo simulation. No background – about 20% for W and 10% for Z events – is subtracted). The top figure is the transverse momentum distribution of the muon in the W events, the middle figure is the transverse momentum distribution of the W, and the bottom figure is the transverse momentum distribution of the Z. The unit is GeV/c for all three figures. 117

8.1 The t_f distributions (for the CF only). The top, middle and bottom figures are the sample, signal and background distributions respectively. The unit of t_f is ns. 122

8.2 Fitted results for the distribution (for the CF only). The top figure shows the fit and the sample. The bottom figure shows the data points together with the sum of signal and background (the solid line). The signal (dashed line) coincides the solid line, and the background distribution (dotted line) is barely visible at the bottom. The unit of t_f is ns. 123

8.3 Halo energy distributions (for the CF only). The top figure is for the sample; the middle figure is for the signal muons; the bottom figure is for the background. The unit of the halo energy is GeV. 125

8.4 Fitted results (for the CF only). The top figure shows the fitted results. The bottom figure shows the data points, together with the sum of signal and background (the solid line), the signal (dashed line) is close to the solid line, and the background distribution (dotted line) is visible at the bottom. The unit of the halo energy is GeV. 126

A.1 The width (w_i) distributions for the parameters with the four smallest width for the muon global fit (momentum determination). Note the first plot has a different scale. 146

List of Tables

1.1 Fundamental Fermions in the Standard Model: Quarks 3

1.2 Fundamental Fermions in the Standard Model: Leptons 4

1.3 Gauge Vector Bosons in the Standard Model 5

4.1 4 run periods EARLY, MIDDLE, LATE-MAX and LATE-CENT, and the corresponding integrated luminosities. 63

5.1 The acceptance results for pre-cleaning and post-cleaning periods of run 1B. The errors quoted are, respectively, statistical errors, chamber efficiencies errors, pdf errors, M_W errors and boson p_T spectrum errors. 80

6.1 Efficiencies for scanned good muons passing the standard muon cuts as a function of the MITOOL variable. 90

6.2 Efficiencies for isolation and quality cuts and total selection efficiency for CF and EF muons. 102

6.3 The MITOOL dependence of the WZ tight selection efficiency. 103

6.4 Trigger efficiencies for high p_T CF and EF muons. The definitions of CCT and OTC are discussed in Chapter 2. The "scint" efficiencies are discussed below. 106

6.5 MU_1_MAX trigger efficiencies for high p_T CF and EF muons. The χ^2 per degree of freedom is labelled χ^2/ndf. 110

6.6 Cross-check of unbiased trigger efficiencies using the $Z \rightarrow \mu\mu$ data sample. All values are given in %. 112

6.7 Trigger efficiency corrections for Z events with respect to formula (6.2) using W trigger efficiency. As the back-to-back (BTB) angle cut increases, the correction approaches one. The uncertainty in these numbers is $\pm 2\%$ for Early and Middle MUSMEAR versions, and $\pm 4\%$ for the LATE MUSMEAR version (these are statistical errors of the Monte Carlo calculations). 115

7.1 Number of $W \rightarrow \mu\nu$ events in the final data sample 118

7.2 Number of $Z \rightarrow \mu\mu$ events in the final data sample 118

8.1 W Backgrounds 133

8.2 Z Backgrounds 133

9.1 Cross-sections times the muonic branching ratio (in nb) for W and Z events where there was a good CF muon trigger. The errors are statistical only; the systematic error for each individual entry is typically 10%. 135

9.2 Sources of errors for the W and Z cross-section calculations and the error after the cancelation in the ratio. The systematic error is the quadratic sum of the five terms listed above in the table, but does not include the luminosity error. 137

Acknowledgements

I wish to thank my advisor, Rod Engelmann (Stony Brook), for his guidance and support. His guidance has a profound impact on my career, waking me up from the ivory tower of the physics textbooks and introducing me to the real world. His support at many crucial moments helped me go through hard times. I will forever treasure the time I spent with him.

I wish to thank Daria Zieminska (Indiana University). She gave me much help, especially in my early days at DØ when I needed it most. I feel I can always count on her help and support.

I wish to thank Darien Wood (Northeastern University) and Paul Quintas (Fermilab). Darien and Paul not only have true understanding in the physics but also have extensive knowledge of the DØ detector down to the last details. They are the kind of people who get things done. It was really enjoyable to work with them who seemed to have answers to all my questions.

I wish to thank Tom Trippe (Lawrence Berkeley Laboratory), Michael Rijssenbeek (Stony Brook) and Marc Baarmand (Stony Brook). I began to appreciate the true meaning of "experts" from them. Tom's deep understanding and sharp instinct in statistics helped me greatly in the muon global fit

project and inspired my interest in statistics. Michael helped me learn the electronics with his genuine expertise. He also gave me valuable insights on the methodology of the scientific research. Marc directed my first project in High Energy Physics and I thank him for bring me into this field.

I wish to thank all the members of the DØ collaboration. I have received assistance from so many of them that it is impossible to list all: the Stony Brook members who answered tons of my questions, the members in the muon, the B and the W/Z group who helped me learn the muon system and W/Z physics, the members from the FNAL computing division who helped me learn advanced subjects in computer science, and countless experts who helped me in many aspects.

I wish to thank Fermilab for providing a superb research environment. From the outstanding theorists to the extremely helpful librarians, they all help to make Fermi National Accelerator Laboratory a first-class lab in the world.

Finally I wish to thank my father Zhenggong Hu and my mother Kuiling Ding, for everything. This thesis is dedicated to them.

Chapter 1

Introduction

In this chapter, we first discuss the Standard Model which is the theoretical frame underlying the analysis described in this thesis, then we move on to the theoretical issues directly related to the analysis.

1.1 The Standard Model

The currently most successful theory for the phenomenology of high energy particle interactions is the "Standard Model". Not only it is mathematically and conceptually beautiful, but also its predictions match very well with the experimental observations since its introduction in the late 1960's[1][2][3]. The first experimental confirmation is the observation of neutral weak currents in a CERN neutrino beam in 1973[4]. The more direct confirmation is the discovery of the W and Z boson in the experiments at CERN[5][7][6][8] in 1983.

The Standard Model is a Lagrangian Quantum Field Theory. It is based

upon the idea of local gauge invariance. The gauge symmetry group of the Standard Model is $SU(3)_C \times SU(2)_L \times U(1)_Y$. $SU(3)_C$ is the symmetry group describing the strong interactions, and $SU(2)_L \times U(1)_Y$ is the symmetry group describing the weak and electromagnetic interactions.

The Standard Model uses spontaneous symmetry breaking as a mechanism to introduce masses for the mediators of the forces. The spontaneous symmetry breaking of the $SU(2)_L \times U(1)_Y$ group is due to a scalar Higgs boson, which gives mass to the carriers of the weak force($W^{\pm}$ and Z bosons) and keeps the photon massless. The Higgs boson has not been directly observed yet.

The Standard Model interprets the excitations in the fields as particles, and each separate field corresponds to a different type (or flavor) of particle. The particle content of the model may be divided into 2 groups: the fundamental fermions (spin $\frac{1}{2}$) and the gauge vector bosons (spin 1).

The fundamental fermions consist of quarks and leptons:

- The quarks: there are 6 different flavors of quarks: up(u), down(d), charm(c), strange(s), top(t), and bottom(b). Each flavor of quark has an internal degree of freedom called color. There are 3 possible color states. The quarks can be grouped into 3 generations: (u,d), (c,s) and (t,b). The corresponding particles in each generation have similar properties, except that the masses increase with each successive generation. Table 1.1[11] shows the properties of the quarks (the top quark is simultaneously declared discovered by both the CDF and DØ collaboration

Quark	Mass (MeV/c^2)	Charge(e)
u	2–8	2/3
d	5–15	$-1/3$
c	1.0 GeV/c^2–1.6 GeV/c^2	2/3
s	100–300	$-1/3$
t	174 GeV/c^2–199 GeV/c^2	2/3
b	4.1 GeV/c^2–4.5 GeV/c^2	$-1/3$

Table 1.1: Fundamental Fermions in the Standard Model: Quarks

at Fermilab in 1995[9][10]).

- The leptons: there are 6 different leptons: electron(e), muon(μ), and tau(τ), and their corresponding neutrinos ν_e, ν_μ, ν_τ. The leptons can also be grouped into 3 generations: (e,ν_e), (μ, ν_μ) and (τ, ν_τ). The corresponding particles in each generation have similar properties, except that the masses increase with each successive generation. Table 1.2[11] shows the properties of the leptons.

The gauge vector bosons are the mediator of the forces between the fundamental fermions and gauge vector bosons themselves. The gauge vector bosons consist of the photon(γ), $W^{\pm}$, Z and gluons(g):

- The photon(γ) is the mediator of electromagnetic interaction. It couples to charged particles. The coupling has a running coupling strength, which increases when the energy involved in the interaction increases. Since the photon is massless, the electromagnetic interaction is long

Lepton	Mass (MeV/c^2)	Charge(e)
e	0.511	-1
ν_e	$< 7eV$	0
μ	105.7	-1
ν_μ	< 0.27	0
τ	1777	-1
ν_τ	< 31	0

Table 1.2: Fundamental Fermions in the Standard Model: Leptons

range. The theory section in the Standard Model describing the electromagnetic interaction is Quantum Electrodynamics(QED).

- The $W^\pm$, Z are the mediators of weak interactions. Since $W^\pm$, Z are very massive, the weak interaction is short range($\sim 10^{-18}$m). In the Standard Model, the theoretical description of the weak interaction is unified with that of the electromagnetic interaction in the Glashow-Weinberg-Salam Model[1][2][3], and these two interactions are called electroweak interaction.

- The gluons are the mediators of the strong interaction. There are 8 kinds of gluons, each with additional color freedom. They couple to colored particles which are quarks and gluons themselves. The coupling has a running coupling strength (parameterized by the strong coupling constant α_s), which decreases when the energy involved in the interaction increases. The theory section in the Standard Model describing the

Gauge Boson	Charge	Mass (GeV/c^2)
gluons	0	0
γ	0	0
$W^{\pm}$	± 1	80.22
Z^0	0	91.18

Table 1.3: Gauge Vector Bosons in the Standard Model

strong interaction is Quantum Chromodynamics(QCD).

Table 1.3[11] shows the properties of the gauge vector bosons.

In the context of $p\bar{p}$ collisions, the parton model[12] is used. The parton model simply assumes that the collision between high energy proton and anti-proton can be described as a collision (hard scattering) between a single parton (quark or gluon) in the proton and a single parton in the anti-proton, plus the hadronizing (fragmentation) of the spectators (the leftover partons which do not participate in the initial hard scattering process). The assumption can be justified if the time scale of the hard scattering is much shorter than the time scale of the interaction of the parton with all the other partons, and therefore the scattered parton is essentially free. One important function which characterizes the proton stucture is the parton distributuion function(pdf) $G_{a/A}(x)$. It describes the probability density of finding parton a in the proton A with a momentum fraction x. We will discuss the pdf and the parton model in more details in Chapter 5.

1.2 W and Z Cross Sections

The Z boson properties have been measured to great precision at LEP[11], placing strong constraints on the existence of new particles produced in neutral weak decays. Our knowledge of the W boson is less precise. Currently the best information on properties of the W comes from hadron collider data. One of the most fundamental measurements is that of production cross sections. The cross sections times leptonic branching ratios of W and Z bosons, $\sigma \cdot B(W \rightarrow \mu\nu)$ and $\sigma \cdot B(Z \rightarrow \mu\mu)$, are tightly constrained in the Standard Model. They are predicted by the theory of electroweak interactions, combined with QCD and our knowledge of parton distribution functions(pdf).

In high-energy $p\bar{p}$ collisions, in lowest order the W's and Z's are produced through the Drell-Yan process [13], with quark-antiquark annihilation as the dominant amplitude (Fig. 1.1):

$$q\bar{q}' \rightarrow W(Z)$$

Since the cross section measurement described in this thesis does not make any requirements on the jets or transverse momentum of the W and Z, we are actually integrating over all orders of QCD processes, instead of using only the lowest order process above. The differential cross section for W production as a function of the rapidity y[1] can be expressed in terms of the Cabibbo angle

[1] The rapidity y is defined as $\frac{1}{2} ln \frac{E+p_z}{E-p_z}$.

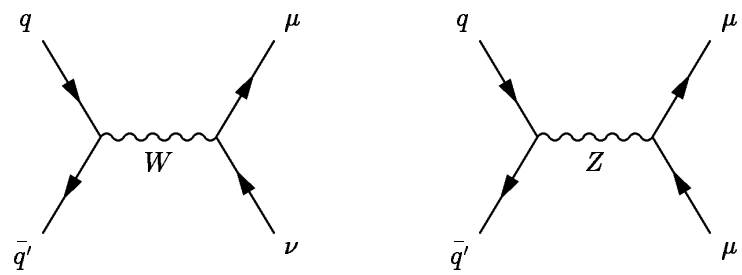

Figure 1.1: W/Z production. The muonic decay diagrams are included here.

θ_C[2], the Fermi coupling Constant G_F[21], and the quark distribution function for u, d and s quarks [14]:

$$\begin{aligned} \frac{d\sigma}{dy}(p\bar{p} \rightarrow W + X) &= K(y) \times \frac{2\pi G_F}{3\sqrt{2}} \times x_1 x_2 \times \\ (cos^2\theta_C[u(x_1)d(x_2) + \bar{d}(x_1)\bar{u}(x_2)] &+ sin^2\theta_C[u(x_1)s(x_2) + \bar{s}(x_1)\bar{u}(x_2)]) \end{aligned}$$

[2]The Cabibbo angle θ_C is a parameter describing d-s quark mixing[21].

where

$$x_1 = \frac{M_W}{\sqrt{s}} e^y, \qquad x_2 = \frac{M_W}{\sqrt{s}} e^{-y}$$

and $W + X$ denote inclusive W production (W plus anything).

The $K(y)$ factor approximates the corrections due to higher order processes, such as quark gluon scattering, real gluon radiation and gluon vertex correction (Fig. 1.2). The K factor has been calculated to order α_s^2 [17] [18]. The major source of uncertainty in the calculation is due to the choice of parton distribution functions.

Similarly, the differential cross section for Z production as a function of the rapidity y can be expressed in terms of the Glashow-Weinberg angle θ_W[3], the Fermi coupling Constant G_F, and the parton distribution function for u, d and s quarks [14]:

$$\begin{aligned}
\frac{d\sigma}{dy}(p\bar{p} \to Z + X) &= K(y) \times \frac{\pi G_F}{3\sqrt{2}} \times x_1 x_2 \times \\
&\{[1 - \frac{8}{3} sin^2\theta_W + \frac{32}{9} sin^4\theta_W] \cdot [u(x_1)u(x_2) + \bar{u}(x_1)\bar{u}(x_2)] \\
&+ [1 - \frac{4}{3} sin^2\theta_W + \frac{8}{9} sin^4\theta_W] \cdot [d(x_1)d(x_2) + \bar{d}(x_1)\bar{d}(x_2) \\
&+ s(x_1)s(x_2) + \bar{s}(x_1)\bar{s}(x_2)]\}
\end{aligned}$$

where

$$x_1 = \frac{M_Z}{\sqrt{s}} e^y, \qquad x_2 = \frac{M_Z}{\sqrt{s}} e^{-y}$$

and $Z + X$ denote inclusive Z production (Z plus anything).

[3] The Glashow-Weinberg angle θ_W is a parameter in the unified electroweak theory [14].

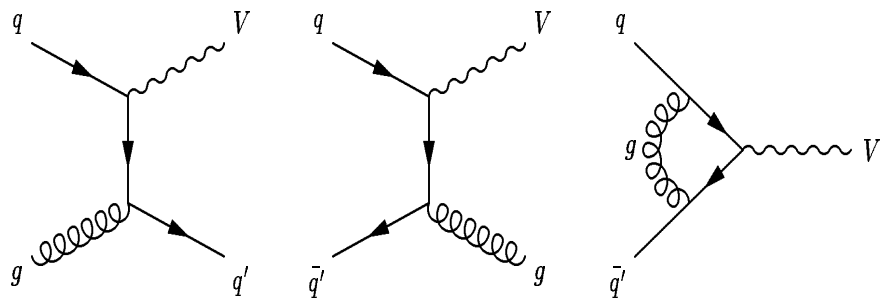

Figure 1.2: Higher order processes: quark gluon scattering, real gluon radiation and gluon vertex correction.

The theoretical predictions of W and Z production cross sections depend on the parton distribution functions, quark-boson couplings, and calculations of the higher order strong interaction corrections to the lowest order processes. The comparison of the measured rates with the predicted rates thus tests aspects of QCD and the electroweak Standard Model.

In addition, the Tevatron (the $p\bar{p}$ collider at Fermilab) provides a chance to study the W and Z cross sections in a unique kinematic regime [14]. At $\sqrt{s} = 1.8$ TeV, the Tevatron is until recently the only collider which produces

on-shell W bosons (LEP[15] will soon be producing on-shell W^+W^-. The first W^+W^- pair is produced on July 10, 1996[16]). The typical x (the fractional momentum of a parton producing a W or Z) is $x \sim \frac{M_{W,Z}}{\sqrt{s}} \sim 0.05$, which means sea quarks are the dominant source of weak bosons. In contrast, the $p\bar{p}$ experiments in CERN took data at $\sqrt{s} = 630$ GeV where the production of W or Z is due mostly to valence quarks.

Since the W and Z decay rapidly, we cannot detect them directly. Instead, we infer the presence of W and Z by detecting their decay products. Most of the W and Z decays are hadronic decays (for W, the branching ratio of hadronic decay is about 2/3; for Z, the branching ratio of hadronic decay is about 7/10), while only a small fraction of the decays are leptonic decays (for W, the branching ratio for leptonic decay is about 1/9, 1/9, 1/9 for $e\nu_e$, $\mu\nu_\mu$, $\tau\nu_\tau$ decays respectively; for Z, the branching ratio for leptonic decay is about 1/30, 1/30, 1/30 for ee, $\mu\mu$, $\tau\tau$ decays respectively). However, due to the large background of strong interaction processes (mostly di-jet processes) in the $p\bar{p}$ collider experiment, we measure the $W(Z)$ cross sections in the lepton decay channels. They provide the cleanest sample of $W(Z)$ bosons in the $p\bar{p}$ collider experiment. This thesis describes the muon channel measurement, $\sigma_W \cdot B(W \to \mu\nu)$ and $\sigma_Z \cdot B(Z \to \mu\mu)$.

By comparing our measurements with the corresponding results in the electron decay channel, we can also test lepton universality. Lepton universality is the statement that the coupling constants for the leptonic weak current are identical for all lepton generations. Lepton universality originates from the local gauge invariance of the electroweak Standard Model, and also the

assumption that there is no mixing among lepton generations. Considering W cross sections only(the Z cross sections suffer from low statistics of the data sample. Also the lepton couplings to the Z are well measured at LEP), the ratio of coupling constants and the ratio of branching fractions are related by [21]:

$$(\frac{g_\mu}{g_e})^2 = \frac{\sigma \cdot B(W \to \mu\nu)}{\sigma \cdot B(W \to e\nu)}$$

where $g_\mu(g_e)$ is the weak coupling constant between W and $\mu(e)$. If the lepton universality holds, then $g_\mu^2 = g_e^2 = 8M_W^2 G_F/\sqrt{2}$. The vector boson decays provide a chance to test lepton universality at large q^2 ($\sim M_{W,Z}^2$).

1.3 W and Z Cross Section Ratio

One of the more interesting numbers we can measure in $W(Z)$ production is the cross section ratio

$$R_\mu = \frac{\sigma \cdot B(W \to \mu\nu)}{\sigma \cdot B(Z \to \mu\mu)}$$

which is less sensitive to higher order QCD correction. Most of the higher order corrections to production cross sections are common to W and Z, canceling when we calculate the cross section ratio. For every diagram producing a W there exists a corresponding diagram producing a Z (up to $O(\alpha_s^2)$ where additional diagrams produce Z's via a triangular quark loop. The $O(\alpha_s^2)$ contributions have been calculated to be less than 1% [14]). For example, in the

W, Z cross section calculation, the first order correction to the Born term is approximately a 20% increase, and the change at the second order is about a 2% increase[29]. However, the cross section ratio only changes by about 1.2% in going from the Born approximation to the second order calculation. The uncertainty in σ_W/σ_Z is dominated by the uncertainty of the ratio of d and u valence quark densities.

From the cross section ratio R_μ, the total width of the W can be obtained.

1.4 W Total Width

The W total width can be expressed as well-defined functions of the basic electroweak parameters. In the electroweak theory, there are 3 free parameters (besides the fermion and higgs masses and the quark mixing angles). The most relevant parameterization for our kinematic regime is M_W(the W mass), G_F (the Fermi constant, measured in muon decay), and α (the electromagnetic fine structure constant). The total width of the W decay can be expressed in the Standard Model as:

$$\begin{aligned}\Gamma(W) &= \frac{G_F M_W^3}{6\pi\sqrt{2}} \cdot [1+\delta(M_{Top}, M_{Higgs})] \cdot [3+6(1+\frac{\alpha_s(M_W)}{\pi})] \\ &= 2.077 \pm 0.014 GeV \quad \text{from theory [26]}\end{aligned}$$

In the above expression, the δ term depends on the top mass and higgs mass, and represents higher order oblique corrections(a class of radiative corrections which occur through loops of new particles in W and Z vertices and

propagators) to $\Gamma(W)$, primarily due to vertex corrections, while the propagator loop corrections are absorbed mostly by the M_W term. The δ term is about -0.35% [26] in the Standard Model with a heavy top quark and a single higgs doublet. The δ term is potentially sensitive to new physics through higher order electroweak corrections to $\Gamma(W)$.

The term containing the strong coupling constant α_s describes the correction to the electroweak calculation due to gluon radiation in lowest order.

The total width of W is sensitive to unobserved decay modes of W, regardless of whether or not they can be detected. The comparison of measured and theoretical values of $\Gamma(W)$ can be used to set an upper limit on the excess width of W, allowed by experiment for non-Standard Model decay processes (such as decays into supersymmetric charginos and neutralinos[24], or into heavy quarks[25]).

The ratio R_μ of $\sigma \cdot B(W \to \mu\nu)$ and $\sigma \cdot B(Z \to \mu\mu)$ can be expressed as:

$$\begin{aligned} R_\mu &= \frac{\sigma \cdot B(W \to \mu\nu)}{\sigma \cdot B(Z \to \mu\mu)} \\ &= \frac{\sigma_W}{\sigma_Z} \cdot \frac{\Gamma(W \to \mu\nu)}{\Gamma(W)} \cdot \frac{\Gamma(Z)}{\Gamma(Z \to \mu\mu)} \end{aligned}$$

Therefore, the measurement of R_μ enables us to calculate $\Gamma(W \to \mu\nu)/\Gamma(W)$, by using the following inputs:

$$\begin{aligned} \frac{\sigma_W}{\sigma_Z} &= 3.33 \pm 0.03 \quad \text{from theory [17]} \\ \Gamma(Z \to \mu\mu)/\Gamma(Z) &= (3.367 \pm 0.006)\% \quad \text{LEP experiment [11]} \end{aligned}$$

If we further assume the Standard Model coupling between W and leptons, we can use the theoretical value $\Gamma(W \rightarrow \mu\nu) = 225.2 \pm 1.5$ MeV[26] and calculate $\Gamma(W)$, the W total width.

The most precise measurement of $\Gamma(W)$ today comes from the $p\bar{p}$ measurements of $R = \frac{\sigma \cdot B(W \rightarrow \ell\nu)}{\sigma \cdot B(Z \rightarrow \ell\ell)}$. A direct measurement, from fitting the tail of the transverse mass spectrum of the W, has been made[28], but is less precise. By measuring $\Gamma(W)$, we test the internal consistency of the electroweak theory and QCD theory.

1.5 Measurement Scheme

The cross section times muonic branching ratio $\sigma \cdot B(W \rightarrow \mu\nu)$ is calculated as ($\sigma \cdot B(Z \rightarrow \mu\mu)$ has a similar formula):

$$\sigma \cdot B(W \rightarrow \mu\nu) \quad = \quad \frac{N_{obs} - N_{bkgd}}{\mathcal{L} \cdot \mathcal{A}_W \cdot \epsilon_W}$$

where N_{obs} is the observed number of candidate events, N_{bkgd} is the calculated number of expected background events, $\mathcal{L}$ is the total integrated luminosity used in the analysis, $\mathcal{A}_W$ is the kinematic and geometric acceptance, ϵ_W is the detection efficiency, including on-line trigger efficiency and off-line selection efficiency.

To calculate the cross section ratio R_μ, we use

$$R_\mu \quad = \quad \frac{\sigma \cdot B(W \rightarrow \mu\nu)}{\sigma \cdot B(Z \rightarrow \mu\mu)}$$

$$= \frac{N_W \mathcal{A}_Z \epsilon_Z}{N_Z \mathcal{A}_W \epsilon_W}$$

where $N_W(N_Z)$ is the number of $W(Z)$ candidates with background subtracted. Note that the luminosity term canceled completely. In addition, part of the systematic errors in the acceptance and detection efficiency also cancel.

Below is the outline of the remainder of this thesis:

Chapter 2, DØ Detector: we will discuss the experimental setup for this analysis, with emphasis on the muon system.

Chapter 3, Event Reconstruction: we will discuss how the various objects in our analysis, such as muons, are reconstructed from data collected by the detector.

Chapter 4-8 we will discuss the details of the analysis, including the measurement of $\mathcal{L}$, $\mathcal{A}_{W/Z}$, $\epsilon_{W/Z}$, and $N_{W/Z}$ and backgrounds.

Chapter 9, Results: based on the analysis described in Chapter 4, we will calculate the W and Z cross section in the muon channel and extract R and $\Gamma(W)$. We will compare our results with other experiments and theory.

Chapter 2

DØ Detector

The DØ detector (Fig. 2.1) is a general purpose particle detector designed to study $p\bar{p}$ collisions at $\sqrt{s} = 1.8$TeV in the Fermilab tevatron collider. It is optimized for the study of physics at large transverse momentum such as electroweak physics, heavy quarks, perturbative QCD physics, and the search for new phenomena beyond the Standard Model.

The DØ detector is 13m high, 11m wide and 17m long. It consists of the Central Detector, the Calorimeters and the Muon Detector. The Central Detector is placed innermost. There is no central magnetic fields, and the energy measurement of particles (except muons) relies on the Calorimeters outside the Central Detector. The calorimeters are thick enough to stop all the particles except muons and neutrinos. Muon detectors are outermost and measure the muon energies by bending in a magnetic field.

The global coordinate system used in DØ is a right-handed corrdinate system, with the $\hat{Z}$ direction the same as the proton direction (southward), and the $\hat{Y}$ direction upward, and $\hat{X}$ direction eastward. Therefore the polar

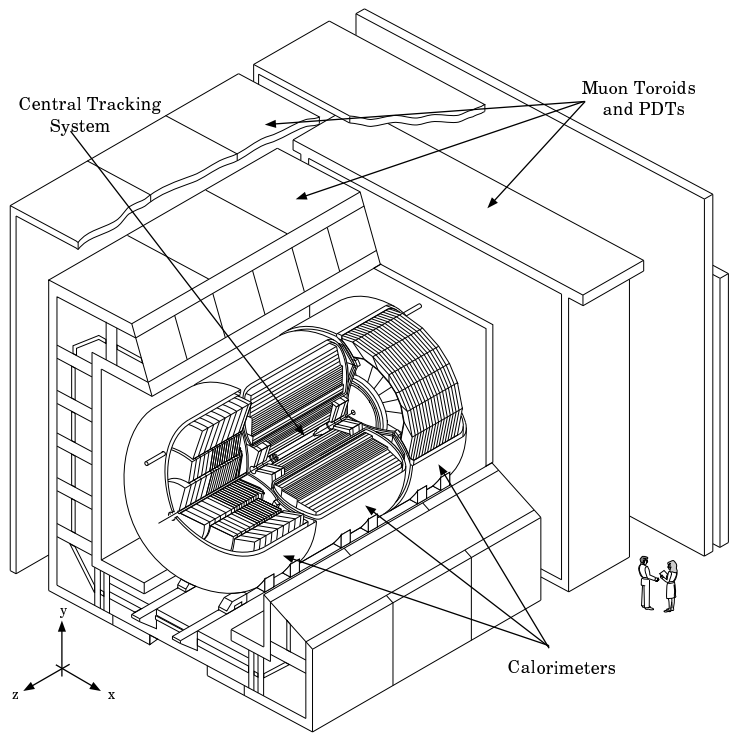

Figure 2.1: Cutaway view of the DØ detector

angle $\theta = 0$ along the proton direction, and the azimuthal angle $\phi = 0$ along the eastward direction. The pseudorapidity $\eta = -ln \tan \frac{\theta}{2}$ is often used to approximate the true rapidity

$$y = \frac{1}{2} ln \frac{E + p_z}{E - p_z}$$

This is a good approximation when the rest mass is much smaller than the energy.

Before discussing the DØ subdetectors, we briefly discuss the Tevatron

which provides the $p\bar{p}$ collisions.

2.1 Tevatron

The Tevatron (Fig. 2.2) accelerates the protons and antiprotons to high energy and steers them to collide at designated points. The two most important parameters of Tevatron are the center of mass energy ($\sqrt{s} = 1.8$Tev) and the instantaneous luminosity (up to $\sim 20 \times 10^{30} cm^{-2} sec^{-1}$).

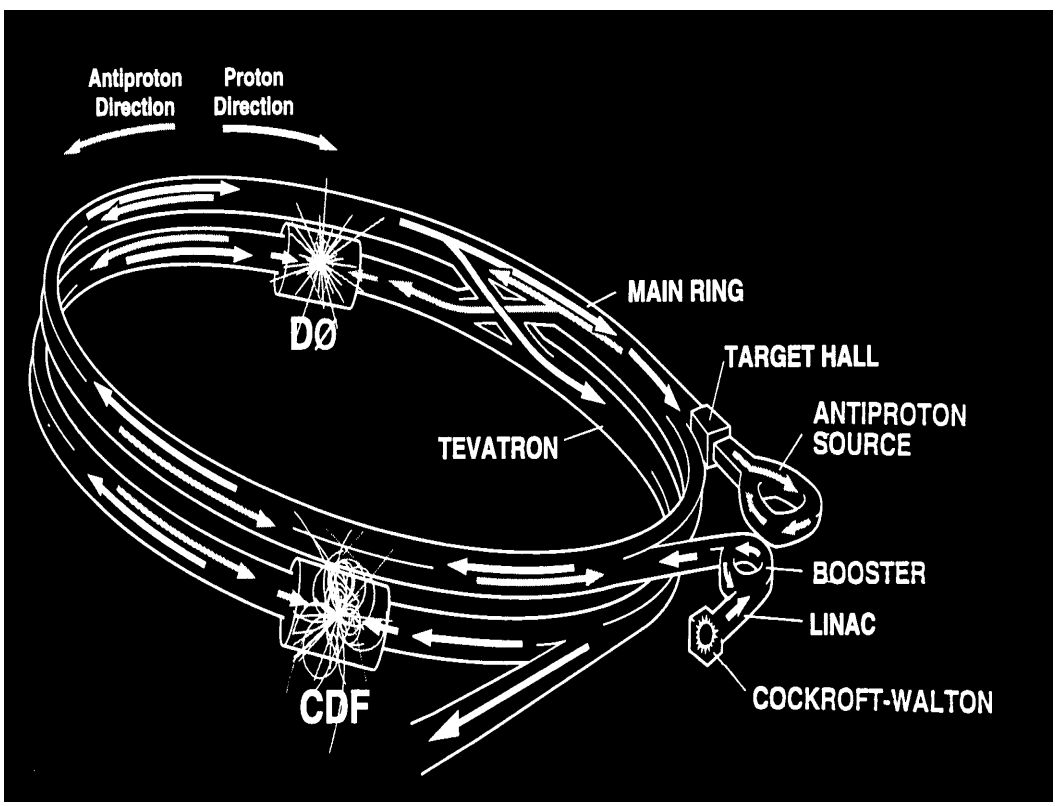

Figure 2.2: The schematic layout of the Tevatron

Below is a brief account of the processes through which the protons and

anti-protons are accelerated[30][36]. The luminosity part will be discussed in a later chapter.

1. The Preaccelerator: Hydrogen atoms are ionized (by passing H_2 gas over a catalytic surface in the presence of free electrons) and are then accelerated to 750KeV in an electrostatic Cockroft-Walton accelerator. The ions are bunched and sent to the Linac.

2. The Linac: the 150 meter long linear accelerator (the Linac) accelerates the Hydrogen ions to 400MeV. When the ions exit from the Linac, electrons are stripped off from them by a carbon foil. The bare protons are sent to the Booster.

3. The Booster: the Booster is a synchrotron ring with 151m diameter. It boosts the protons to 8GeV. The protons are organized into discrete bunches and sent to the Main Ring.

4. The Main Ring: the Main Ring is also a synchrotron ring, but with a radius of 1000m. The Main Ring accelerates the proton bunches to 150GeV. The Main Ring also produces anti-protons by extracting the 120GeV proton beam onto a nickel/copper target. The production rate is about 20 anti-protons with a momentum of about 8 GeV for every 10^6 protons hitting the target. The anti-protons are then debunched and stored in the accumulator ring for later injection back to the Main Ring.

5. The Tevatron: The Tevatron is a proton synchrotron with the same radius as the Main Ring. It lies 25.5 inches below the Main Ring in the

accelerator tunnel. Protons and anti-protons are injected by bunch from the Main Ring into the Tevatron. They occupy the same beam pipe but move in the opposite directions (protons clockwise, anti-protons counter clockwise). The Tevatron accelerates the protons and anti-protons up to 900GeV and steers them to collide in the center of the DØ detector and in the center of the other general purpose particle detector, the Collider Detector Facility (CDF).

2.2 Central Detector

The Central Detector (CD, Fig. 2.3) consists of the Vertex Detector (VTX), the Transition Radiation Detector (TRD), the Central Drift Chamber (CDC), and two Forward Drift Chambers (FDCs). The VTX, TRD, CDC cover the large angle region and are arranged in three cylinders concentric with the beams. the FDCs are oriented perpendicular to the beams. The whole essembly fits within the inner cylindrical aperture of the calorimeters in a volume bounded by a radius r=78cm and z=$\pm$135cm along the beam.

With no central magnetic field and therefore without the need to measure the momentum of charged particles, the prime considerations for tracking were good two-track resolving power, high efficiency and good ionization energy measurement. The CD is responsible for making a precise measurement of the location of the interaction vertices for each event. Precise position measurements are also useful for calibrating the calorimeter shower position measurements and for improving the accuracy of muon momentum measure-

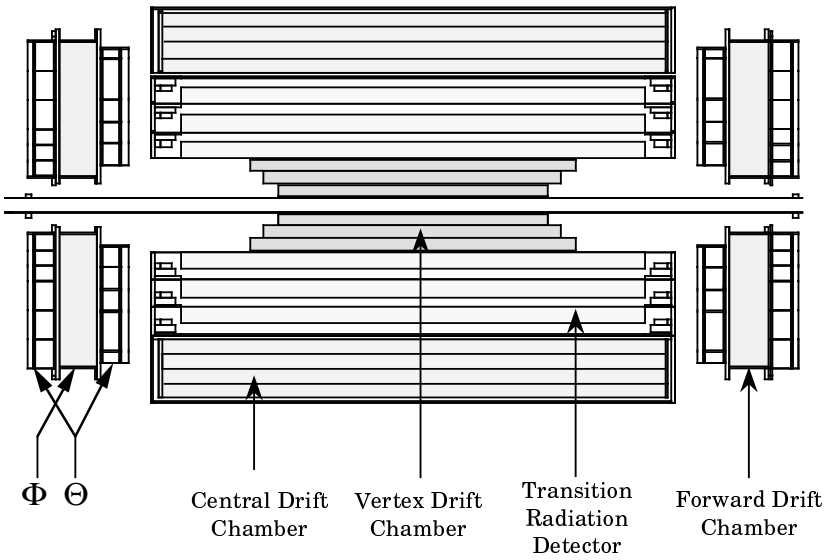

Figure 2.3: Central Detector layout.

ments.

2.2.1 Drift Chamber Principles

Many components of the DØ detector are drift chambers, including the Vertex Detector (VTX), the Central Drift Chamber (CDC), the Forward Drift Chambers (FDC's) and the Muon Detector. Below, we briefly review the drift chamber principles.

When a charged particle passes through a gas, it will interact electro-

magnetically with nearby atomic electrons, creating electron/ion pairs along its path (the number of such pairs created depends on the energy and the charge of the particle and the type of gas, but can typically be on the order of 100/cm). With the presence of a strong enough electric field, the electrons produced will drift through the gas towards the positive electrode (the ions also drift in the opposite direction, but their drift speed is much lower and can be ignored in the following discussion), resulting in repeated collisions with the gas molecules and creating an avalanche. When this avalanche reaches the positive electrode, it creates a measurable current which is proportional to the original number of ions created. The ratio between the final number of electrons collected and the initial number deposited (called the Gas Gain) can be on the order of 10^4 for practical detectors.

The electrons drift with a predictable speed over most of the distance to the anode, implying one can turn a measurement of the time an electron takes to drift to the anode into a measurement of the distance of the original source particle from the anode.

A drift chamber is a device which utilizes the above facts. A strong electric field due to a thin anode wire (typically 20-100μm) is created. A linear relationship between distance and time is achieved by creating the electric field as constant as possible over as large a volume as possible (usually with the help of additional field-shaping electrodes), and also by using the fact that the relationship between electron drift velocity and electric field tends to flatten out for sufficiently large electric fields (typically $10 - 50\mu m/ns$).

The measurement of the size of the anode signal determines the energy

loss density of the traversing particle and can be used for particle identification.

Further information on drift chambers can be found in [32][33].

2.2.2 Vertex Detector (VTX)

The Vertex Detector (VTX) (Fig. 2.4) is the innermost tracking detector in DØ. It has an inner radius of 3.7cm, and an outer radius of 16.2cm. It consists of 3 concentric layers of cells. The innermost layer has a length of 97cm, and each successive layer is about 10cm longer.

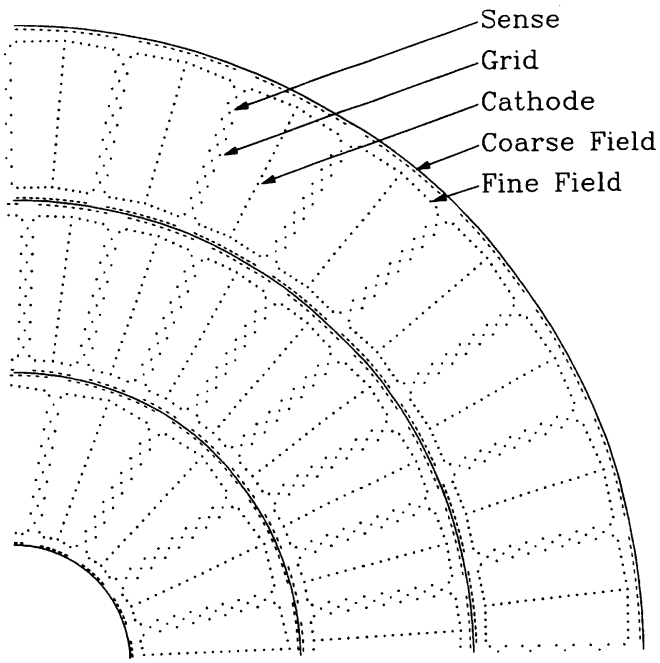

Figure 2.4: End view of a Vertex Chamber quadrant.

The innermost layer has 16 cells in azimuth. The outer two layers have

32 cells each. The 8 sense wires (anode wires) in each cell (there are 640 sense wires in total in the VTX) are arranged in planes which are parallel to the paths of particles emerging from the interaction region (this arrangement is called jet geometry). The wires are 4.57mm separated radially, and are staggered by $\pm 100\mu m$ in azimuth ϕ in order to resolve left-right ambiguities. The cells of the three layers are also offset in ϕ to further aid pattern recognition and facilitate calibration and help eliminating dead regions.

The sense wires provide a measurement of the radius r and azimuth ϕ of a hit (by the drift time and the location of the wire hit), with a resolution of $\sim 60\mu m$. The z-coordinate can be measured from the relative size of the signals on both ends of the VTX sense wires with a resolution of $\sim 1.5cm$.

Further information on VTX can be found in [31].

2.2.3 Transition Radiation Detector (TRD)

Outside the VTX and inside the CDC is the Transition Radiation Detector (TRD). It is a device designed to distinguish electrons from heavier particles. It is based upon the fact that when a charged particle crosses between two materials with different dielectric constants, it radiates in the forward direction, with the radiation intensity proportional to $\gamma = E/(mc^2)$ and concentrated in a cone whose half opening angle is $1/\gamma$. The radiation typically peaks in the X-ray region for large $\gamma(\gamma > 10^3)$. This fact can be utilized to discriminate between particles with similar energies but with different masses.

At the Tevatron, electrons are the only charged particles likely to be

produced with sufficient energy to produce detectable transition radiation. The TRD is used exclusively to identify electrons. The TRD therefore does not directly affect our analysis in the muon channel.

Further information on TRD can be found in [31].

2.2.4 Central Drift Chamber (CDC)

Outside the TRD is the Central Drift Chamber (CDC, Fig. 2.5). It is the outermost tracking detector in the Central Detector. It has an inner radius of 49.5cm, and an outer radius of 74.5cm. It consists of 4 concentric layers of cells. It has a length of 184cm.

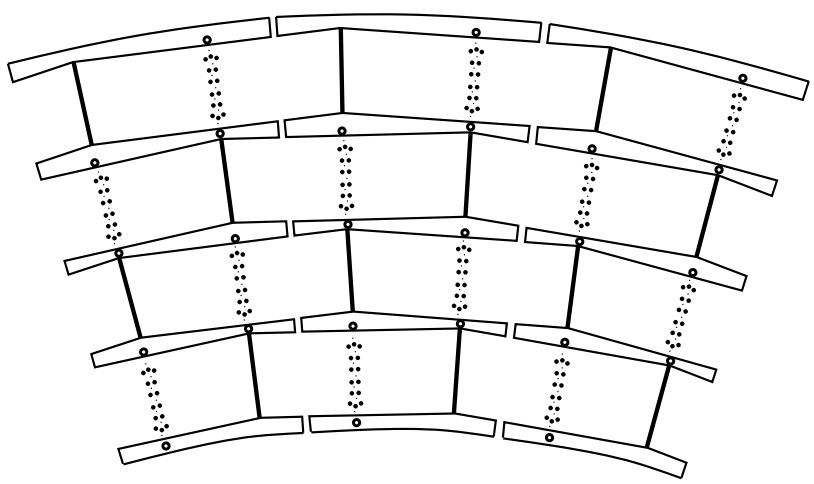

Figure 2.5: End view of a Central Drift Chamber section.

Each layer has 32 cells in azimuth. The 7 sense wires in each cell (there are 896 sense wires in total in CDC) are arranged in jet geometry. The wires are 6.0mm separated radially, and are staggered by $\pm 200\mu m$ in ϕ to resolve

left-right ambiguities. Alternate cells in radius are also offset by half a cell to further aid pattern recognition.

The sense wires provide a measurement of the $r-\phi$ coordinate of a hit (by the drift time and the location of the wire hit), with a resolution of $\sim 180\mu m$. The z-coordinate can be measured by the inductive delay lines embedded in the module walls in the sense wire plane. When an avalanche occurs near an outer sense wire, a pulse is induced in the nearby delay line and propagates with a velocity of about $2.35mm/ns$. By comparing the arrival times of the pulse at both ends, the z position can be determined. This can be done with a resolution of 2.9mm (best case). The CDC has a tracking efficiency of about 89% for isolated tracks.

Further information on CDC can be found in [31].

2.2.5 Forward Drift Chambers (FDCs)

The Forward Drift Chambers (FDCs, Fig. 2.6) extend the coverage for charged particles tracking down to a polar angle $\theta \sim 5°(\eta \approx 3.1)$. The FDCs consist of two sets of FDC chambers, locating at either end of the concentric barrels of the VTX, TRD, CDC, and just before the entrance wall of the end calorimeters. Each FDC consists of three layers of chambers: two Θ layers sandwiching one Φ layer. These layers have an inner radius of 11cm, and an outer radius of 62cm (61.3cm for the Φ layer). The Θ layers extend in $|z|$ from 104.8cm to 111.2cm, and from 128.8cm to 135.2cm. The Φ layer extends in $|z|$ from 113.0cm to 127.0cm.

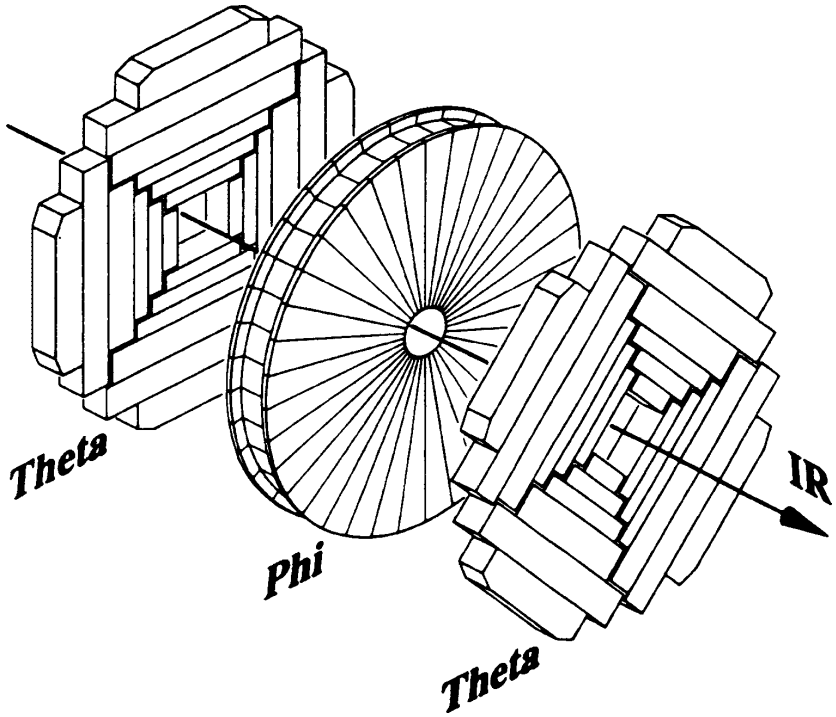

Figure 2.6: Forward Drift Chambers layout.

Each Θ layer has 4 quadrants, each composed of 6 rectangular drift cells at increasing radii. The 8 wires in each cell (there are 192 sense wires in total in each FDC Θ layer) are oriented in a plane parallel to the z-axis and normal to the radial direction. The inner three cells are half cells in which the wires are placed at the edge of the cell; thus the electrons can drift in only one direction. The wires are 8.0mm separated radially, and are staggered by $\pm 200\mu m$. Each Θ cell also contains a delay line to measure the position along the length of the cell. The upstream and downstream Θ chambers are rotated relative to each other by an angle of $\pi/4$.

Each Φ layer has 36 cells in azimuth. The 16 sense wires in each cell (there are 576 sense wires in total in each FDC Φ layer) are arranged in a plane containing the beam line. The wires are 8.0mm separated radially, and are staggered by $\pm 200\mu m$. There are no delay lines in the Φ layer.

The drift resolution is about $300\mu m$ for the Θ layer, and about $200\mu m$ for the Φ layer. The FDC has a tracking efficiency of about 85% for isolated tracks.

Further information on the FDC can be found in [31].

2.3 Calorimeters

DØ has no central magnetic field, the Calorimeters provide the only available measurement of the energy of particles (except for muons).

Calorimeters stop particles and measure the amount of kinetic energy deposited by the particles, via the following two processes: Electromagnetic Shower and Hadronic Shower.

- Electromagnetic Shower: when a high-energy ($\gg$ 10MeV) electron passes through a material with a high atomic number, it loses energy primarily through the Bremsstrahlung process by interacting with the Coulomb field around the nucleus and emitting an energetic photon. The high-energy photon loses energy primarily through converting itself into an electron-positron pair in the vicinity of a nucleus. A cascade of such processes is called an electromagnetic shower.

The electromagnetic shower continues to develop until all the secondaries have sufficiently low energy such that other energy loss mechanisms (mostly ionization) become important. A characteristic length for shower development is the radiation length X_0 which is related to the fractional energy loss as

$$\frac{dE}{E} = -\frac{dx}{X_0}$$

where dx is the thickness of material traversed and E is the initial electron energy.

The radiation length X_0 depends only on the material. For uranium, X_0 is about 3.2mm.

- Hadronic Shower: hadronic particles lose energy primarily through inelastic collisions with atomic nuclei, producing secondary hadrons. This cascade process is called a hadronic shower.

  The hadronic shower continues to develop until all the particles are stopped by ionization losses or absorbed by nuclear processes. The scale is described by the nuclear absorption length λ which only depends on the material (for uranium, $\lambda \sim 10.5$cm).

The calorimeters detect the particles' energy by detecting those low-energy particles in the showers. To reduce the cost and save space, the DØ calorimeters interleave layers of a dense, inert absorber with layers of a material which is sensitive to particles passing through it. Since most of the

energy is absorbed in the inert material, only a portion of the incident energy can be detected (called sampling). This kind of calorimeter is called sampling calorimeter.

The calorimeters (Fig. 2.7) consist of one Central Calorimeter (CC) covering roughly $|\eta| \leq 1$, and a pair of End Calorimeters (ECN and ECS at the north and the south end) covering up to $|\eta| \sim 4$. The boundary between the CC and the EC is approximately perpendicular to the beam direction.

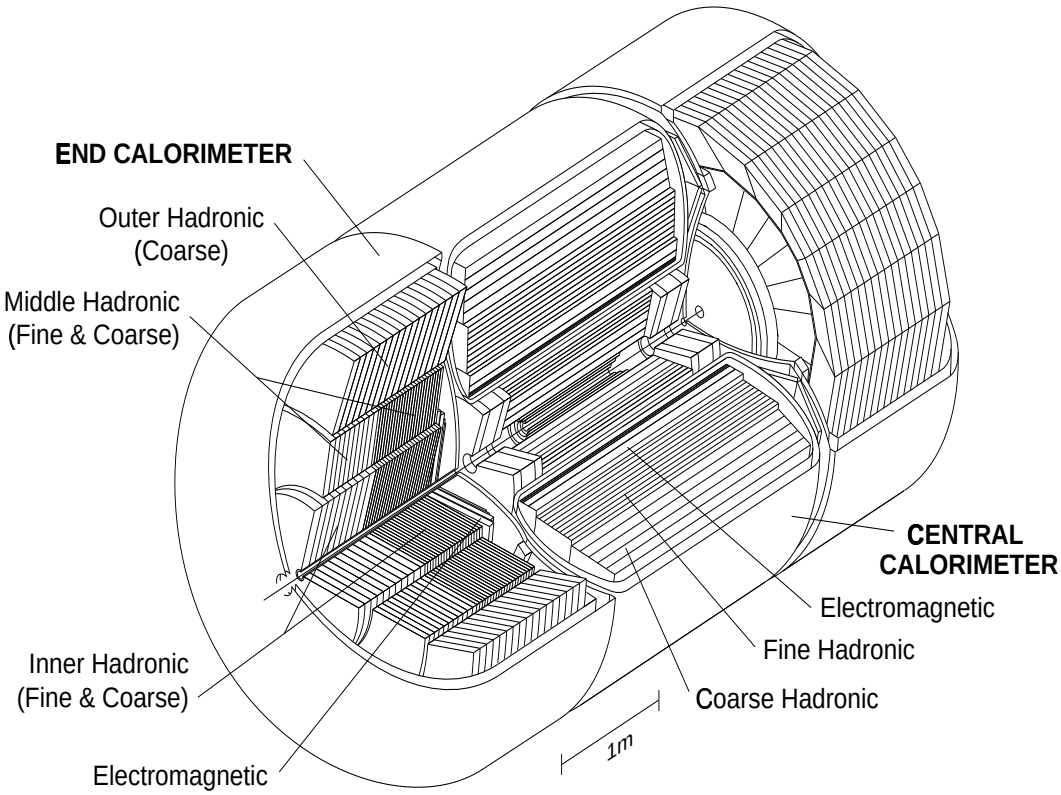

Figure 2.7: DØ Calorimeter.

The calorimeters are divided into a large number of modules, each of which consists of a stack of interleaved absorber plates and signal boards embedded

in liquid argon, the sampling material. There are 3 distinct types of modules in both the CC and the EC:

- Electromagnetic (EM) modules: consist of relatively thin uranium absorber plates, but are thick enough to contain most electromagnetic showers.
- Fine Hadronic (FH) modules: consist of thick uranium plates to measure hadronic showers.
- Coarse Hadronic (CH) modules: consist of thick copper or stainless steel plates to measure any leakage out the FH layer, and also serve to reduce any leakage out of the back of the calorimeter into the muon system ("punchthrough").

The CC consists of three concentric layers of modules. At the innermost are the 32 EM modules with a total of 20.5 radiation lengths (at $\eta = 0$) and a total of 0.76 nuclear absorption lengths (at $\eta = 0$). In the middle are the 16 FH modules with 96.0 radiation lengths (at $\eta = 0$) and 3.2 nuclear absorption lengths (at $\eta = 0$). At the outermost are the 16 CH modules with 32.9 radiation lengths (at $\eta = 0$) and 3.2 nuclear absorption lengths (at $\eta = 0$).

Each EC consists of three concentric layers of modules: EM, FH and CH modules just like the CC, except the geometry is different.

The resolution of the calorimeters is parameterized as

$$\frac{\sigma}{E} = C + \frac{S}{\sqrt{E}} + \frac{N}{E}$$

where the constants C, S, and N are calibration errors, sampling fluctuations, and noise contributions, respectively. The measured resolutions for electrons and pions are (from the test beam studies with the EC[36]):

$$C_e = 0.003 \pm 0.002, S_e = 0.157 \pm 0.005(GeV)^{\frac{1}{2}}, N_e \approx 0.140GeV$$

$$C_\pi = 0.032 \pm 0.004, S_\pi = 0.41 \pm 0.04(GeV)^{\frac{1}{2}}, N_\pi \approx 1.28GeV$$

Further information on the calorimeters can be found in [31].

2.4 Muon Detector

Muons are heavy leptons ($M_\mu \approx 200M_e$), and do not lose a large fraction of its energy due to bremsstrahlung initiating showers in the calorimeters. They also have a long lifetime ($\sim 2.2\mu$s), long enough to go through the detector before most of them decay.

The DØ muon detection system (Fig. 2.8) consists of magnetized iron toroids, a set of Wide Angle Muon Chambers (WAMUS) and a set of Small Angle Muon Chambers (SAMUS) for the location of the muon trajectories before and after the iron. The magnetic field produced by the toroid system provide a means to measure the muon momentum. The WAMUS and SAMUS measure the muon trajectories, from which we can calculate the muon momentum. Since muons are measured after most of the debris of electromagnetic and hadronic particle showers is absorbed in the calorimeters, the muon can be identified in the middle of hadron jets with much greater purity than electrons.

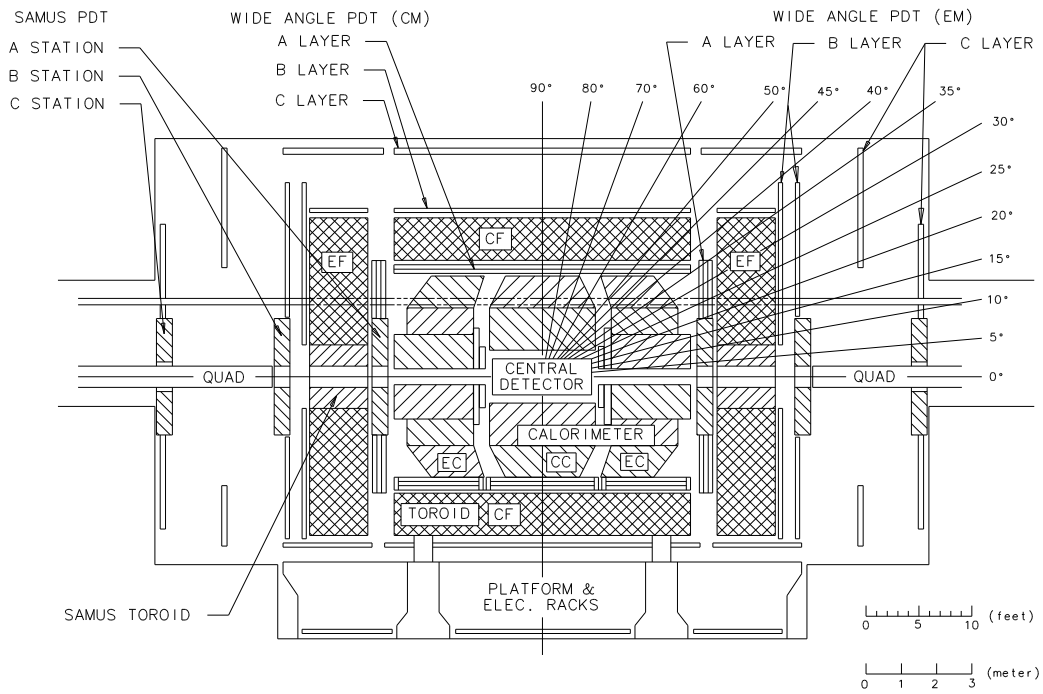

Figure 2.8: Elevation view of the DØ muon system showing the 5 muon toroids and the A, B and C layers of PDT chambers

2.4.1 Toroids

The toroid system of the DØ muon system consists of 5 separate solid iron toroid magnets: 1 Central Toroid (CF), 2 End Toroids (EFs) and 2 SAMUS toroids. The muon toroids provide the magnetic fields necessary for the momentum measurement. The magnetic field is along the azimuthal direction ($\mathbf{B} \sim B_0\hat{\phi}$), and the bending of muon tracks is in the $r - z$ plane.

- CF: the CF toroid is a square annulus 109cm thick, centered on the Tevatron beam lines, located at $-378.5 \leq |z| \leq 378.5$cm. The inner and outer surface of the CF are at perpendicular distances of 318cm and

427cm from the beams line respectively. The CF toroid covers polar angles from 41° to 139° ($|\eta| \leq 1.2$). The coil system of the CF can excite internal fields of 1.9T. The coils are not completely symmetrically placed on the CF, and there are fringe fields, exceeding 0.01T near the central beam.

- EF: the two EF toroids are located at $447 \leq |z| \leq 600$cm in the DØ global coordinate system. Their outer surfaces are at a perpendicular distance of 417cm. The EFs have a 183cm square inner hole centered on the Tevatron beams. The main ring beam, which is 225cm above the beam line, and 33cm to the west of the beam line, passes through a 30cm diameter hole in the EFs (reference [34]). The EF toroids cover polar angles from 9° to 43° ($1.0 \leq |\eta| \leq 2.4$). The coils can excite fields of up to about 2T.

- SAMUS toroids: the SAMUS toroids are located within the inner holes of EFs. The SAMUS toroids have the outer surface at 170cm from the beam axis and a 51cm inner hole. The SAMUS toroids cover polar angles from 2.5° to 11° ($1.7 \leq |\eta| \leq 3.6$). The coils can excite fields around 1.9T.

The muon toroid system is very thick. Together with the calorimeters, it affords a clean environment for identification and momentum measurement of high p_T muons. The total number of nuclear interaction lengths seen by a particle as a function of emission angle is shown in Fig. 2.10. The absorption length of the calorimeter is indicated separately from that of the muon system.

On the other hand, the multiple Coulomb scattering in the toroids sets a lower limit of 18% for the relative momentum resolution. For the determination of the muon charge we require its measured transverse momentum p_T to be 3 standard deviations above zero which holds for $p_T \leq 200$GeV/c at $\eta = 0$ and $p_T \leq 30$GeV/c at $\eta = 3.3$.

The minimum momentum required for a muon to emerge from the iron toroids varies from about 3.5GeV/c ar $\eta = 0$ to about 5GeV/c at larger η.

2.4.2 Wide Angle Muon Chambers (WAMUS)

The WAMUS chambers are deployed in 3 layers, with one layer (called A layer) before the iron toroids, and two layers (called B layer and C layer, with the C layer at the outermost) after the magnetic iron toroids. All the layers consist of proportional drift tubes (PDTs).

PDT Cells

The PDT cell is the most basic building block of the WAMUS system. There are 11,386 PDT cells in total in the WAMUS system. The unit cell of the WAMUS PDT is 10.1cm wide (local x direction), 5.5cm high (local y direction), and has various lengths (local ξ direction. The length varies from 191 cm to 579 cm) for different chambers. It has top and bottom vernier cathode pads (Fig. 2.11). The upper and lower cathode planes are made from two independent electrodes forming the inner and outer portions of a repeating diamond pattern whose repeat distance is 61cm. The 50μm thick sense wire is

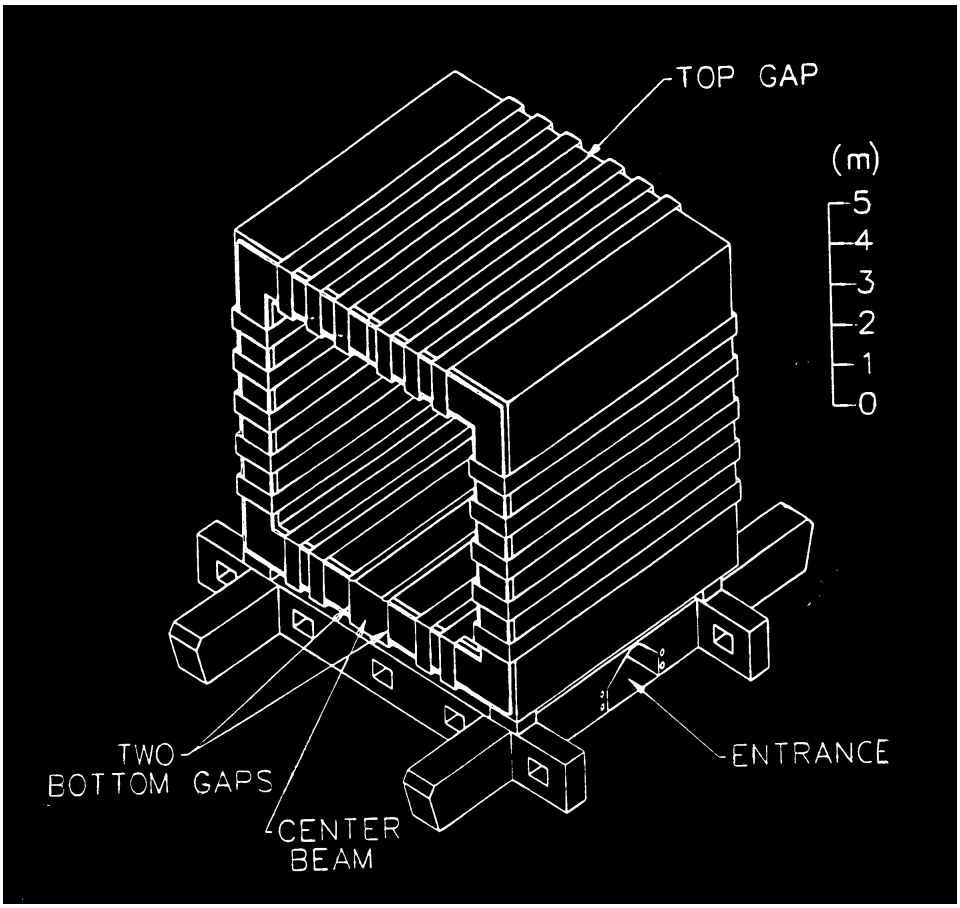

Figure 2.9: Muon System CF toroid. The beamline (not shown) goes through the center of the toroid. The CD and the muon A layer (not shown) are positioned within the toroid, and the muon B and C layer (not shown) are placed outside.

at the center of the PDT. The aluminum tube is grounded while the potential of the anode wire and the pads are kept at 4.54 and 2.30kV respectively. The electrostatic potential of the unit cell is shown in Fig. 2.12.

The coordinate (ξ) along the wire direction is measured by a combination of cathode pad signals and timing information from the anode wires.

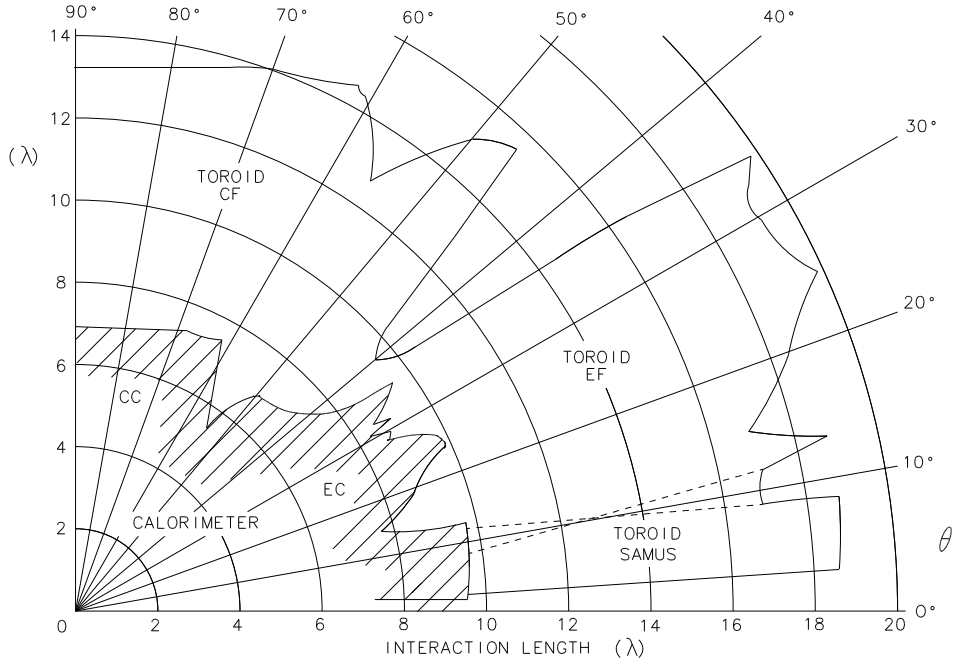

Figure 2.10: Absorption lengths of calorimeter and muon system as a function of the polar angle.

1. Coarse Measurment: The anode wires from adjacent cells are connected at one end for economy. A coarse indication of the ξ coordinate can be obtained by measuring the time difference Δt for a particular anode signal from the two ends of the paired wires. This measurement determines ξ with a precision varying from 10 to 30 cm along the wire.

2. Fine Measurment: The information from the cathode pad signal gives the fine resolution in ξ. The ratio of the sum and the difference of the signals from the inner portion (the central pad connected with "A in" in Fig. 2.11) and outer portion (the outer pad connected with "A out" in Fig. 2.11) of the cathode pads gives a measurement of the ξ

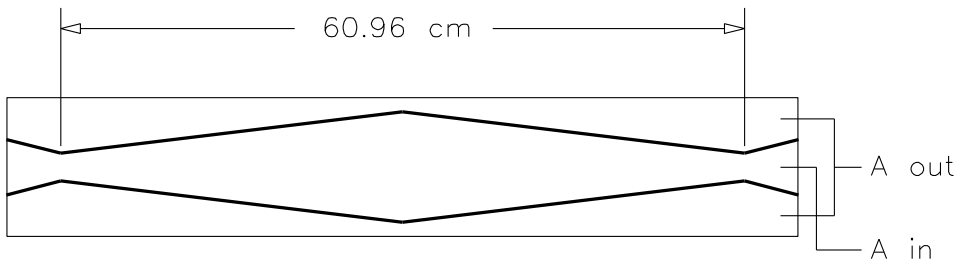

Figure 2.11: WAMUS PDT cathode pad structure

coordinate, modulo the approximately 30cm half repeat distance of the pattern. The pointer for the correct cathode pad solution is given by the Δt measurement. The ξ resolution achieved in a given chamber is approximately 1cm.

The drift time of the muon defines its drift distance with a resolution of ± 0.9mm, which is close to the diffusion limit. To get the best measurement on the muon momentum, all the chambers are oriented so that the PDT anode wires are perpendicular to the beam line, and along the magnetic field (in the ϕ direction) so that the bend corrdinates are measured by the drift time.

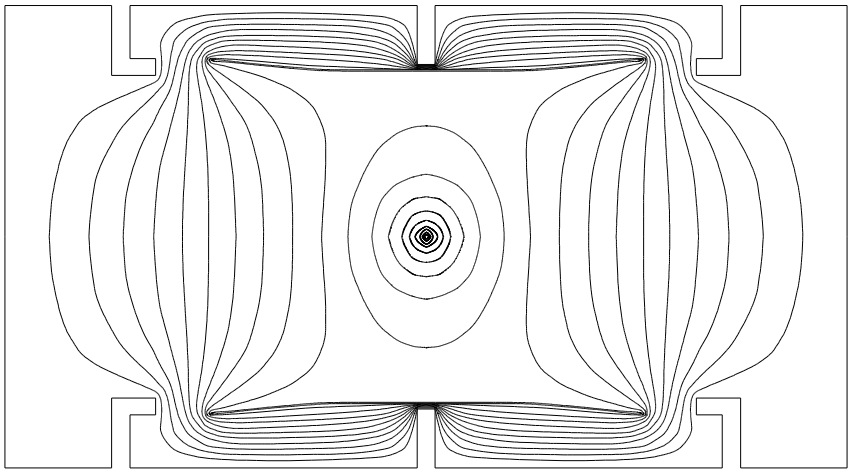

Figure 2.12: WAMUS PDT cell equipotential lines

WAMUS

As mentioned above, the WAMUS chambers are made of PDT cells (Fig. 2.13). There are 164 chambers in WAMUS, with 104 chambers in the A layer, 20 chambers in the B layer and 40 chambers in the C layer. The individual chambers differ mainly in the number of cells in depth (3 or 4 decks) and width (between 14 and 24 cells) and in their length (191 and 579cm). The cells of different decks are staggered to resolve lef-right ambiguities. Reference [38] gives the most comprehensive details of all WAMUS chambers, including their individual dimensions, orientations and other specifications.

The A layer chambers are all 4-deck chambers. They cover the whole inside surfaces of the CF and EF toroids. By using 4-deck chambers, the

distance between the center lines of the innermost and the outermost PDTs is 17cm, enabling us to define the angle and position (in the bend view) of the impinging particle into the toroid iron to an accuracy of ± 0.6mrad and ± 0.1mm respectively.

The B layer chambers and C layer chambers are all 3-deck chambers. The B layer is placed just outside the CF and EF toroids. The typical distance between the centers of the B layer and that of the C layer is 137cm, enabling us to determine the angle and position (in the bend view) of a outgoing particle to an accuracy of ± 0.2 mrad and ± 0.17mm respectively.

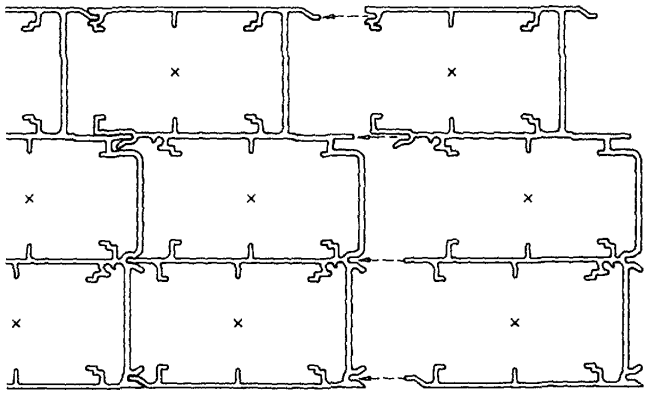

Figure 2.13: Assembly of a 3-deck chamber

The muon system is symmetric around the beam pipe, except that the supporting structure for the calorimeters exclude muon detectors from the space inside the toroid immerdiately beneath the calorimeter cryostats. In addtion, the electronics and other support equipment are contained in work areas under the detector and displace some of the muon chambers.

The measured momentum p resolution of WAMUS can be parameterized as[39]:

$$(\frac{\sigma(\frac{1}{p})}{\frac{1}{p}})^2 = (0.18)^2 + (0.003p[GeV/c])^2$$

Finally, we discuss two terms which are frequently used but also frequently misused: CF chambers and EF chambers (see Figure 2.8).

The WAMUS chambers are either CF chambers or EF chambers. The basic distinction between these two kinds of chambers lies in the deck direction of the chambers. The deck direction is the normal direction of the inter-deck boundary plane (therefore the deck direction coincides with the local y direction of the PDTs in the chambers). Also remember all the WAMUS chambers's ξ direction is always in the XY plane of the DØ global coordinate system (see Figure 2.1) and perpendicular to the beam line (the Z direction).

For the CF chambers, the deck direction is in the XY plane of the DØ global coordinate system, and can be either along the $\hat{X}$ direction or along the $\hat{Y}$ direction; for the EF chambers, the deck direction is in the $\hat{Z}$ direction and perpendicular to the XY plane. The reason to make the distinction between CF and EF chambers is their different performances. The EF muon efficiency is much lower than that of the CF chambers, especially so in run1b before the cleanup of the EF chambers in Februray 1995.

Muons with hits in CF chambers are called CF muons, and muons with hits in EF chambers but with no hits in SAMUS are called EF muons. Most of the CF muons pass through CF toroids, and most of the EF muons pass

through EF toroids. A muon could have both CF and EF hits, or have EF chambers hits after going through CF toroid. But those muons usually go through too little magnetic field and their momentum measurent is dubious. A minimum $\int B \cdot dl$ cut is made which basically eliminates all those cross boundary muons. The pseudorapidity value $|\eta| = 1.0$ approximately divides the CF and EF muons. Since the CF and EF chambers have quite different performances, we will need to calculcate two sets of numbers in most of the analysis described in the later chapters.

Besides reference [38], reference [40] is also a good source of muon system information.

2.4.3 Small Angle Muon Chambers (SAMUS)

The SAMUS system consists of three stations. Similar to the WAMUS, they are named A, B and C station with the A station preceding the toroids. Each station consists of 3 planes of doublets of proportional drift tube chambers. These doublets are oriented in x, y (in the DØ global coordinate system) and u directions (u is at 45°, in the xy plane, with respect to x, y). Individual PDTs in a doublet form a close packed array with adjacent tubes offset by one half a tube diameter. There are 5308 tubes in total in the SAMUS system.

Further information on SAMUS can be found in [31].

2.5 DØ Trigger and Data Acquisition Systems

The $p\bar{p}$ beam crossing occurs about every $3.5\mu s$, which means a possible event rate of 290kHz. In contrast, the data recording rate is only about 2Hz. Trigger and Data Acquisition Systems are the tools with which we pre-select (online select) interesting events and let the data recording system record those events only.

The DØ trigger system has 3 levels of increasingly sophisticated event characterization, reflecting the fact that the higher level trigger have more information and time to make decisions. The Level 0 trigger detects the occurence of an non-diffractive inelastic $p\bar{p}$ collision. It has no dead time within the $3.5\mu s$ beam crossing time. The Level 1 trigger selects events based on a coarse subset of the event data. Most Level 1 triggers have no dead time with a few exceptions referred to as Level 1.5 trigger. The Level 2 trigger selects events based on sophisticated algorithms. The Data Acquisition Systems record events which pass all three levels of the trigger system permanently on magnetic tapes.

2.5.1 Level 0 Trigger

The Level 0 trigger registers the presence of non-diffractive inelastic $p\bar{p}$ collisions and provides information on the z-coordinate of the primary collision vertex. It also serves as the luminosity monitor for the experiment.

The Level 0 trigger is a scintillator-based trigger with no dead time within the 3.5μs beam crossing time. It uses 2 hodoscopes of scintillation counters

mounted on the front surfaces of the end calorimeters. It partially covers the rapidity region $1.9 < |\eta| < 4.3$, and nearly completely covers $2.2 < |\eta| < 3.9$.

The Level 0 trigger registers non-diffractive inelastic $p\bar{p}$ collisions by looking for the coincidence of the 2 scintillation hadoscopes. Non-diffractive inelastic $p\bar{p}$ collisions typically cause a large amount of activity in the far forward regions due to spectator quark fragmentation. With the η coverage specified above, the Level 0 trigger is over 99% efficient in detecting non-diffractive inelastic collisions. At a instantaneous luminosity of $\mathcal{L} = 5 \times 10^{30} cm^{-2} s^{-1}$, its output rate is about 150kHz.

The Level 0 trigger also provides information on the z-coordinate (along the beam) of the primary collision vertex. The large spread of the Tevatron vertex distribution (with a typical $\sigma \sim 30$cm) may introduce substantial error in the transverse energy (E_T) values used in the trigger. To provide E_T corrections with sufficient accuracy, a vertex position resolution of 8cm is needed at Level 1 and 3cm at Level 2. The Level 0 trigger determines the z coordinate by the difference in arrival time for particles hitting the 2 Level 0 detectors (for multiple interactions, the Level 0 time difference information is ambiguous and a flag is set to identify these events in the subsequent trigger levels). The time resolution of each Level 0 counter was measured to be typically 100-150ps. A fast vertex determination with a resolution of $\pm$15cm is available within 800 ns after the collision. A more accurate determination with a resolution of $\pm$3.5cm ($\pm$6.0cm for multiple interactions) is available within 2.1μs [35]. As we will discuss later, the muon Level 2 trigger uses this fine measurement of z for the trigger decision (the muon Level 1 decision is based on the muon

system information and therefore does not use the z measurement).

The Tevatron luminosity is obtained by measuring the rate for non-diffractive inelastic $p\bar{p}$ collisions. Events of this type are selected by requiring a Level 0 coincidence with $|z_{vtx}| < 100$cm (see later chapters for more discussion on this).

It should be pointed out that the results of the Level 0 tests are just input to the Level 1 AND-OR network (see below). The actual trigger decision is made by Level 1 system.

More information about the Level 0 trigger can be found in [35] and [31].

2.5.2 Level 1 Trigger

The Level 1 trigger is used to select events based on a coarse subset of event data. It uses hardware trigger elements for speed (all processing must be completed within the $3.5\mu s$ beam crossing interval to avoid dead time), and is structured with a software-driven architecture for easy modification and flexibility.

The trigger decisions are made in a so-called Level 1 Framework based on inputs from the specific Level 1 trigger devices, such as Level 1 calorimeter trigger and Level 1 muon trigger and various scintillator and timing vetoes.

The Level 1 Framework is a two-dimensional AND-OR network. There are 256 latched bits input (called AND-OR terms) from various Level 1 trigger devices, each representing some specific piece of detector information. Various logical combinations of these AND-OR terms result in the output of 32 Level 1

triggers. If any of the triggers is satisfied, the Level 1 Framework will assemble a block of information that summarizes all the conditions that have lead to a positive Level 1 decision and then pass them on to Level 2 for further analysis.

Many of these Level 1 triggers above operate with no dead time during the 3.5μs between beam crossing. Others, however require several beam crossing times to complete (so-called Level 1.5 triggers). The output rate of the Level 1 trigger is about 200Hz, and about 100Hz for Level 1.5.

The Level 1 muon trigger is further discussed below.

The Level 1 muon trigger can detect the presence of muon tracks and whether they are located in any of the 5 separate η regions of the muon detector: CF, EF-North, EF-South, SAMUS-North, SAMUS-South. The Level 1.5 muon confirmation imposes a further p_T threshold cut.

The basic information provided by the muon chambers to the Level 1 muon trigger is a single latch bit (corresponding to the bend coordinate of hit drift cells) for each of the approximately 16,700 drift cells of the muon system.

These bits are received by 200 module address cards (MACs). which perform zero-suppression and generate bit patterns corresponding to hit centroids (a centroid is defined as the most likely half-cell traversed by a track, projected to the midplane of a chamber). The MACs perform a logical OR on a group of 3 centroids in WAMUS, and thus produce a bit pattern for use by the Level 1 muon trigger (also called CCT, coarse centroid trigger). The WAMUS CCT cards search for possible muon candidates in a hodoscopic, 6 cell wide (60cm) road. The CCT requires at least two hit drift cells (must be from different decks) in all 3 layers, except near the CF-EF boundary (roughly

$0.8 < |\eta| < 1.0$, with only 2 layer coverage) where some 2 layer combinations are allowed. The CCT decisions are available with 3.5μs beam crossing time.

Although there is no p_T cut at the Level 1 muon trigger, the requirement that there are hits in all 3 layers implies a momentum cut of $\sim 3 - 5$Gev/c because the muon has to be energetic enough to penetrate the calorimeters and muon toroids.

The Level 1.5 trigger (also called OTC, octant trigger card) can apply a sharper p_T thresold by requiring a finer match between layers. The OTC compares all combinations of A, B and C layer centroids to determine if they correspond to tracks above a p_T threshold, typically 3-7 Gev/c. However, due to the combinatoric problems of doing this matching, especially in the busy SAMUS regions, this computation often takes longer than the 2.4μ s allotted for Level 1 trigger term decisions. Decision times typically range from 1 to 5 μs in the WAMUS regions, but can take up to 100 μs in the busy SAMUS region.

In addition, scintillor counters are placed on the top or sides of the muon system. The scintillator (with a time resolution of about 3ns) must be hit around the time of the beam crossing (a time gate of 100ns) in order to confirm a Level 1 muon trigger. This is often called scintillator veto (vetoing the trigger if the scintillator is not hit).

Reference [31] contains more detailed information on the Level 1 trigger.

2.5.3 Level 2 Trigger and Data Acquisition System

The Level 2 system is closely interwined with the DØ data acquisition system in hardware. The system collects the digitized data from all relevant detector elements and trigger blocks for events that successfully pass the Level 1 triggers and applies software algorithms on data needed to reduce the rate from the approximately 200Hz input to about 2 Hz output to the host computer and data logger, where they are permanently stored on magnetic tapes for offline analysis.

The Level 2 software event-filtering is based on a series of filter tools. Each tool has a specific function related to identification of a type of particle or event characteristic. The tools are associated into "scripts" which specify the combinations and orders of the tools. Each of the 32 Level 1 trigger is associated with a script, which can spawn several Level 2 filters. There are 128 Level 2 filter bits available in total.

Below we further discuss some general features of the muon Level 2 triggers.

The first stage of the muon reconstruction is performed at Level 2. To minimize the processing time, the search for muon candidates is restricted to the forward region of those sectors which had a Level 1 trigger. A muon must have hits in at least two planes in two PDT chambers. At least 3 out of the following 4 variables must be good (consistent with a beam produced muon): the residuals (the differences between measured distances and fitted distances) in the PDT drift view (local x direxion), the residuals along the PDT wire

(local ξ direction) and the projections of the track to the primary vertex in both views. In the central region, in order to reject cosmic rays, we reject muon candidates with a track in the opposite muon chambers within 20° in ϕ and 10° in θ, or with PDT hits in the opposite side within 60cm (about 5°) of the projected candidate trajectory. The muon momentum is determined by the PDT hits and the vertex information from Level 0. It is less precise than the offline reconstruction results.

At Level 2, if any filter bits are set, the events are sent to the host system to be recorded. The raw data from the online system are then reconstructed with two kinds of output: DSTs and STAs. The DSTs ($\sim$ 15 kbytes/event) contain only the reconstruction results for high-level objects, such as electrons, muons, etc. The STAs ($\sim 600 - 1000$ kbytes/event) contain the raw data of the event in addition to the reconstruction results.

References [37] and [31] contain more detailed information on the Level 2 trigger. Reference [37] also elaborates the details of the data acquisition system.

Chapter 3

Event Reconstruction

DØ RECO is a software package which reconstructs events. It reads in the digital signals collected by the DØ detector. It then interprets(reconstructs) them in terms of higher level objects such as electrons, muons, jets and neutrinos. Details of reconstruction are usually quite technical. But they are integral parts of a complete analysis. Below we will describe the reconstruction algorithms with emphasis on those objects that are directly used in the analysis.

3.1 Interaction Vertex

The interaction vertex is the point where high energy quarks collide. The determination of the vertex position is important. In particular, the z position of vertex affects the determination of the particle polar angle θ and the transverse momenta such as the muon p_T and the missing transverse energy $\not{E}_T$.

The typical cross-section of the beam was about $50\mu m$ at a location about 3-4mm from the center of the DØ detector with a drift of less than $50\mu m$ during a typical data run [41]. The (x, y) position of the vertex can therefore be considered as a constant, and in many cases is taken to be $(0, 0)$ and in other is reconstructed using information from the VTX chambers.

The z-coordinate of the interaction vertex can vary along the beam direction with $\sigma \sim 30$cm(centered on $z = -7$cm). It is measured with CDC(or FDC) tracks[41]. Each CDC track is projected back towards the center of the detector, and its impact paramter[1] is calculated. Tracks with too large impact parameters were discarded (they may be tracks due to low momentum particles which suffer from a large amount of multiple scattering). The remaining tracks are projected into the (r, z) plane and their intersections with the z-axis is calculated. We fit the histogram of the z positions with a gaussian curve and take the mean as the z-position of the vertex and take the width as the error. The resolution of z thus obtained is about 1-2cm. Multiple vertices can be separated if they are at least 7cm apart.

3.2 Muon

The muon reconstruction in the WAMUS takes the raw data as inputs and calculates the muon trajectories and momenta as outputs.

The raw data collected by the muon system consist of, for each PDT, a

[1]The impact parameter is usually defined as the smallest distance from the interaction point to the track.

digital pad-latch indicating a possible hit, and a series of analogue signals that represent the drift time, delta time, and cathode pad charges associated with the recorded pad-latch signal (see the previous chapter for detail discussion).

The muon reconstruction processes the raw data in 3 major steps: hit sorting, track finding, and global fitting. The first two steps[42] use only the muon system information, while the last step[43] includes information from the full DØ detector.

3.2.1 Hit Sorting

During hit sorting, raw data are converted to hit locations in the global DØ coordinate system. The details are discussed below.

The muon reconstruction program first removes corrupted points, and if this fails the complete events is skipped. Then raw WAMUS data are converted into points in space to be used by the track finding processing unit, taking the following steps:

1. The muon reconstruction program loops over all chambers with hits, corrects for the drift time and delta time constants, and then uses the pad latch bits and time information to assign the hit to the even or odd cell (or both). Bad data are flagged (a good hit must have at least one latch bit set and a physical drift time).

2. Then the muon reconstruction program gets the geometry values (orientation, wire length and location in the DØ global coordinate system), and corrects the pad charges for pedestals and gains. Then it converts

the time division (with time of flight correction) to a distance from the wire center (in DØ gloabal coordinates, assuming a 90 degree incident angle).

At this point there still exists a left-right ambiguity in the drift distances (from the drift time measurements), and a similar two-fold ambiguity exists in the vernier pad solutions derived from the corrected cathode pad values and their associated charge ratio. At this stage the two solutions for the drift time are considered as separate hits.

3.2.2 Track Finding

This section of the muon reconstruction program finds muon tracks based on the hits found in the hit sorting section above. It is a process of pattern recognition that a certain set of hits must pass in order to yield a single track through the muon chambers. The details are summarized below:

1. Establishment of a list of hits using a "road" algorithm:

   If BC segment with at least 4 points is found, a matching A layer segment with at least 2 points is searched for. If such a BC segment is not found, an A layer segment with at least 3 points (one of them can be the vertex point) is searched for.

2. All the segments are required to point to the vertex within very loose criteria (3-5m. It is coarse due to multiple scattering at low momentum).

The best segments are selected based on the number of planes participating, pointing to the vertex or not, and the quality of the segment fit.

3. The above procedures are repeated 3 times until up to 6 tracks are found. In the first pass only ABC tracks are accepted; in the second and the third passes, the requirements are relaxed by accepting 2 layer tracks or expanding the "road" searching window by 50%.

4. Track fit: hits are assigned to tracks (a hit can only be assigned to one track). Then the fits in both the bend and the non-bend views are done. Below are the details of the bend view fit (the non-bend view fit is similar).

   (a) For a 3-layer track: first the BC segment is fitted by looping over all possible hits and selecting the best fit. This segment is extrapolated to the magnet center, then this pseudopoint is combined with the A layer points to fit a segment inside magnet (the vertex is ignored).

   (b) For a 2-layer track: for a BC track, the pseudopoint and the vertex are used to get the segment inside magnet; for an AB or AC track, the A layer points and vertex are used to fit the segment inside the magnetic field.

3.2.3 Global Fit

The reconstruction so far only uses information from muon detector only. But there is muon information available from other parts of DØ detector: the VTX, the CDC(or FDC) and the Calorimeter. The global fit combines those inputs with the information from the muon detector using a Least Square fit to find the final muon track parameters and momentum.

The relevant measurements used as inputs for the global fit include (see Fig. 2.8):

- 2 vertex position measurements from the VTX (x and y coordinates);
- 4 CDC tracking measurements (the bend view and nonbend view slopes and interceptions of the best matching CDC track);
- 2 angle measurements (one on each view, with value set to zero, and error describing the Multiple Coulomb Scattering in the Calorimeter);
- 4 tracking measurements from the A layer (the bend view and nonbend view slopes and interceptions of the track);
- 4 tracking measurements from the BC layers (the bend view and nonbend view slopes and interceptions of the track).

There are 16 measurements in total as inputs. The global fit fits them with 7 parameters:

- 4 parmeters to specify the muon track in the CDC (the bend view and nonbend view slopes and interceptions of the track);

- 2 parameters for the Multiple Coulomb Scattering deflection angles due to transversing the calorimeters;
- $1/p$ (the inverse of the muon momentum).

Most($\sim$ 70%) of the muon track candidates found in the muon detector can be successfully fitted globally. The resolution for low momentum muons is dominated by multiple Coulomb scattering in the toroids, and the resolution for high momentum muons is dominated by the resolution of the space point measurements ($\sim 2mm$). The chamber inefficiencies and geometrical misalignment($\sim 1mm$) also contribute to the uncertaities in the muon momentum.

The global fit has proven quite helpful in many analyses at DØ. For example, the first top candidate event at DØ was an $e\mu$ event (both of the top quark in the $t\bar{t}$ pair produced in the $p\bar{p}$ collision have leptonic decays, one to e and one to μ). The muon in this event was first considered a low momentum muon, due to the poor A layer measurement (as we can see in Figure 3.1, we would have labelled it a low momentum muon because of the large bending between the A layer track and the BC layer track) and this event was rejected as a top candidate event. However, careful examination of this event by globally fitting the muon track using inputs from the CDC and the VTX indicated it is a high p_T muon event (the more precise CDC measurement showed the bending was very small, therefore it was a high p_T muon). After further close scrutinies for many aspects by many experienced physicists, this event was considered to be one of the best top candidate events in the entire

RUN 1A.

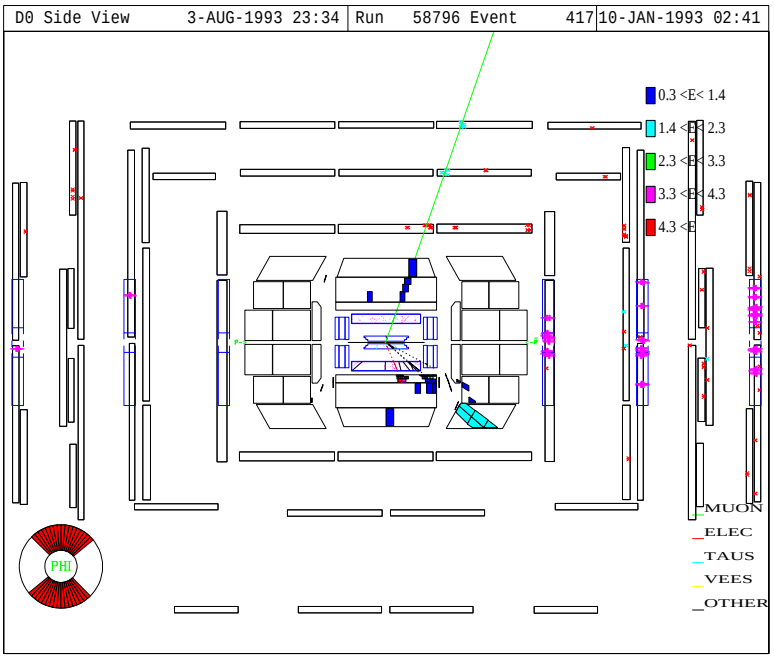

Figure 3.1: The sideview of the first top event at DØ.

During the development of the global fitting software, the most pressing concern was the muon momentum resolution. With many "teething" problems in various parts of the DØ detector at that time, it was necessary to find out which input to the global fit needed improving most. A novel statistical approach was developed and is briefly summarized in the **Appendix A** of this thesis.

3.3 Transverse Missing Energy $\not{E}_T$

Since neutrinos have no charge and interact with other particles weakly, they escape the direct detection of DØ. We can infer their existance by the fact that the total transverse momentum of an event is conserved and must be zero. The negative of the vector sum of all the detected transverse momemta is called transverse missing momentum ($\not{E}_T$) and is considered to be due to neutrinos. On the other hand, the longitudinal momenta of the neutrinos can not be easily deduced because of the uncertainty of the longitudinal momenta of initial state partons and also because of the particles escaping into the beam pipe and thus undetected.

DØ defines missing momentum and missing transverse energy as:

$$\not{E}_x^{cal} = -\sum_i E_i \ \sin(\theta_i) \ \cos(\phi_i)$$

$$\not{E}_y^{cal} = -\sum_i E_i \ \sin(\theta_i) \ \sin(\phi_i)$$

$$\not{E}_T = \sqrt{(\not{E}_x^{cal})^2 + (\not{E}_y^{cal})^2}$$

where the sum is over all the calorimeter cells, and E_i, θ_i, and ϕ_i are the energy deposit, the polar and azimuthal coordinates of cell i respectively.

For events containing muons, we need to correct the above expressions because muons deposit only part of their energies in calorimeters (called Minimum Ionization Particle energy which can be estimated from detector Monte Carlo studies). The corrected expressions are then:

$$\not{E}_x = \not{E}_x^{cal} - \sum_\mu (p^\mu - E^{dep}) \ \sin(\theta_\mu) \ \cos(\phi_\mu)$$

$$\not{E}_y = \not{E}_y^{cal} - \sum_{\mu}(p^{\mu} - E^{dep})\ \sin(\theta_{\mu})\ \sin(\phi_{\mu})$$

$$\not{E}_T = \sqrt{(\not{E}_x)^2 + (\not{E}_y)^2}$$

where $p^{\mu}, E^{dep}, \theta_{\mu}$, and ϕ_{μ} are the muon momentum, energy deposition, polar and azimuthal angles respectively.

The $\not{E}_T$ resolution of the DØ calorimeter may be parametrized as (based on QCD di-jet data):

$$\sigma_{\not{E}_T} \quad = \quad a + b \cdot S_T + c \cdot S_T^2$$

where $a = 1.89 \pm 0.05\ GeV, b = (6.7 \pm 0.7) \times 10^{-3}, c = (9.9 \pm 2.1) \times 10^{-6} GeV^{-1}$, and where S_T is the scalar sum of the transverse energy in the calorimeter [46].

Chapter 4

Luminosity

4.1 Instantaneous Luminosity

The cross section is the interaction probability rate per unit flux. The flux is also called luminosity $\mathcal{L}$ which is proportinal to number of colliding particles(p and $\bar{p}$) per unit time and per unit overlapping area:

$$\mathcal{L} \propto \frac{N_p N_{\bar{p}}}{\sigma_{x,y}^2 \tau}$$

At Tevatron, N_p is about 100×10^9 and $N_{\bar{p}}$ is about 50×10^9(these values hold for the beginning of each store; during the store they decrease as various factors contribute to the depletion of circulating beam intensity). The overlpapping area is characterized by the beam spot size with $\sigma_{x,y} \approx 40\mu m$ at DØ. The beam crossing time $\tau \approx 3.5\mu sec$. Typically in RUN 1B $\mathcal{L} \sim 1 - 20 \times 10^{30} cm^{-2} sec^{-1}$.

At DØ, the instantaneous luminosity $\mathcal{L}$ is determined using the Level 0 trigger system by measuring the rate R of inelastic $p\bar{p}$ scattering:

$$\mathcal{L} = \frac{R}{\sigma_{L\emptyset}}$$

Inelastic $p\bar{p}$ scattering includes hard core, single diffractive and double diffractive scattering. These processes have known cross sections, measured previously at E710[47] and CDF[48][49][50]. Combining these known cross sections with LØ efficiencies for detecting these processes (the efficiencies are calculated using Monte Carlo and DØ data[52]), we can calculate the LØ monitor constant $\sigma_{L\emptyset}$,, the cross section subtended by the LØ. We find $\sigma_{L\emptyset} = 46.7 \pm 2.5mb$, where $1mb = 1 \times 10^{-3} barn = 1 \times 10^{-3} \times 10^{-24} cm^2$.

The inelastic interaction rate R can be determined from the LØ counter rate $R_{L\emptyset}$ which is the same as the interaction rate but only when luminosity is low enough. The LØ can only indicate whether there is an inelastic $p\bar{p}$ scattering during the beam crossing time. Multiple interactions in a single crossing will only be counted once. The average number of interactions per crossing is $\bar{n} = \mathcal{L}\tau\sigma_{L\emptyset}$, Based on Poisson statistics the relation between interaction rate R and $R_{L\emptyset}$ is then:

$$\frac{R}{R_{L\emptyset}} = \frac{\bar{n}}{1-\bar{n}} = \frac{-ln(1 - R_{L\emptyset}\tau)}{R_{L\emptyset}\tau}$$

4.2 Integrated Luminosity

The expected number of a certain type of events(for example $N_{W\rightarrow\mu\nu}$) for a period of running time is found by integrating the luminosity with respect

to time:

$$N = \sigma \int \mathcal{L} dt$$

The integrated luminosity $\int \mathcal{L} dt$ is stored by the DØ trigger system after the LØ measures the instantaneous luminosity and after corrections(such as prescale and main ring veto correction) are made. The integrated luminosity is stored in the Production Database(PDB) for offline analysis.

We define four running and trigger periods (see later chapters for the trigger definitions): EARLY, MIDDLE, LATE-MAX, LATE-CENT. The three time periods correspond to run ranges separated by detector shutdowns and major detector modifications. The 'MAX' and 'CENT' refer to different triggers (see Chapter 6) which ran simultaneously during the latter part of Run 1B. The corresponding integrated luminosities, as extracted from the PBD, are listed in Table 4.1. In the analysis reported in this thesis, we use the MU_1_MAX trigger throughout (namely, the combination of EARLY, MIDDLE and LATE-MAX) with the toal integrated luminosity

$$\int \mathcal{L} dt = 38.3 \pm 3.1 pb^{-1}$$

The combined run period of EARLY and MIDDLE is often called the "pre-cleaning" run period, while the period LATE is called the "post-cleaning" run period. This name convention is due to the cleanup of muon chambers (mostly EF chambers) in February of 1995 (see Chapter 5).

RUN PERIOD	Run Range	MU_1_MAX	MU_1_CENT
Early	70-84 K	12.515 pb^{-1}	N/A
Middle	84-89 K	19.527 pb^{-1}	N/A
Late	89-94 K	6.298 pb^{-1}	23.525 pb^{-1}

Table 4.1: 4 run periods EARLY, MIDDLE, LATE-MAX and LATE-CENT, and the corresponding integrated luminosities.

Chapter 5

Acceptance

The Acceptance is the probability that an event produced in the collisions passes the geometrical and kinematic cuts. For the $W \rightarrow \mu\nu$ and $Z \rightarrow \mu\mu$ analyses we estimate the acceptances using a Monte Carlo event simulation method.

An event generator gives the energy and the angle of the muon(s). The program "DØ GEANT" simulates the various parts of the detector and produces "smeared" muon parameters. However the efficiencies and resolutions are first approximations only. An additional stand-alone program, "MUSMEAR", adds the *measured* efficiencies and resolutions of the muon system. Without this step, we would severely *overestimate* the acceptance.

We will first discuss the Monte Carlo software, then move on to the results of the acceptance measurements.

5.1 Monte Carlo Event Simulation

Besides the name of city, Monte Carlo refers to a numerical method for integration. If we want to integrate a complicate function $f(x_1, x_2, \cdots, x_n)$ over the n-dimensional space of $(x_1, x_2, \cdots, x_n)$, we may have difficulty to do that in analytical form. The Monte Carlo method provides a numerical solution. The average of f over this n-dimensional space is, by definition, the above integration divided by the volume of the space. So the integration problem can be transformed into an averaging problem which is easy to do: one generates N random sets of $(x_1, x_2, \cdots, x_n)$ (uniformly distributed in the volume) and calculates the corresponding f's, then adds up those f's, and gets the average by N divides the sum. However, various techniques are needed for the above scheme to work practically (for example, how to get enough precision without making N astronomically large).

In high energy physics, the Monte Carlo method is used to simulate physics processes. In our context in particular, it is used to simulate the hadron collisions and the subsequent evolution, and to model the detector responses. The tools for the first two simulations are called event generators. The tools to model detector responses are detector simulators. We will discuss them in the following subsections.

5.1.1 Event Generator — ISAJET

The most commonly used Monte Carlo event generators for hadron-hadron collisions are ISAJET[53], PYTHIA[54], and HERWIG[55] (these are the only

3 generators which create output data in a form that is appropriate for the DØ detector simulator). Most of the generators follow the same basic steps in modeling high energy hadron-hadron collisions. The major difference lies in the treatment of beam fragmentation (see below).

The generator we use in this analysis is ISAJET (version 7.13). The main function of ISAJET is to simulate pp and $p\bar{p}$ collisions and to model the hard parton-parton scattering processes that occur. It is based upon perturbative QCD cross sections, leading order QCD radiative corrections for initial and final state partons, and phenomenological models for the fragmentation of hard scattering jets and beam jets into hadrons. Below is a brief description of the major steps it takes in the simulation:

Hard Scattering

ISAJET calculates the hard scattering using the amplitudes and cross sections from the lowest order scattering matrix elements computed in perturbative QCD. These cross sections, $\hat{\sigma}$, are then convoluted with the parton density distributions, $f_i(x, Q^2)$ to give, for example, the $p\bar{p}$ cross section σ

$$\sigma = \int dx_1 dx_2 \hat{\sigma}_{ij} f_i(x_1, Q^2) f_j(x_2, Q^2)$$

where x_1 and x_2 are the parton momentum fractions and Q^2 is the momentum transfer squared.

QCD Evolution

All the partons (see Chapter 1 for discussion on the parton model) involved in the hadron scattering processes are then evolved through repeated parton branchings, based upon a branching algorithm introduced by Fox and Wolfram [56]. The probability that a branching $a \rightarrow bc$ occurs during a small change in the evolution parameter $dt(t = p^2)$ is given by the Altarelli-Parisi equations. The evolution process calculation starts where t takes the maximum allowed value $(t = t_0 = p_a^2)$ and then solves for the value of $t(t = t_1)$ at which the branching occurs. The products b and c can then branch themselves. The branching stops when a parton mass is below some minimum cutoff value (6GeV). This procedure generates both initial and final state radiation.

Hadronization

QCD postulates that only colorless objects are observable. The quarks and gluons emerging from the above QCD evolution must be confined. They must be combined with the quarks and gluons to form colorless particles (mesons and baryons). The process of forming colorless hadrons from the colored partons is called hadronization or fragmentation. It is a non-perturbative process and phenomenological models must be used. ISAJET uses the Feynman-Field independent fragmentation model. In this model, a $q'\bar{q}'$ pair is generated for a quark q with certain momentum. The q and $\bar{q}'$ are combined to form a meson. The leftover quark q' is then fragmented in the same way. The process continues until the energy left falls below some cutoff value. Light quarks are

generated according to the ratio $u : d : s = 0.4 : 0.4 : 0.2$. Baryons are formed by generating diquark pairs with a total probability of 0.08. This approach is also used in many other event generators (except PYTHIA) because it tends to reproduce the limited transverse momenta and approximate scaling of energy fraction distributions observed in quark jets.

Beam Fragmentation

Beam fragmentation is the process of hadronizing those leftover partons that did not participate in the initial hard scattering process. After hadronization these spectator partons will form the bulk of the so-called "underlying event". They must be evolved and hadronized according to some prescription, on which no consensus among different event generators exits. As mentioned above, many of the major differences between the various Monte Carlo event generators center on this beam fragmentation process. ISAJET simply superimposes a "minimum bias event"[1] (generated with multi-pomeron chains which gives scaling and long range correlations) upon the hard scattering event.

5.1.2 Detector Simulator — DØ GEANT

DØ GEANT is a customized version of GEANT (from the CERN Program Library[15]) for the DØ detector. GEANT can accurately simulate the tracking of particles through user-specified detector setups and perform scattering

[1] A minimum bias event is the typical inelastic scattering event detected, which is mostly with no measureable hard scattering.

and interaction processes. The interactions of particles are modeled in terms of various physics processes including δ-ray production, multiple Coulomb scattering, full electromagnetic and hadronic showering, electron and muon bremsstrahlung, and decays. GEANT can simulate the response of various detector components to those processes (for all primary and secondary tracks) and convert them to digitized signals.

To customize GEANT into DØ GEANT which specifically simulates the DØ detector, the geometrical model of DØ including the material used must be added to GEANT. The geometry of the DØ detector is simulated in great detail down to the level of sense wires, cathode material, support structures, etc. However, the treatment of the calorimeter is simplified in our analysis. When full simulation of showering in the calorimeter (requiring DØ GEANT to track hundreds of secondaries through large numbers of uranium plates and argon gaps, which uses a lot of computing resources) is not needed, an approximation is made for the modules. The full structure of the supports and individual modules is preserved, but the contents of the modules are modeled as homogeneous blocks of a uranium-G10-argon mixture (with the correct average atomic weight). This greatly reduces the number of volumes through which DØ GEANT has to track and therefore speeds up the tracking. Within the calorimeter, sampling fluctuations are added after showering for each track, and the appropriate hadron to electron response (determined from test beam results) is introduced. Electromagnetic showers are allowed to evolve until the individual secondaries fall below 200 MeV at which point the deposited energies are determined from simple parameterizations. Shower library func-

tions are used for hadronic showers at their entering the Calorimeter. This approach is called shower library and is used for the hadrons when generating the Monte Carlo events for our W/Z analysis (we should point out that the shower library approach is not applied to the primary muons in the events. They always go through the full DØ GEANT).

From a technical point of view, one of DØ GEANT's features is that it can be easily modified to reflect the actually detector effects. In the next subsection, we will discuss MUSMEAR which is a major addition to DØ GEANT for the muon system in order to simulate the real data more realistically.

MUSMEAR

There is discrepancy between DØ GEANT and the actual situation, majorly due to alignment uncertainties, drift time resolutions, pad latch inefficiencies. MUSMEAR does the following to model those effects [58][61]:

1. MUSMEAR "smears" the muon data as simulated in DØ GEANT so far by making the time electronic resolutions worse. MUSMEAR also drops hits in order to simulate chamber inefficiencies. All this is based on measurements from actual data.

2. MUSMEAR modifies the muon geometry files so as to effect a deliberate misalignment of chamber positions. A typical value of $0 - 1$ mm misalignment (in the drift direction only) was needed for DØ GEANT so that the Monte Carlo $W \rightarrow \mu\nu$ and $Z \rightarrow \mu\mu$ muon distributions would match those of the data.

5.2 Acceptance

We used ISAJET (Version 7.13) to generate about $50,000$ $W \rightarrow \mu\nu$ and about $20,000$ $Z \rightarrow \mu\mu$ events and then processed them with DØ GEANT. We break the acceptance into CF and EF regions because they are vastly different. Further, the muon chambers underwent significant changes (the EF chambers and some of the CF chambers were cleaned up, and the chamber efficiencies were greatly improved during the shut down in February of 1995.

We used different versions of MUSMEAR for the four different run periods:

1. EARLY: E7281_R7988

   The notation is explained below:

   - E: standing for chamber efficiencies which were measured with data between run 72K and 81K;
   - R: standing for chamber resolutions which were measured with data between run 79K and 88K.

2. MIDDLE: E8488_R7988

3. LATE1: E8992_B_R8992

4. LATE2: E9394_R8992

We use the average of the first two MUSMEAR versions (EARLY and MIDDLE) to estimate the acceptance in the pre-cleaning run period, and use

the average of the last two MUSMEAR versions (LATE1 and LATE2) to estimate the acceptance in the post-cleaning run period.

5.3 Cuts

The basic feature of $W \rightarrow \mu\nu$ events is the presence of of a high p_T, isolated muon and a large $\not{E}_T$ corresponding to the neutrino. The basic feature of $Z \rightarrow \mu\mu$ events is the presence of 2 high p_T, isolated muons. The acceptance cuts concentrate mostly on the geometrical and kinematic part, while quality cuts (discussed in later chapter) concentrate on the high quality and isolation part of the events.

The acceptance cuts are based on the definition of a "loose muon". Below we first define a loose muon, then list the acceptance cuts for $W \rightarrow \mu\nu$ and $Z \rightarrow \mu\mu$ events.

5.3.1 The Definition of Loose Muon

A muon is a "loose muon" if it passes all the following three cuts:

1. Pseudorapidity cut: the muon must be a CF or EF muon.

   We restrict our analysis to CF muons and EF muons, which is equivalent to $|\eta| < 1.5$. The overlap muons (overlap muons are muons with a mixture of hits from of EF and SAMUS chambers) are not included in our trigger and for this analysis.

Fig. 5.1 compares the η distribution for $Z \rightarrow \mu\mu$ EF muons for data and that of the Monte Carlo simulation. We see that the Monte Carlo reproduces the η distribution of the data up to $|\eta| = 1.5$ reasonably well. The acceptance drops strongly at $|\eta| = 1.5$ in the data so a fiducial cut is made there.

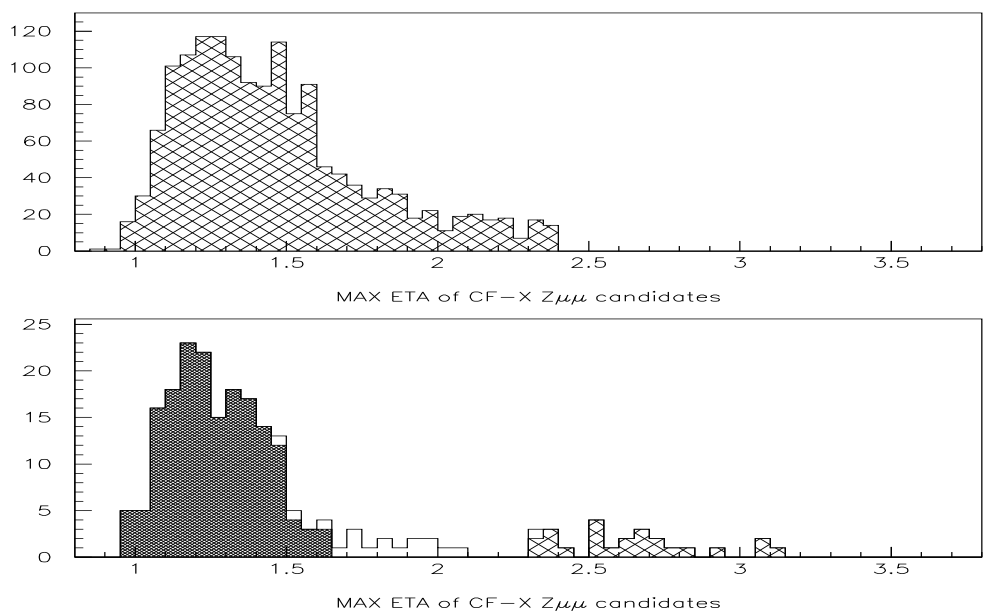

Figure 5.1: Data and Monte Carlo η distributions are shown for the EF leg of CF-EF $Z \rightarrow \mu\mu$ events. The top figure is for Monte Carlo events. The bottom one is for the data, where the dark distribution is for the EF muons, the blank distribution is for the overlap muons (not used in this analysis), and the hashed one is for the SAMUS muons(not used in this analysis).

2. Main Ring muon chambers cut: in the pre-cleaning run period (EARLY and MIDDLE), a sizeable amount of muons were lost in the range of $1.4 \leq \phi \leq 1.92$ (corresponding to ϕ between 80° and 110°. See fig5.2) in the pre-cleaning period. We exclude the ϕ range above from the analysis for the pre-cleaning data. During during that period of time the chambers in this range were extremely inefficient due to heavy radiation damage from the main ring beam halo [59]. The MUSMEAR simulation does not model this inefficiency, so we need to explicitly apply this cut.

3. Fiducial cut: $\int Bdl \geq 0.6$ GeV when $|\eta| > 0.7$.

   We reject muons with $\int Bdl < 0.6$ GeV (or 1.83Tm) because those muons emerge from the gap between CF and EF toroids (in the range of $0.8 \leq |\eta| \leq 1.0$). They do not transverse enough magnetized iron and their momenta are poorly measured. Also they are likely to be contaminated by hadron punchthrough leaking out of the calorimeters.

5.3.2 Acceptance Cuts for $W \rightarrow \mu\nu$ Events

The acceptance cuts for $W \rightarrow \mu\nu$ are:

1. at least 1 loose muon;

2. $p_T \geq 20$ GeV, $\not{E}_T \geq 20$ GeV

   where p_T is the transverse momentum of the muon and $\not{E}_T$ is the missing transverse energy. These two cuts are motivated by the high mass of the

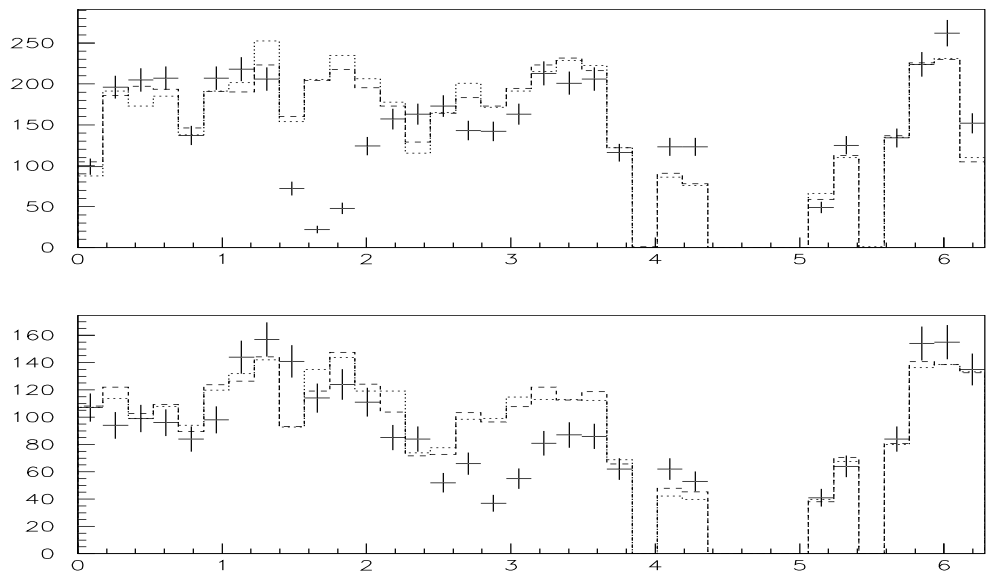

Figure 5.2: Data(the crosses) and Monte Carlo (the dotted and dash line corresponding to the EARLY and MiDDLE MUSMEAR version respectively) of ϕ distributions are shown for precleaning (top) and postcleaning (bottom) CF data. The precleaning Main Ring hole is not simulated in MUSMEAR. The hole around $\phi = 3.0$ in the postcleaning plot is due to the trigger efficiency drop).

W resulting in a large p_T muon and neutrino. These thresholds are quite low in order to maximize the acceptance.

3. we reject the event if there are 2 loose muons and both of them have $p_T \geq 10\text{GeV}$.

   This cut is used to eliminate the Z background in the W sample.

5.3.3 Acceptance Cuts for $Z \rightarrow \mu\mu$ Events

The acceptance cuts for $Z \rightarrow \mu\mu$ events are:

1. at least 2 loose muons;

2. $p_{T1} \geq 20$ GeV, $p_{T2} \geq 15$ GeV

   where p_{T1} and p_{T2} are the transverse momenta of the two muons. By convention, we call the muon with the higher p_T the first muon and the other one the second muon.

3. angle cut: we reject the event if $\Delta\theta(\mu_1, \mu_2) \geq 170°$ and $\Delta\phi(\mu_1, \mu_2) \geq 170°$; we also reject the event if $\Delta\phi(\mu_1, \mu_2) \leq 30°$.

   The first part of the angle cut is motivated by the suppression of cosmic rays, which are likely to have a back-to-back muon pair structure. The second part is used to suppress low mass dimuon events.

5.4 Systematic Errors

5.4.1 Chamber Efficiencies and Resolutions

The MUSMEAR versions which we use to get the acceptance numbers are based on actual measurements with data. Due to continuous bombardment by particles, the chamber conditions deteriorated (the deterioration is related to the total integrated luminosity received by the DØ detector, which is roughly the same during the pre-cleaning and the post-cleaning period). Ideally, we should create at least one MUSMEAR version for each data run. Since this is impractical, we get our measurements to be used in MUSMEAR from a portion of the data runs.

One way to estimated the systematic error due to this simplification is comparing the acceptance results when we use MUSMEAR based on different data runs and take the difference as the error. For the CF acceptance, this error is about 1%. A second and independent way of calculating this systematic error is through a comparison of data and MUSMEAR Monte Carlo trigger efficiencies. This method enables us to directly compare the data with Monte Carlo simulation. If both the hit efficiencies and the trigger simulator were perfectly accurate, then the trigger efficiencies would match exactly. The actual comparison shows that they are close, but with different MUSMEAR versions, the trigger efficiencies from the Monte Carlo simulation vary around the trigger efficiencies from the data. The CF, for example, varies by 6%. It has been established that the trigger efficiencies are twice as sensitive as the

acceptances to changes in the MUSMEAR files[57]. Therefore a 6% range in trigger efficiencies corresponds to a 3% range in acceptances. Since this method gives larger error values, we take them as systematic errors to be conservative (Table 5.1).

To estimate the systematic errors due to chamber resolutions, we find the most "realistic" alignment value used in the Monte Carlo so that the width of the Z invariant mass peak from the Monte Carlo $Z \rightarrow \mu\mu$ events will be the same as that from the data. Then we go through the whole MUSMEAR process using this alignment value, and see how the acceptance changes. The systematic errors are about 1% for the CF. We ignore them due to the dominant errors from the chamber efficiencies.

5.4.2 Parton Distribution Functions

The parton distribution functions (pdf) determine the frequency of the various the initial kinematic states of the incoming quarks and/or anti-quarks and hence affect the kinematical variables of the produced W and Z bosons. Different pdf will change the acceptance numbers.

The pdf used in the above Monte Carlo simulation is `MRSD-'`. This parameterization fits the W charge asymmetry measurement best [62], which is currently the most sensitive probe of the parton structure of the nucleon. There are also other parameterizations available. We use the simpler and faster FAST Monte Carlo program[63] to measure the systematic error due to the pdf choices. We test 3 different parameteriztions (`MRSD0'`, `CTEQ2M`, `CTEQ2MF`).

We take the difference between the resulting acceptances as systematic error due to the pdf choices (Table 5.1).

5.4.3 W Mass Uncertainty

The Z mass has been very precisely determined, and the error on it is so small that we can ignore its effect on the acceptance. The W mass is not as precisely known. We use the FAST Monte Carlo program above, repeating the acceptance calculation with different values for the W mass (which are varied within W mass error. We take the W mass as measured in DØ, $M_W = 80.350 \pm 0.270 GeV/c^2$ [64]). The difference in the acceptance numbers is taken as the systematic error (Table 5.1).

5.4.4 W/Z p_T Distributions

As discussed in Chapter 1, the higher order processes of W and Z production involve recoiling jets. These recoiling jets affect the p_T spectrum of the W and Z bosons. To estimate the systematic errors due to the uncertainty in the W/Z p_T distributions, we use the same FAST Monte Carlo program above and vary the p_T parameterization within one standard deviation. We take the variation in the resulting acceptance numbers as the systematic error (Table 5.1).

Pre-cleaning (%)						
Accpt	Value	Stat	Chmb Eff	pdf	M_W	p_T
$\mathcal{A}_{W,CF}$	20.14	± 0.17	± 0.61	± 0.30	± 0.03	± 0.03
$\mathcal{A}_{W,EF}$	6.31	± 0.11	± 1.60	± 0.08	± 0.01	± 0.01
$\mathcal{A}_{Z,CFCF}$	5.70	± 0.16	± 0.50	± 0.30	± 0.03	± 0.01
$\mathcal{A}_{Z,CFEF}$	5.61	± 0.16	± 1.40	± 0.18	± 0.07	± 0.03
$\mathcal{A}_{Z,EFEF}$	0.65	± 0.06	± 0.19	± 0.01	± 0.01	± 0.00
Post-cleaning (%)						
Accpt	Value	Stat	Chmb Eff	pdf	M_W	p_T
$\mathcal{A}_{W,CF}$	21.90	± 0.19	± 0.70	± 0.33	± 0.04	± 0.04
$\mathcal{A}_{W,EF}$	8.52	± 0.13	± 0.51	± 0.14	± 0.01	± 0.02
$\mathcal{A}_{Z,CFCF}$	6.26	± 0.21	± 0.39	± 0.34	± 0.05	± 0.01
$\mathcal{A}_{Z,CFEF}$	7.61	± 0.23	± 0.60	± 0.32	± 0.18	± 0.04
$\mathcal{A}_{Z,EFEF}$	1.06	± 0.09	± 1.00	± 0.03	± 0.02	± 0.01

Table 5.1: The acceptance results for pre-cleaning and post-cleaning periods of run 1B. The errors quoted are, respectively, statistical errors, chamber efficiencies errors, pdf errors, M_W errors and boson p_T spectrum errors.

5.5 Summary of Acceptance and Errors

Table 5.1 summarizes the acceptance results. The distributions of the transverse mass of the W and invariant mass of the Z from data (with background subtracted) are shown in Fig. 5.3, Fig. 5.4, and Fig. 5.5, together with those from the Monte Carlo simulation. The match between Monte Carlo and data distribution gives us further confidence in the accuracy of the Monte Carlo simulation.

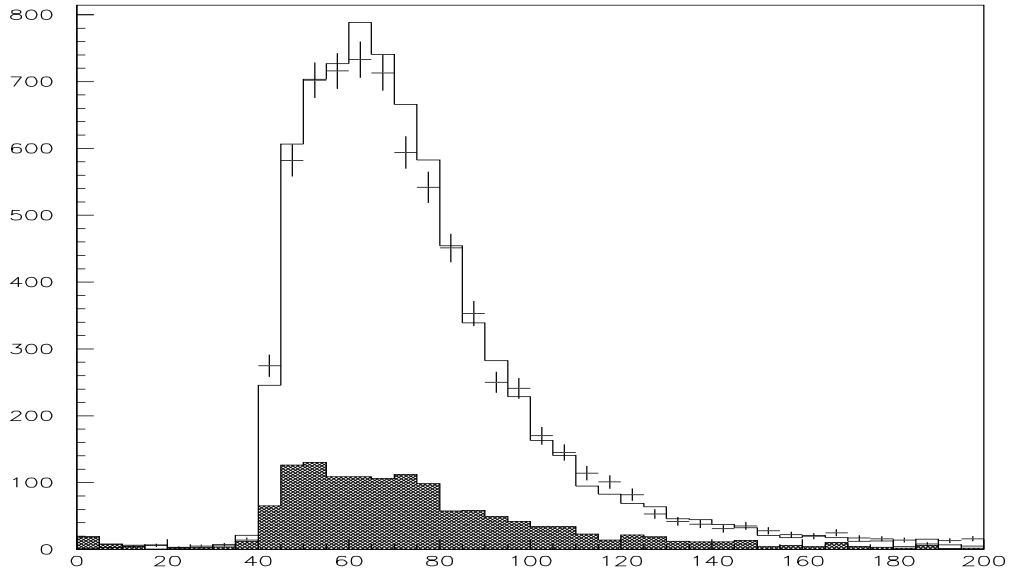

Figure 5.3: Comparison of the W transverse mass for data and Monte Carlo. The points represent the data. The hashed area shows the contribution of the backgrounds (see Cahpter 8) and the blank area gives the expected signal plus background distribution. The unit for the transverse mass is GeV/c^2.

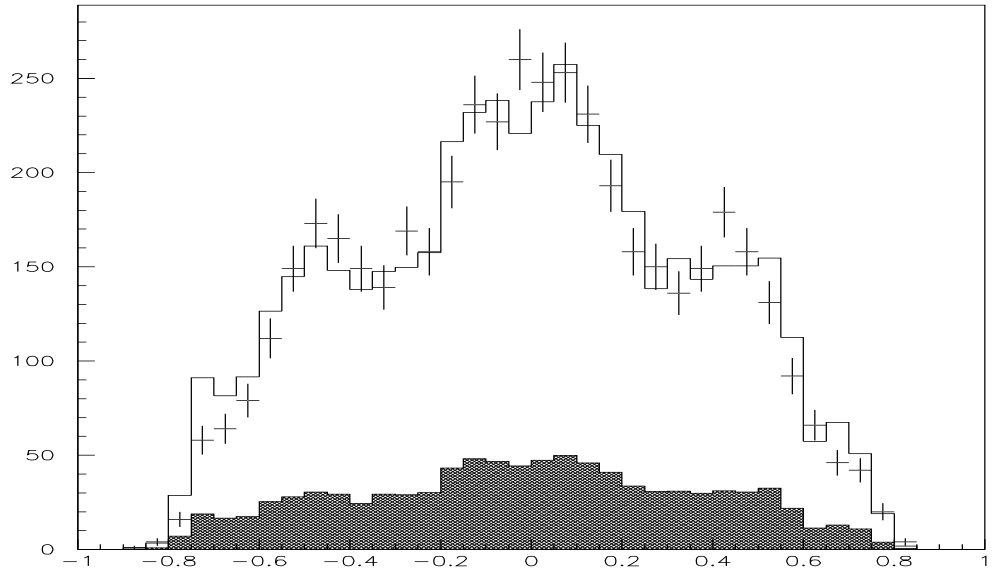

Figure 5.4: Comparison of the muon η in the $W \rightarrow \mu\nu$ for data and Monte Carlo (for the CF only). The points represent the data. The hashed area shows the contribution of the backgrounds and the blank area gives the expected signal plus background (see Chapter 8) distribution.

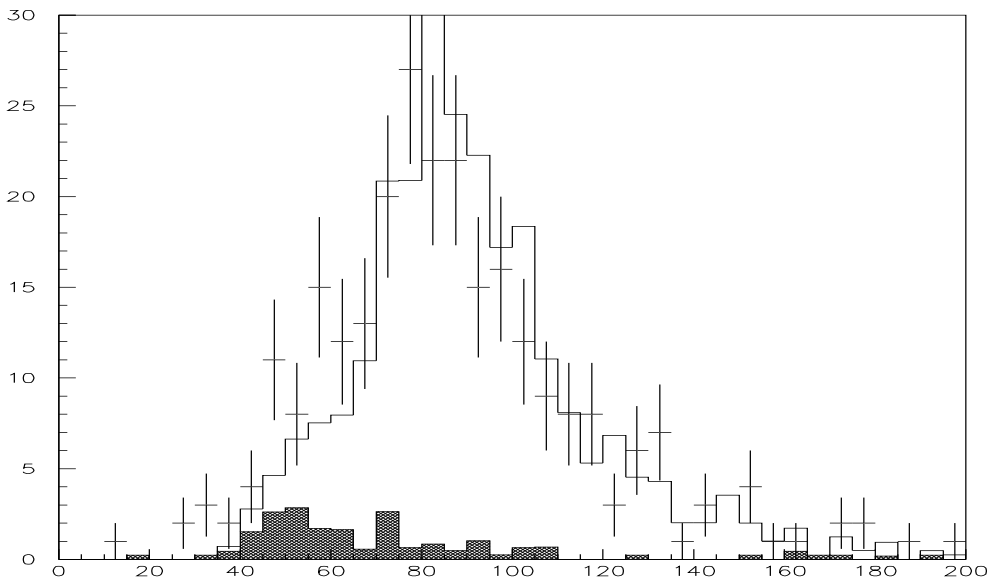

Figure 5.5: Comparison of the Z invariant mass for data and Monte Carlo. The points represent the data. The hashed area shows the contribution of the backgrounds and the blank area gives the expected signal plus background (see Chapter 8) distribution. The unit for the invariant mass is GeV/c^2.

Chapter 6

Selection Efficiencies and Trigger Efficiencies

In this chapter we will discuss the efficiencies of the muon offline selection cuts and the efficiencies of the W/Z trigger.

We have discussed the definition of a "loose muon" in the previous chapter. In this chapter we introduce the definition of a "standard muon" and a "tight muon". These two definitions correspond to two groups of offline selection cuts. The efficiencies of these cuts will be studied the $Z \rightarrow \mu\mu$ data sample and a detailed inspection of many aspects of the events by physicists (called "eye-scanning") rather than using software algorithms.

Then we will turn to the W/Z trigger efficiencies. They will be studied with an unbiased muon sample and cross-checked with $Z \rightarrow \mu\mu$ events.

6.1 Reconstruction and Selection Efficiencies

Data events are more complicated than Monte Carlo events. Therefore additional efficiency factors beyond the acceptance derived from the Monte

Carlo are needed to do the cross-section calculation. The first of these, the reconstruction or "loose" muon efficiency, is a factor which accounts for failures in track finding. These failures are mainly due to non-Gaussian tails of hit variable distributions and therefore not included in MUSMEAR. This efficiency is calculated from data events. The second factor, the selection or "tight" muon efficiency, accounts for the efficiency of the selection cuts (described below) applied to the W muon and at least to one of the two Z muons. Again the Monte Carlo is not considered reliable enough to estimate this, and the efficiencies are calculated from the data.

6.1.1 Reconstruction Efficiency

A muon is a "standard muon" if

1. it is a loose muon as defined for the acceptance cuts,

2. it has a muon track quality $IFW4 \leq 1$,

   The muon system checks the track quality in many aspects and uses IFW4 to count the number of failures in the following checks (all the variables below are based on the measurements from the muon system only):

   - No missing modules
   - The nonbend view impact parameter ≤ 100 cm
   - The bend view impact parameter ≤ 80 cm

- The nonbend view fit has hit residual rms ≤ 7 cm
- The bend view fit has hit residual rms ≤ 1 cm

The IFW4 cut is a powerful cut to suppress cosmic rays and combinatorics[1]. By requiring $IFW4 = 0$ for EF muons, we can keep the backgrounds in the EF low, where there are considerable background and inefficiency problems. We relax the IFW4 requirement in the CF, allowing one of the checks listed above to fail, in order to have a higher efficiency.

3. it has a good calorimeter track:

   The Muon Tracking in the DØ Calorimeter (MTC) is the name of a software package developed at DØ. It uses calorimeter information to identify the "track-like" (no electromagnetic and hadronic shower and no strong interaction present) energy deposition of muons in the calorimeter. Although the calorimeter's transverse segmentation is coarse compared to the muon chambers, a calorimeter track can be reconstructed successfully when the muon is well isolated from other particles in the event. This is particularly true for the WZ analysis. Muons leave a distinctive energy deposition over the total path length, that of a minimum ionizing particle (MIP). The existence of a vertex point provides another constraining point. In short, the MTC is a means for locating muon candidates with calorimeter information independent from the

[1]Combinatorics are faked tracks constructed by the software based on some random hits which happen to resemble a cluster of hits left by particles.

muon detector (more detailed discussion can be found in References [65] and [66]). Among the many output quantities from the MTC, two are of particular interest:

- the fraction of hadronic calorimeter layers used for the track fitting (HFRAC). For a good MIP muon, HFRAC should be 100%. Usually, in order to keep the efficiency high, we relax the minimum requirement to 0.7, which means no more than 1 layer of the hadronic calorimeter can be missing from the fit.
- the fraction of the total energy deposited in a 3×3 calorimeter cell region around the track in the last hadronic layer of calorimeter (EFRCH1). If HFRAC is less than 100%, then the last layer must be hit. We must have $EFRCH1 > 0$ if $HFRAC < 1.0$.

We use "MTC cut" as a shorthand notation for the following combination of MTC cuts:

- $HFRAC \geq 0.7$,
- $EFRCH1 > 0$ if $HFRAC < 1$.

The efficiencies of the standard muon cuts are conventionally called muon reconstruction efficiencies. The muon reconstruction efficiencies were calculated from an eye-scanned muon sample [67].

In order to reduce number of events to eye-scan, we take events from a "muon plus jet" trigger (this introduces a trigger bias, The effect of which

will be discussed below) to have a "muon-rich" sample, and eye-scan them to identify good muons and see if they would be cut off by the standard muon cuts. The eye-scanning process relies on the scanner's experience and judgement. The bias of the individual person can be minimized when several people participate in the process and the scanning results are compared. Typically, the following empirically established scanning criteria are applied to identify good muons:

- In the bend view, examine the A layer hits, and check if they are consistent with a track coming from the beam.
- In the bend view, check the B and C layer hits and see how well they match the inside track. In many cases, a π or a K can have a good track before the iron toroid, but its BC segment results from combinatorics. We discard such events.
- In the non-bend view, check the BC layer track to see if it points to the vertex.
- Cosmic rays can be spotted through their failure to point well to the vertex. This can usually be seen in the muon chambers or in the calorimeter.
- check the energy depositions in the calorimeter to see if they line up with the hits in the muon chambers.

The efficiencies for the standard selection are [68]:

$$\epsilon_{CF,standard} = 0.877 \pm 0.021$$

$$\epsilon_{EF,standard} = 0.840 \pm 0.028$$

As mentioned above, the scanned sample may have a trigger bias. In contrast to our W and Z sample, eye-scanning sample is a low p_T sample. In order to cross check the above results, we use the $Z \rightarrow \mu\mu$ data sample, where one muon passes all the tight cuts including the trigger. This cross-check of the scanning results is weak due to the low statistics of the $Z \rightarrow \mu\mu$ data sample. The MTC efficiency in the CF (0.934 ± 0.028) gives results (with larger errors) consistent with the scanned results (0.932 ± 0.017). There were not enough events in the EF to do this.

For the study of the efficiency dependence on the luminosity or the number of interactions in the same event, we divide the scanned results into groups with the same number of interaction vertices. The basic tool is the so-called MITOOL. We discuss the MITOOL briefly below for completeness. More details can be found in Reference [70] and [71].

MITOOL stands for Multiple Interaction Tool. It is DØ software to discern whether or not an event is determined to be a single or multiple interaction event. It sets a flag for the event based on the information of the Level 0 multiple interaction flag, the Level 0 Slow Z value, the CD Z value of the primary vertex, and the weights, number of tracks, and other data from all the stored CD primary vertices. This flag is also called MITOOL, and can take the value of 0, 1, 2, 3 or 4, with the following meaning:

- $MITOOL = 0$: no vertex information or a failure;
- $MITOOL = 1$: most likely a single interaction;
- $MITOOL = 2$: likely a single interaction;
- $MITOOL = 3$: likely a multiple interaction;
- $MITOOL = 4$: most likely a multiple interaction;

As can be seen in Table 6.1, there is no statistically significant dependence on MITOOL.

MITOOL	CF	EF
1	$(88 \pm 3)\%$	$(81 \pm 5)\%$
2	$(84 \pm 6)\%$	$(95 \pm 5)\%$
3	$(90 \pm 4)\%$	$(69 \pm 8)\%$
4	$(87 \pm 3)\%$	$(86 \pm 5)\%$

Table 6.1: Efficiencies for scanned good muons passing the standard muon cuts as a function of the MITOOL variable.

However, a small difference in pre- and post-cleaning reconstruction efficiency was noticed. Since this difference is just over 2σ, and is not a function of the increased luminosity, we do not consider it significant. For completeness, it is included here.

$$\epsilon_{CF,precleaning} = 0.917 \pm 0.023$$

$$\epsilon_{CF,postcleaning} = 0.825 \pm 0.037$$

6.1.2 Selection Efficiency

We select high quality muons by imposing further selection criteria. A muon is a "tight muon" if

- it is a standard muon;
- it passes all the tight quality cuts, which can be put into 3 categories: high tracking quality, good timing, and isolation:

  1. high tracking quality: the cut on the global fit χ^2 is augmented by additional CD match and impact parameter cuts.

     - Global Fit: $\chi^2 \leq 20.0$

       The global fit χ^2 is a quantitative measurement of the overall quality of the muon track. Thus a good χ^2 is required. See Figure 6.1 for the comparison of signal and background χ^2 distributions.

     - CD Match: $\Delta\theta \leq 0.12$rad, $\Delta\phi \leq 0.04$rad

       A good global fit already implies a good CD match. The CD match cut explicitly and more strictly requires a CD track to match the muon track. For comparison, DØ RECO only requires $\Delta\theta \leq 0.45$rad, $\Delta\phi \leq 0.45$rad. See Figure 6.2 and Figure 6.3 for the comparison of signal and background $\Delta\theta$ and $\Delta\phi$ distributions.

     - Impact parameters, two cuts:

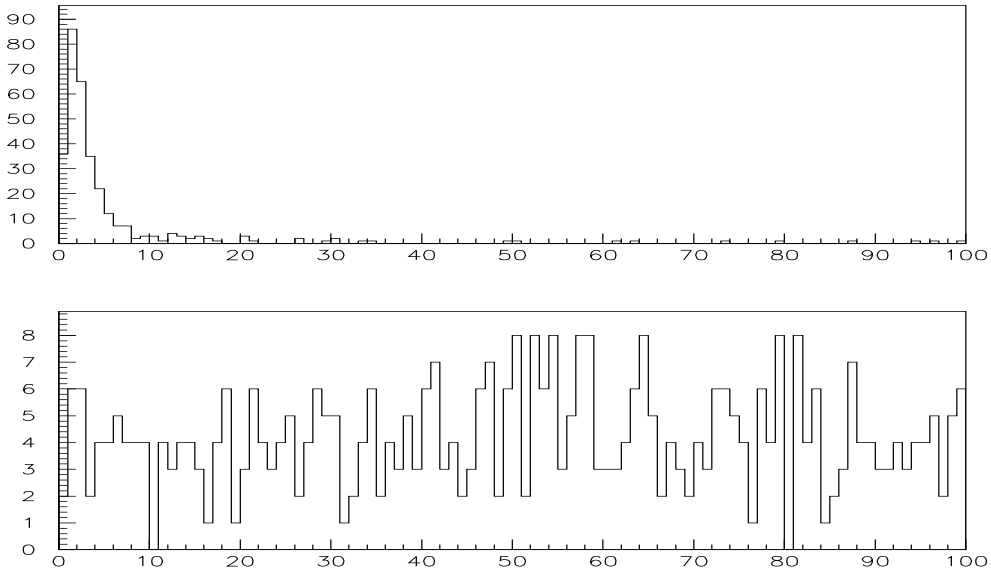

Figure 6.1: χ^2 distributions. The top figure is for the signal muons (the other leg in the $Z \rightarrow \mu\mu$ events has to be a "tight" muon). The bottom figure is for the cosmic rays.

* $b_{\text{bend-view}} \leq 15\text{cm(CF)}, 20\text{cm(EF)}$

  The bend-view impact parameter is defined as the impact parameter of the muon track in the $r - z$ plane. It is calculated using the muon A layer track plus the point extrapolated from the B and C layer track to the center of the iron toroids. This cut is tighter than the nonbend-view impact parameter cut below because the best of the muon chamber

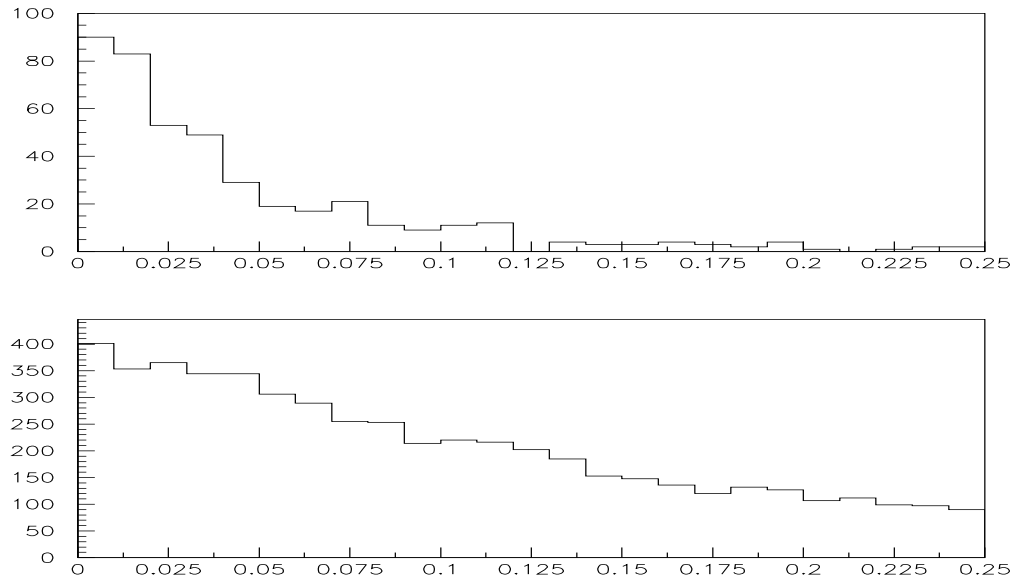

Figure 6.2: $\Delta\theta$ (radians) distributions. The top figure is for the signal muons (the other leg in the $Z \to \mu\mu$ events has to be a "tight" muon). The bottom figure is for the cosmic rays.

space measurements are done with higher accuracy in this plane (the drift distance measurement, as discussed in Section 2.4.2). See Figure 6.4 for the comparison of signal and background bend-view impact parameter distributions.

* $b_{\text{nonbend-view}} \leq 20\text{cm(CF)}, 25\text{cm(EF)}$

  The nonbend-view impact parameter is defined as the impact parameter of the muon track in the $x - y$ plane. It is

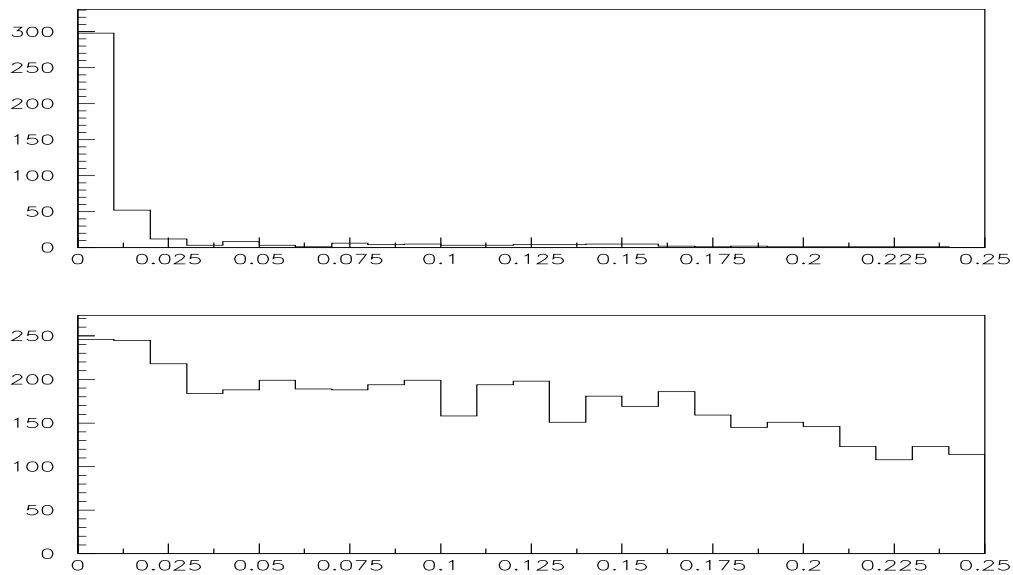

Figure 6.3: $\Delta\phi$ (radians) distributions. The top figure is for the signal muons (the other leg in the $Z \rightarrow \mu\mu$ events has to be a "tight" muon). The bottom figure is for the cosmic rays.

calculated using only the muon track segment measured by the B and C layer chambers (since the muon track inside the iron toroids is already constrained to the interaction points in the $x - y$ plane). See Figure 6.5 for the comparison of signal and background bend-view impact parameter distributions.

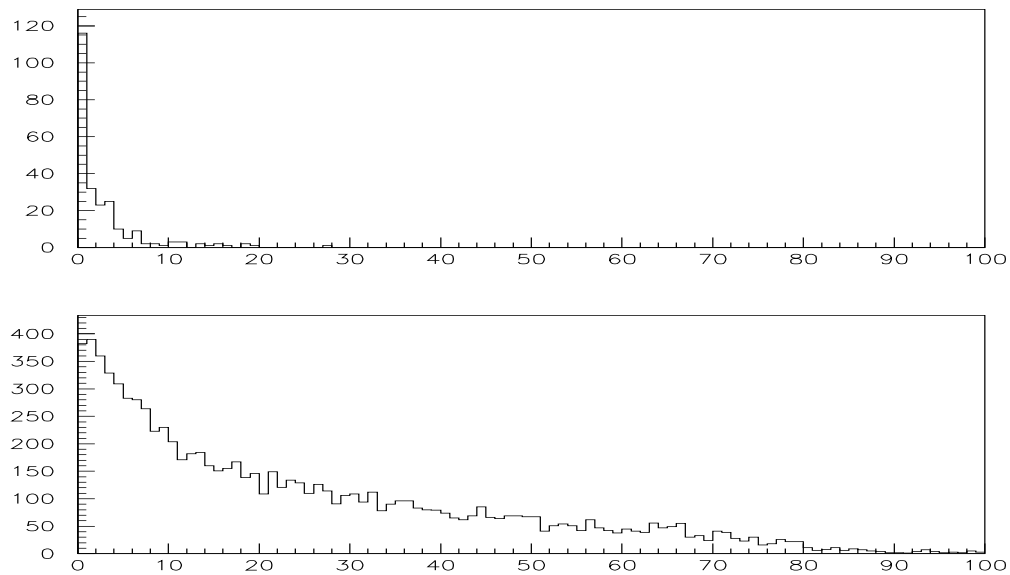

Figure 6.4: The bend-view impact parameter (cm) distributions. The top figure is for the signal muons (the other leg in the $Z \rightarrow \mu\mu$ events has to be a "tight" muon). The bottom figure is for the cosmic rays.

These two cuts require the muons to come from the interaction point and thus suppress the cosmic ray backgrounds. Similar to the CD match cut, the impact parameter cuts are closely related to the global fit cuts.

2. good timing: floating time $t_f \leq 100ns$

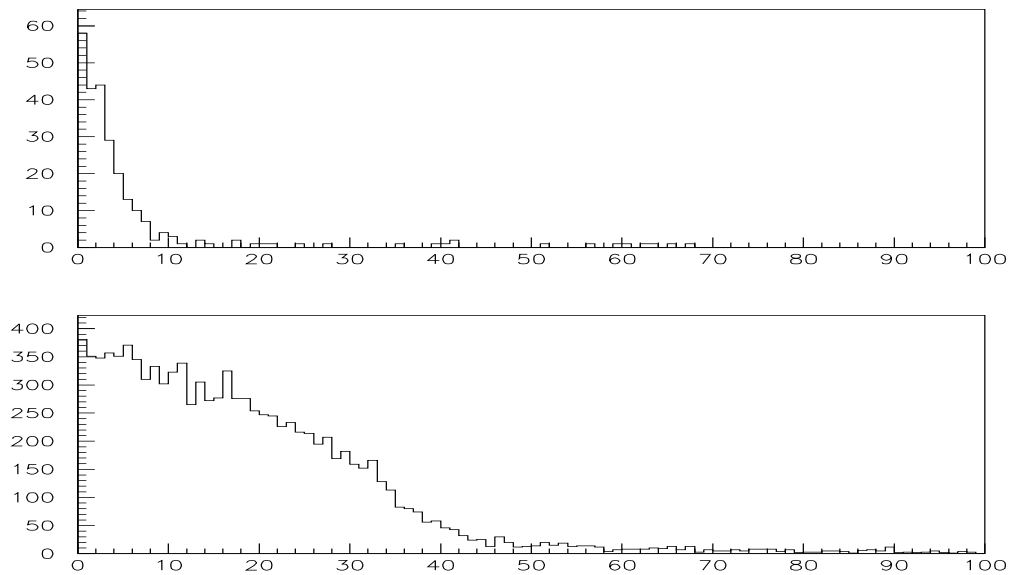

Figure 6.5: The nonbend-view impact parameter (cm) distributions. The top figure is for the signal muons (the other leg in the $Z \rightarrow \mu\mu$ events has to be a "tight" muon). The bottom figure is for the cosmic rays.

The "floating time" t_f is an offset added to the nominal beam crossing time and is fit to give the best muon track fit. This floating time peaks at 0ns for good beam-produced muons, but is flat (except for a trigger bias) for cosmic ray and combinatorics. The trigger bias induces a distribution peaked at +100 ns since the muon trigger gate is asymmetric about the beam crossing time. See Figure 6.6 for the comparison of signal and background t_f distributions.

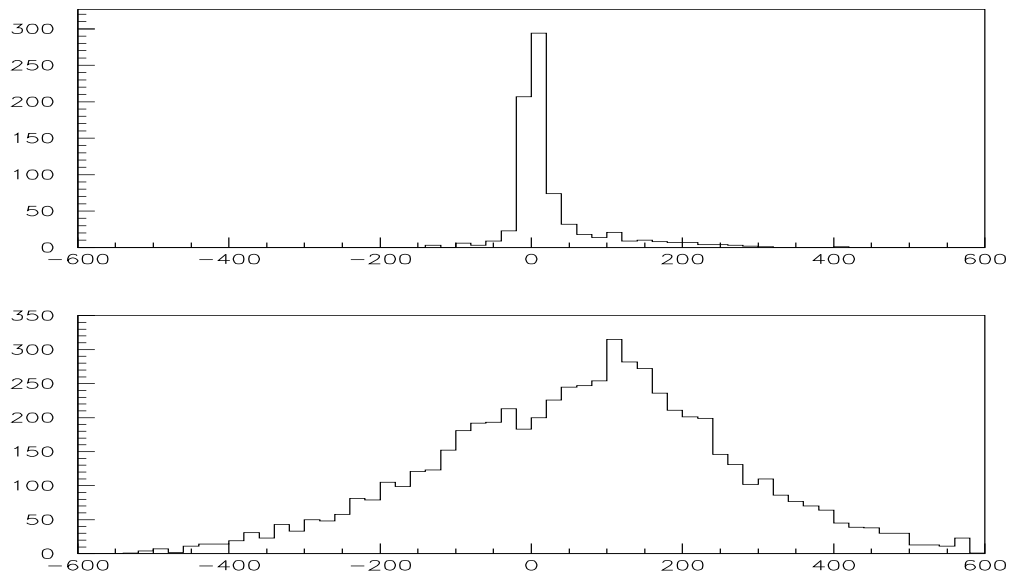

Figure 6.6: The floating time (ns) distributions. The top figure is for the signal muons (the other leg in the $Z \to \mu\mu$ events has to be a "tight" muon). The bottom figure is for the cosmic rays.

3. Calorimeter Isolation:

   We require the muon to be isolated from other particle depositing energy in the calorimeter close to the muon track. This is a feature of $W \to \mu\nu$ and $Z \to \mu\mu$ events.

   We use the following pair of cuts:

   - $I_\mu(2nn) \leq 3$, where $I_\mu(2nn)$ is defined to be

$$I_\mu(2nn) = \frac{E(+2NN) - E(\text{expected})}{\sigma(\text{expected})}$$

$E(+2NN)$ is the sum of the calorimeter energy deposited in the muon-hit cells plus their 2 nearest neighbors (a 5×5 block of cells), $E(\text{expected})$ is the expected energy deposition from the muon itself, generally that of a minimum ionizing particle (MIP). For isolated muons the deviation of the energy deposition should mostly be smaller than 3σ. The $I_\mu(2nn) \leq 3$ cut rejects non-isolated muons that are close to a jet, as in the case of muonic b and c decays. See Figure 6.7 for the comparison of signal and background I_μ distributions.

- Halo Cut: $E(0.2 \leq \Delta R \leq 0.6) \leq 6$ GeV, where $\Delta R = \sqrt{\Delta\eta^2 + \Delta\phi^2}$.

  This cut is similar to the MIP cut above, except we are looking at a larger region in the calorimeter around the muon track. We require the energy deposition to be small in a region between two concentric cones. See Figure 6.8 for the comparison of signal and background halo energy distributions.

The tight muon efficiencies are conventionally defined to be the efficiencies of the tight quality cuts above (excluding the standard muon efficiency which has already been calculated in the first two sections of this chapter). They can be studied using the $Z \to \mu\mu$ data sample[68] by requiring one muon in the $Z \to \mu\mu$ events to pass all the above cuts, and counting how many of the

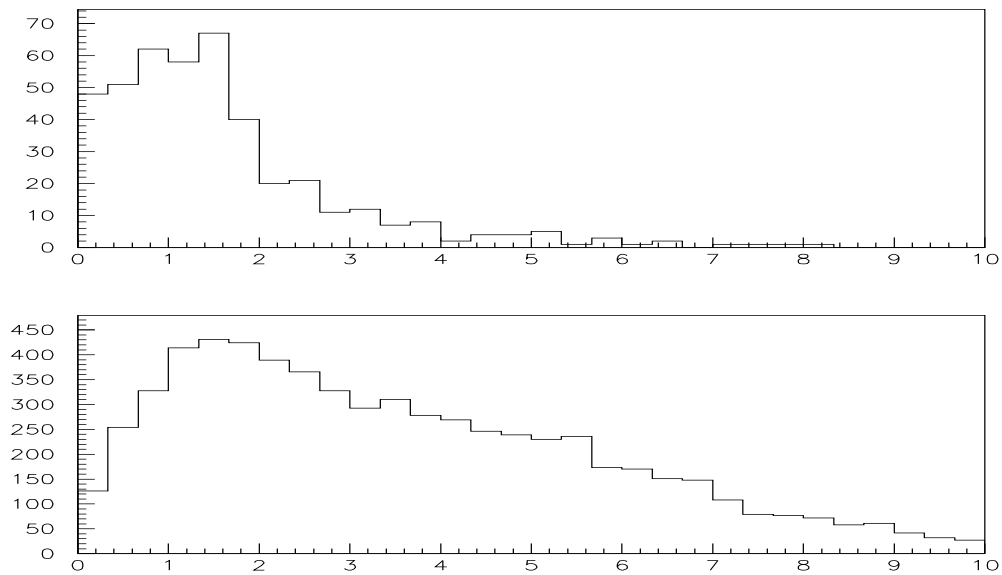

Figure 6.7: I_μ distributions. The top figure is for the signal muons (the other leg in the $Z \to \mu\mu$ events has to be a "tight" muon). The bottom figure is for the QCD events.

other legs pass or fail the cuts. To be exact, if the number of the events in which both muons passes the tight quality cuts (called tight-tight events) is N_{TT}, and the number of the events in which at least one muon pass the tight quality cuts (called tight-loose events, because the other muon has to pass the loose muon cuts and the standard muon cuts, but not necessarily the tight

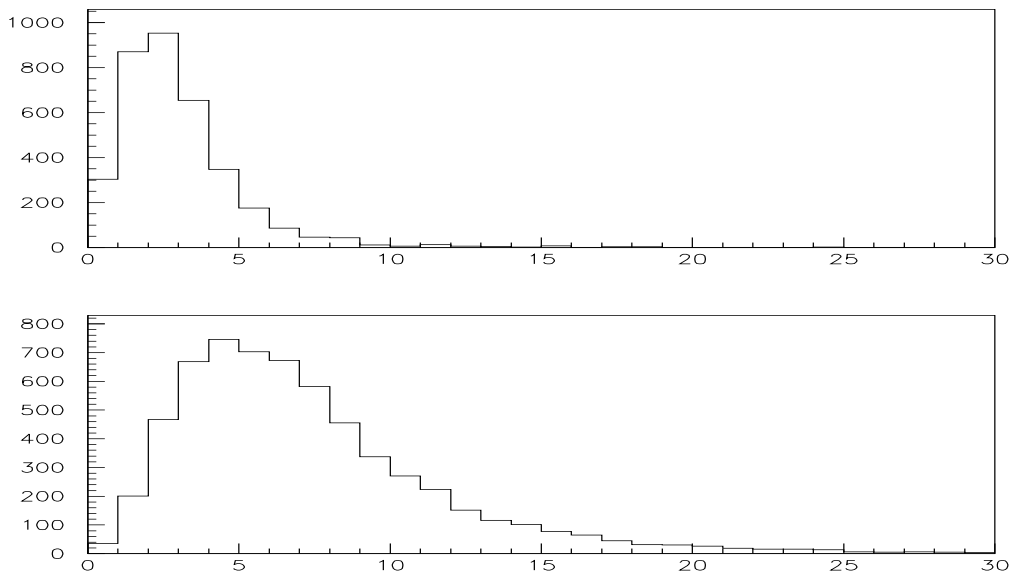

Figure 6.8: The halo energy (GeV) distributions. The top figure is for the signal muons (the other leg in the $Z \rightarrow \mu\mu$ events has to be a "tight" muon). The bottom figure is for the QCD events.

quality cuts) is N_{TL}, then the efficiency of the tight quality cuts is[2] (the error is just the Poisson statistical error):

[2]This formula is usually a good approximation, but not strictly correct in statistical theory. For example, we will run into difficulties when N_{TT} is 0, in which case both ϵ and its error will be 0, regardless of the value of N_{TL}. The correct formula is derived in [69]. The formula quoted above is sufficiently accurate for our case.

$$\epsilon = \frac{2 \times N_{TT}}{N_{TT} + N_{TL}}$$

The advantage of using the $Z \rightarrow \mu\mu$ data sample is that both W and Z muonic decays produce isolated muons with similar momentum spectra. Using the data sample is more reliable than relying on Mote Carlo simulation of the detector responses. The disadvantage of using the $Z \rightarrow \mu\mu$ data sample is the low statistics. In fact, as we will see below, the statistical error is very large and we neglect any small systematic errors due to the small differences of the $W \rightarrow \mu\nu$ and $Z \rightarrow \mu\mu$ event kinematics.

Incidentally, we cannot use a $J/\psi \rightarrow \mu\mu$ data sample despite the gain in statistics. The reason is that the muons in these events have kinematic features different from those of the $W \rightarrow \mu\nu$ or $Z \rightarrow \mu\mu$ events. They have also different isolation characteristics (they are often associated with, instead of being isolated from, jets) from the W and Z decay events.

Using the $Z \rightarrow \mu\mu$ data sample, we find the efficiencies of the tight quality cuts to be [68]:

$$\epsilon_{CF} = (61.7 \pm 2.2)\%$$

$$\epsilon_{EF} = (23.6 \pm 4.1)\%$$

These numbers were obtained assuming that there was negligible background in the 'tight-loose' sample (one of the two muons passes all cuts, no requirement on the other). As shown in Chapter 8, the background is of the

order of 10%. A new method which should be background free, is presented here. We separate the quality and timing cuts from the isolation cuts, since there should be minimal correlation between them. The efficiency of the quality cuts is determined from the $Z \rightarrow \mu\mu$ sample with both legs isolated and the efficiency of the isolation cut from the sample where both legs pass all quality cuts. We have more confidence in this new method and will use its results to calculate the cross sections.

The results of this alternative method to measure the efficiency are summarized in Table 6.2. Note that the "tight" efficiencies are consistent with the values from the first method quoted above.

CUTS	CF	EF
all quality and timing	0.735 ± 0.022	0.281 ± 0.048
isolation	0.878 ± 0.018	0.793 ± 0.075
"tight"	0.645 ± 0.023	0.223 ± 0.044

Table 6.2: Efficiencies for isolation and quality cuts and total selection efficiency for CF and EF muons.

It is also assumed that there is no p_T dependence of the efficiency above 20GeV which is our p_T cut for the $Z \rightarrow \mu\mu$ sample. This assumption is validated by the consistent results we get when we lower the p_T cut to 15GeV.

There is a definite drop in the "tight" efficiency with increased luminosity. As shown in Table 6.3, this occurs for $MITOOL = 4$. This gives rise to the slight difference observed in precleaning and postcleaning efficiencies for the CF region. Within their rather large errors, the EF efficiencies are the same

for both running periods and for all MITOOL values.

MITOOL	CF	EF
1	$(69 \pm 3)\%$	$(20 \pm 6)\%$
2	$(74 \pm 6)\%$	$(50 \pm 20)\%$
3	$(64 \pm 4)\%$	$(30 \pm 11)\%$
4	$(43 \pm 7)\%$	$(15 \pm 10)\%$

Table 6.3: The MITOOL dependence of the WZ tight selection efficiency.

Since there is a dependence on MITOOL, we cannot use the average efficiency from the complete $Z \rightarrow \mu\mu$ sample. The Z sample, when the first leg of the Z is required to be tight, will have fewer $MITOOL = 4$ events than does a truly unbiased sample. We need to weight the efficiencies in Table 6.3 for the correct MITOOL distribution of our sample. For the $W \rightarrow \mu\nu$ trigger (see the next section), this weighted efficiencies differs by 6% from the unweighted average for the complete $Z \rightarrow \mu\mu$ sample. The weighted efficiencies are

$$\begin{aligned}
\epsilon_{CF,early} &= 0.634 \pm 0.027 \\
\epsilon_{CF,middle} &= 0.611 \pm 0.031 \\
\epsilon_{CF,post-MAX} &= 0.634 \pm 0.027 \\
\epsilon_{CF,post-CENT} &= 0.586 \pm 0.037
\end{aligned}$$

We use the unweighted average efficiency for the EF due to poor statistics (see Table 6.3).

6.2 W/Z Trigger Requirements

For the cross-section analysis the same trigger for W and Z candidates was used, in order to keep the systematic errors on the ratio of the cross-sections to a minimum. The trigger simply required a single high p_T muon at all trigger levels. It was more complicated after the EF chambers were cleaned, as the CF and EF triggers were split and given different prescales. Before run 89000, the trigger used was MU_1_HIGH at Level 1 and MU_1_MAX at level 2. After run 89000, this trigger was kept but ran with a high prescale (7 in the average). A new trigger, which was restricted to only the CF region but was otherwise identical, was introduced. It was called MU_1_CENT at Level 1 and MU_1_CENT_MAX at Level 2 and had an average prescale of 2.

The Level 1 and Level 2 trigger requirements are:

- Level 1 requirements:
  - at least one muon within WAMUS region.
  - scintillator veto (beginning with run 81907).
  - Level 1.5 confirmation.
- Level 2 requirements:
  - $p_T^\mu \geq 15$ Gev/c.
  - "BEST" quality (see the discussion of the Level 2 filters below).
  - calorimeter confirmation of the muon track.

– cosmic ray rejection with "MUCTAG" (see the discussion below). and scintillator veto (beginning with run 84303).

6.2.1 W Trigger Efficiencies

The trigger efficiencies are measured with an unbiased high p_T muon ($p_T \geq$ 15GeV) sample[75]. These muons are "tight" muons as described early in this chapter, and are required to come from a trigger other than the muon trigger (such as a jet trigger), whether they satisfied the muon trigger conditions or not. By requiring "tight" muons we reduce the background in the sample and minimize the correlation between trigger and selection efficiencies. By requiring that the muons pass a trigger other than the muon trigger , we select an unbiased muon sample for trigger efficiency calculations.

The trigger efficiency is then the number of events passing the trigger in question divided by the total number of events in the sample (we take the Poisson statistical error as its error as in the tight muon selection efficiency case).

The results are summarized in Table 6.4. Below we discuss the details of the calculation.

Level 1 Trigger and Level 1.5 Confirmation

The Level 1 W/Z trigger, MU_1_HIGH is a single muon satisfying the muon CCT logic and confirmed by the OTC electronic table at Level 1.5. There is a difference between the pre-cleaning and post-cleaning periods (

CF MUONS		
TRIGGER	pre-cleaning	post-cleaning
CCT	0.785 ± 0.007	0.765 ± 0.011
OTC	0.697 ± 0.008	0.686 ± 0.013
Scint	0.983 ± 0.017	0.970 ± 0.030
Level 2	0.863 ± 0.013	0.872 ± 0.019
TOTAL	0.464 ± 0.014	0.444 ± 0.020
EF MUONS		
TRIGGER	pre-cleaning	post-cleaning
CCT	0.171 ± 0.022	0.588 ± 0.032
OTC	0.820 ± 0.054	0.759 ± 0.037
Level 2	0.724 ± 0.100	0.857 ± 0.076
TOTAL	0.102 ± 0.020	0.382 ± 0.044

Table 6.4: Trigger efficiencies for high p_T CF and EF muons. The definitions of CCT and OTC are discussed in Chapter 2. The "scint" efficiencies are discussed below.

especially for EF muons) due to the muon chamber cleaning[73] which affected the EF chambers most.

No clear p_T dependence of these efficiencies is seen in the range $p_T \geq 15$ GeV. Figures 6.9 and 6.10 show the CF trigger efficiencies which are consistent with being independent of p_T.

The scintillator (for CF only) is used to put a time stamp on muons in order to separate the in-time muons from out-of-time muons ("in-time" here means in time with the beam crossing signal). The central part of the DØ detector is covered on all the sides with scintillator counters. We reject out-

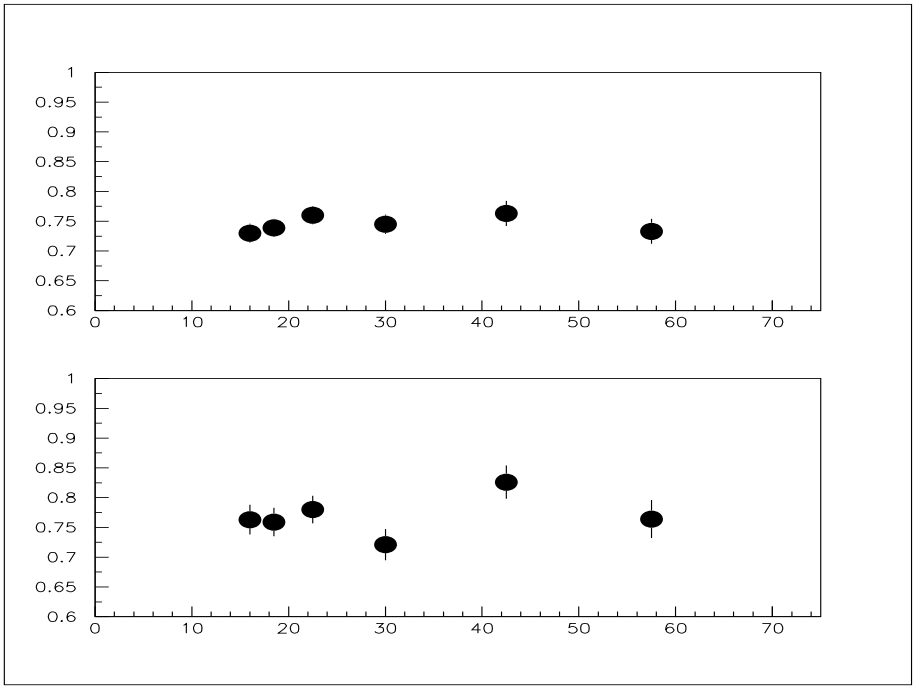

Figure 6.9: Level 1 efficiencies for CF muons for different p_T (GeV/c). The top figure is for pre-cleaning run period, the bottom figure is for post-cleaning run period.

of-time background muons from sources (such as cosmic rays) other than the $p\bar{p}$ collision at beam cross time.

The efficiency of the scintillator is calculated with $Z \rightarrow \mu\mu$ events where both muons are required to be tight muons. The efficiency is found to be $(98.3 \pm 1.7)\%$ for the pre-cleaning period and $(97.0 \pm 3.0)\%$ for the post-cleaning period.

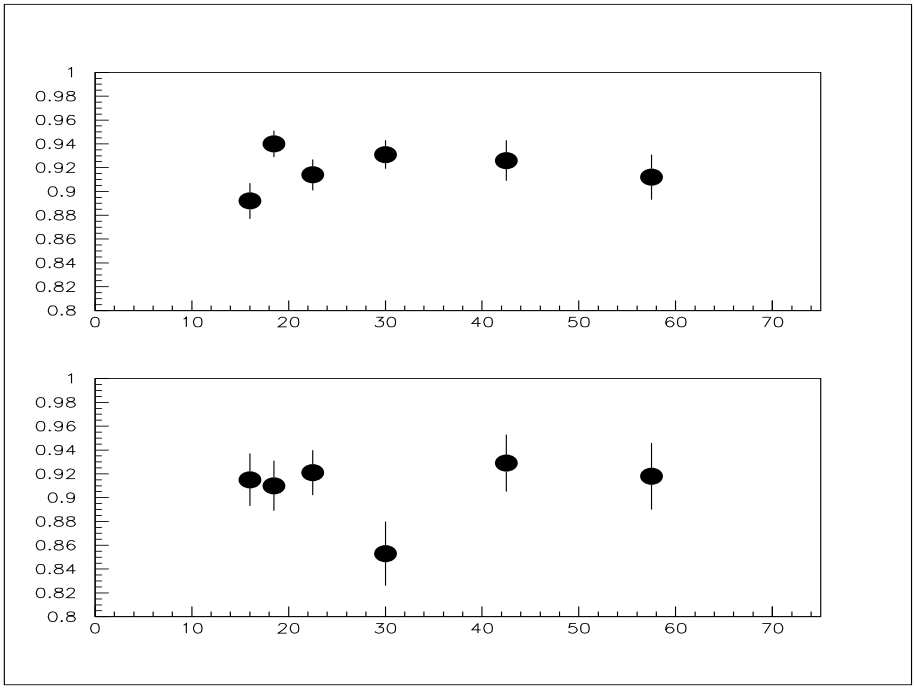

Figure 6.10: Level 1.5 efficiencies for CF muons for different p_T (GeV/c). The top one is for pre-cleaning run period, the bottom one is for post-cleaning run period.

Level 2 Filter

In the Level 2 W/Z filter MU_1_MAX, a single muon with $p_T \geq 15$GeV is required which has to satisfy a set off muon quality cuts ("BEST" muon quality). We will explain these terms below.

The Level 2 filter has both p_T dependence (Figure 6.11) and time dependence (Table 6.5). Figure 6.11 shows the Level 2 trigger efficiencies in the CF

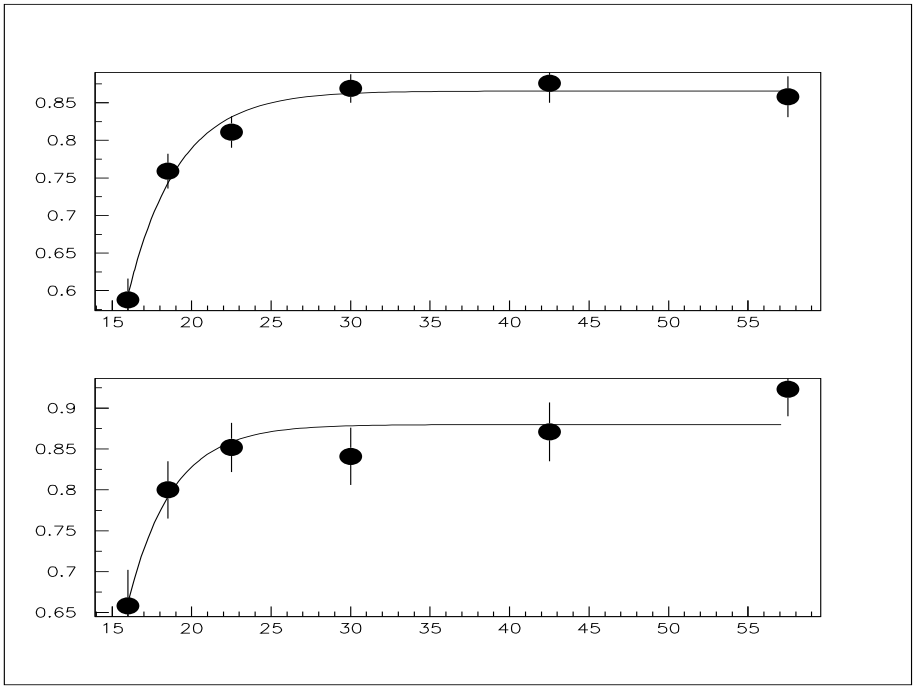

Figure 6.11: Level 2 efficiencies for CF muons for different p_T(GeV/c). The top figure is for the pre-cleaning run period, the bottom figure is for the post-cleaning run period.

as a function of p_T in the pre-cleaning and post-cleaning periods. We fit these efficiencies (ϵ) points to a function of the form

$$\epsilon = A * (1. - 0.5 * e^{C*(B-p_T)}). \tag{6.1}$$

where A is the plateau efficiency at high p_T, B is the 50% relative efficiency point, and C characterizes the steepness of the turn on at low p_T. Fig. 6.11

shows the p_T turn on curves for the pre-cleaning and post-cleaning CF muons. Table 6.5 gives the fit results together with the average value for muons with $p_T \geq 20$ GeV/c (using Monte Carlo simulation to find the relative proportion of the W at each p_T bin).

CF MUONS		
FIT RESULTS	pre-cleaning	post-cleaning
χ^2/ndf	0.6	1.0
A (plateau)	0.866 ± 0.014	0.880 ± 0.021
B (50 % eff)	14.5 ± 0.6	14.0 ± 1.3
C (turn on)	0.32 ± 0.09	0.36 ± 0.19
AVERAGE $p_T \geq 20$	0.848 ± 0.011	0.865 ± 0.017
EF MUONS		
AVERAGE $p_T \geq 20$	0.731 ± 0.087	0.857 ± 0.076

Table 6.5: MU_1_MAX trigger efficiencies for high p_T CF and EF muons. The χ^2 per degree of freedom is labelled χ^2/ndf.

Most of the inefficiency of the MU_1_MAX filter can be accounted for by the requirement of CAL_CONFIRM and BEST. Each of these requirements is about 95% efficient (with a rejection factor of about 2) which explains why the plateau level is close to 90%.

- CAL_CONFIRM:

  "CAL_CONFIRM" stands for calorimeter confirmation. It requires the energy deposition along the muon track to be at least 5 GeV.

  The efficiency of the CAL_CONFIRM requirement can be studied with

the monitor filter MU_1_MON, which is the same as MU_1_MAX except it does not require CAL_CONFIRM. Due to heavy prescaling, we have very few events from MU_1_MON in the post-cleaning run period. In the pre-cleaning run period we calculate the efficiency of the CAL_CONFIRM requirement to be 0.936 ± 0.016.

- BEST:

  "BEST" is the requirement that the muons must have $IFW4 = 0$ (see the discussion on IFW4 early this chapter).

  The efficiency of the BEST requirement can be studied with the monitor filter MU_1_HIGH, which is the same as MU_1_MAX except it does not require BEST. Again, due to heavy prescaling, we have very few events from MU_1_HIGH in the post-cleaning run period. In the pre-cleaning run period we calculate the efficiency of the BEST requirement to be 0.970 ± 0.012.

Cross-checks with a $Z \rightarrow \mu\mu$ Sample

Despite its low statistics the $Z \rightarrow \mu\mu$ data sample can be used to cross-check the trigger efficiencies obtained from the unbiased muon sample. If both muons pass the tight selection cuts and one of the muons satisfies the MU_1_MAX trigger, we consider the other muon unbiased and use it to calculate the trigger efficiencies. Table6.2.1 shows that there is good agreement in the Level 1 efficiency for CF muons, but the Level 2 CF efficiency calculated from the $Z \rightarrow \mu\mu$ sample is higher than that from the unbiased muon

sample. However, the calculation from the $Z \rightarrow \mu\mu$ events does not include the CAL_CONFIRM efficiency (the results of the on-line calculation are not stored). If allowance is made for that term, the efficiencies agree. Within the extremely limited EF statistics there is good agreement.

CF: unbiased muon sample			
RUN RANGE	Level 1	Level 1.5	Level 2
pre-cleaning	78 ± 1	70 ± 1	86 ± 1
post-cleaning	76 ± 1	69 ± 1	87 ± 2
CF: Z sample			
pre-cleaning	69 ± 4	92 ± 3	94 ± 2
post-cleaning	57 ± 9	94 ± 6	92 ± 8
EF: unbiased muon sample			
RUN RANGE	Level 1	Level 1.5	Level 2
pre-cleaning	17 ± 2	82 ± 5	72 ± 10
post-cleaning	59 ± 3	76 ± 4	86 ± 8
EF: Z sample			
pre-cleaning	19 ± 10	100 ± 33	100 ± 33
post-cleaning	75 ± 15	100 ± 17	75 ± 25

Table 6.6: Cross-check of unbiased trigger efficiencies using the $Z \rightarrow \mu\mu$ data sample. All values are given in %.

6.2.2 Z Trigger Efficiencies

Under the assumption that the trigger requirements (discussed in the previous sections) affect both muons from the Z decay in an uncorrelated fashion, we can calculate the trigger efficiency ϵ_Z for Z candidates, where

both muons are in the CF, from the trigger efficienciy ϵ_W for W candidates in the CF

$$\epsilon_Z = 2\epsilon_W - \epsilon_W^2 \tag{6.2}$$

However Monte Carlo modeling shows that this is not so. The main reason is the "MUCTAG" cut. This cut rejects muons if there are hits or tracks on the opposite side of the muon detector. This is designed to remove cosmic rays but unfortunately also loses real Z events. Even after we apply a non-back-to-back cut offline ($\Delta\phi < 170°$ or $\Delta\theta < 170°$) in order to reject cosmic rays, the MUCTAG cut rejects additional events. A plot of the Z trigger efficiency versus $\Delta\phi$ shows the depletion from this cut (Fig. 6.12). On the average 5% of the otherwise good Z events fail because of this. We use in our analysis expression (6.2) and calculate correction to it.

Another correction to 6.2 is due to the fact that the W trigger efficiency ϵ_W is calculated for muons with $p_T \geq 20$ GeV. However, in the case where the offline p_T cuts on the Z muons are 20 and 15 GeV, it can happen that a muon with p_T between 15 and 20 is the one which satisfies the W trigger. The efficiency for such muons is much lower due to the Level 2 p_T threshold. Since this is an infrequent occurrence, on average the effect is small (1-2%).

Table 6.7 shows the corrections to (6.2) needed to be applied for each running period. In the case of a back-to-back acceptance cut (BTB in Table 6.7) of 150° (the back-to-back track is searched over each chamber. Each chamber covers about 20° in ϕ. We use 150° instead of 160° to be conservative)

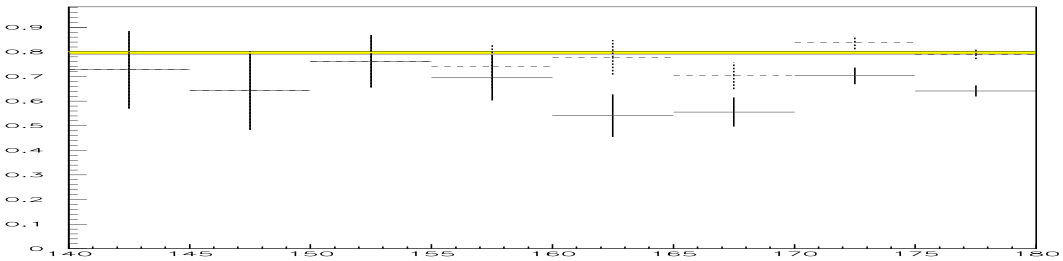

Figure 6.12: The $Z \rightarrow \mu\mu$ trigger efficiency versus $\Delta\phi$ (degrees) is shown for CF-CF Monte Carlo events. There is a drop near $\Delta\phi = 180°$. This is caused by the MUCTAG cut removing back-to-back muons. The band is the $Z \rightarrow \mu\mu$ trigger efficiency using the formula (6.2). The solid crosses show the actual efficiencies without the back-to-back cut. The dotted crosses show the efficiencies with the back-to-back cut.

and p_T cuts of 20 GeV on both legs, we expect that the Z trigger efficiency is correctly given by formula (6.2). The table confirms that this is true (within the statistical accuracy of the Monte Carlo sets). Since in this analysis we used a $\Delta\phi$ cut of 170° and p_T cuts of 20 and 15 GeV, we use corrections of 0.935 ± 0.020, 0.945 ± 0.020, and 0.871 ± 0.040 for the three running periods.

As far as can be ascertained within the limited statistics, the efficiency for CF-EF Z candidates, where the CF leg is required to have triggered, is the same as for CF W candidates. Thus no such correction is needed.

RUN PERIOD (p_T cut)	No BTB	BTB 170	BTB 160	BTB 150
Early (20,15)	.807	.935	.984	.987
Early (20,20)	.815	.948	.994	.997
Middle (20,15)	.790	.945	.990	.995
Middle (20,20)	.800	.960	1.006	1.012
Late (20,15)	.746	.871	.918	.925
Late (20,20)	.760	.892	.938	.945

Table 6.7: Trigger efficiency corrections for Z events with respect to formula (6.2) using W trigger efficiency. As the back-to-back (BTB) angle cut increases, the correction approaches one. The uncertainty in these numbers is $\pm 2\%$ for Early and Middle MUSMEAR versions, and $\pm 4\%$ for the LATE MUSMEAR version (these are statistical errors of the Monte Carlo calculations).

Chapter 7

Data Samples of $W \rightarrow \mu\nu$ and $Z \rightarrow \mu\mu$

Based on the cuts discussed in the previous chapters, we select the $W \rightarrow \mu\nu$ and $Z \rightarrow \mu\mu$ candidate sample. The events

- Pass the W or Z acceptance cuts;
- Pass the W or Z trigger cuts (in the case of CF-EF Z candidates, the CF muon must pass the trigger);
- Have 1 tight muon but less than 2 loose muons for $W \rightarrow \mu\nu$;
- Have at least 1 tight muon and at least 2 loose muons for $Z \rightarrow \mu\mu$.

Tables 7.1 and 7.2 give the number of events in the final $W \rightarrow \mu\nu$ and $Z \rightarrow \mu\mu$ samples and the corresponding integrated luminosity. We have already shown the distributions of the W transverse mass, Z invariant mass and the muon η (in W events) in Chapter 5. Figures 7.1 shows additional distributions of some kinematic quantities for the final samples. The Monte Carlo distribution (dashed line) describes the data reasonably well. Note,

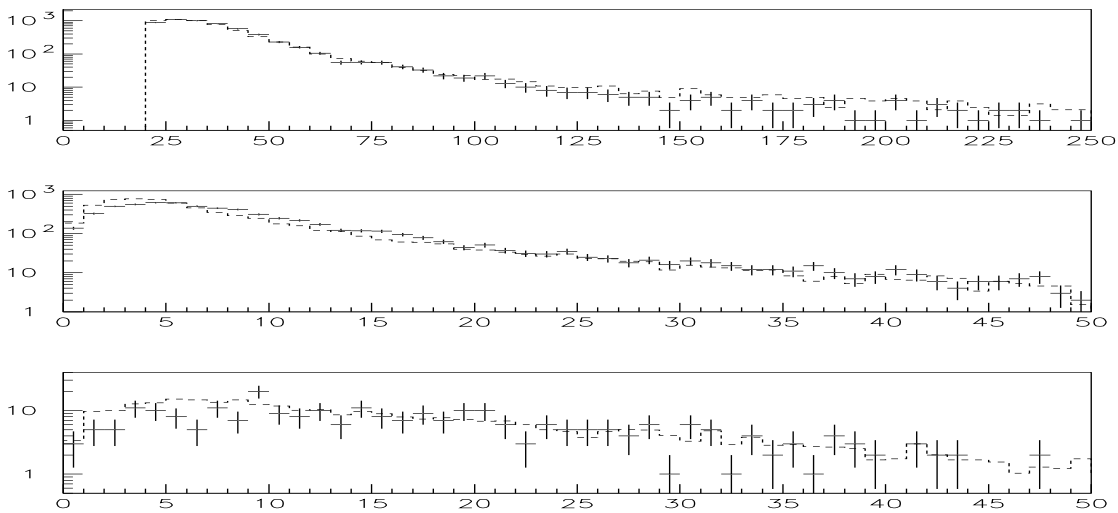

Figure 7.1: Some kinematic quantities (the crosses are for data, and the histograms are for Monte Carlo simulation. No background – about 20% for W and 10% for Z events – is subtracted). The top figure is the transverse momentum distribution of the muon in the W events, the middle figure is the transverse momentum distribution of the W, and the bottom figure is the transverse momentum distribution of the Z. The unit is GeV/c for all three figures.

however, that the measured W transverse momentum distribution is somewhat less steep than the Monte Carlo distribution.

RUN PERIOD	CF	EF	Total
Early	1762	51	1813
Middle	2715	55	2770
Late-MAX	934	203	1137
Late-CENT	2812	—	2812

Table 7.1: Number of $W \rightarrow \mu\nu$ events in the final data sample

Run Periods	CF-CF	CF-EF	EF-EF	Total
Early	59	29	0	88
Middle	114	43	0	157
Late-MAX	32	22	2	54
Late-CENT	89	67	0	156

Table 7.2: Number of $Z \rightarrow \mu\mu$ events in the final data sample

Chapter 8

Background

In this chapter we discuss the backgrounds for the W and Z sample separately.

8.1 W Backgrounds

We consider the following types of backgrounds: cosmic rays and combinatorics, general QCD processes, 1-legged $Z \rightarrow \mu\mu$ events, and W or Z decays into τ, where the τ subsequently decays into a muon.

8.1.1 Cosmic Rays and Combinatorics

The cosmic/combinatoric muon background is estimated from the data using the floating time t_f distributions (see Chapter 6 for detailed discussion on t_f). The floating time t_f is determined with the assumption that the muon is coming from the vertex. Therefore the t_f distribution of the $W \rightarrow \mu\nu$ events (called "signal distribution", which should be narrow and centered around

$t_f = 0$ ns) and the t_f distribution of the cosmic/combinatoric muons (called "background distribution", which is expected to be broad and is experientally found to peak around $t_f = 100$ ns due to the trigger bias) are characteristically different. In order to estimate the cosmic/combinatoric background, we plot the t_f distribution of the final sample (called "sample distribution") and estimate the cosmic/combinatoric background by fitting it with the shape of a signal distribution and a background distribution.

We get the signal (or background) distribution from the data from all the triggers by selecting those events which are clearly signal (or background), and whose t_f distribution is similar to the signal (or background) events in the final $W \rightarrow \mu\nu$ sample. We achieve this by making the cuts on the quantities uncorrelated with t_f as tight as possible to get the signal distribution (for the background distribution, those cuts are reversed to approximate the background events). On the quantities correlated with t_f (especially muon system quantities such as IFW4[1]), we make similar cuts as in the $W \rightarrow \mu\nu$ event selection.

Below we list the selection criteria for the events giving the signal distribution and background distribution:

- Selection criteria for signal distribution:

    1. Muon $p_T > 5$ GeV/c;

    2. A matching track in CD;

[1]See section 6.1.1 for discussion on IFW4.

3. Global fit $\chi^2 < 5$;
4. Calorimeter energy deposition in the $\Delta R \leq 0.2$ cone $E(\Delta R \leq 0.2) > 5$ GeV;
5. Non-bend view impact parameter $b_{nb} < 20$cm;
6. 3-layer track;
7. MTC cuts;
8. $IFW4 = 0$.

The $\chi^2 < 5$, $E(\Delta R \leq 0.2) > 5$ GeV and $IFW4 = 0$ are very powerful cuts to reject cosmic rays/combinatorics. With the additional cuts above, we expect very little contamination from cosmic rays/combinatorics. See the systematic error discussion below on how we account for the effect of the remaining background in the signal sample.

- Selection criteria for background distribution:

  1. no matching CD track;
  2. Calorimeter energy deposition in the $\Delta R \leq 0.2$ cone $E(0.2) < 0.5$ GeV;
  3. Non-bend view impact parameter $b_{nb} > 40.0$cm;
  4. 3-layer track;
  5. HFRAC≤ 0.5;
  6. $IFW4 = 0$;

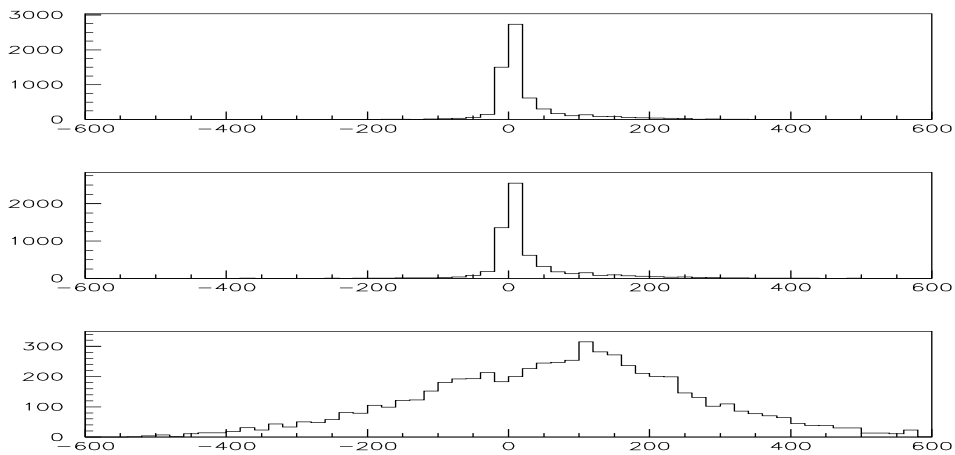

Figure 8.1: The t_f distributions (for the CF only). The top, middle and bottom figures are the sample, signal and background distributions respectively. The unit of t_f is ns.

Figure 8.1 shows the sample, signal and background distributions of t_f in the CF. Figure 8.2 shows the CF fitted results. Note that in order to get a better fit, we did not apply the t_f cut, because the tails of the distributions are important for the fit. Since we do have the t_f cut in the final sample, we will take that factor into account in the background calculation after the fit.

While the statistical error is given by the fitting procedure, the systematic error can come from two sources:

- Different run periods: the t_f distribution changes over long period of run-time which is due to changes of the chamber conditions. We repeat the above fitting procedure by using the pre-cleaning data and post-cleaning data. We compare the two fitting results in order to get systematic errors.

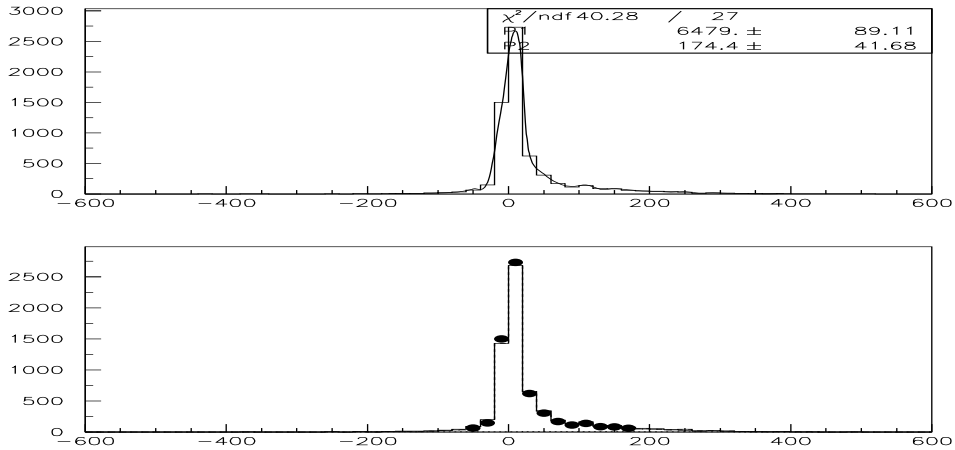

Figure 8.2: Fitted results for the distribution (for the CF only). The top figure shows the fit and the sample. The bottom figure shows the data points together with the sum of signal and background (the solid line). The signal (dashed line) coincides the solid line, and the background distribution (dotted line) is barely visible at the bottom. The unit of t_f is ns.

- Impurity of the signal t_f distribution: despite all the powerful cuts against cosmic rays/combinatorics, as listed above, some cosmic rays and combinatorics may still remain and contaminate the signal distribution. To estimate the effect of this impurity, we repeat the fitting procedure above, but use slightly different cuts for the signal distribution. We require scintillator confirmation in addition, but relax the global fit χ^2 cut to 10.0 and the $E(\Delta R \leq 0.2)$ cut to 3.0 so that we still have enough statistics for the fit. The change in the result is taken to be the systematic error due to the impurity of the signal distribution.

In summary, the cosmic/combinatoric background for the CF and EF is

(the errors quoted are the statistical error and the systematic errors due to averaging over long run periods and the impurity of the signal distribution as discussed above):

$$b_{cosmics,CF} = (1.8 \pm 0.4 \pm 0.4 \pm 0.5)\%$$
$$b_{cosmics,EF} = (6.5 \pm 2.1 \pm 1.5 \pm 1.8)\%$$

8.1.2 QCD Processes

The dominant QCD processes contributing to the $W \rightarrow \mu\nu$ background are the muonic decays of the b and c quarks. The background due to hadrons leaking out of the calorimeter and $\pi(K) \rightarrow \mu$ decay in flight can be ignored due to the thickness of the calorimeter and the muon system [59], and also due to the high p_T cut.

The QCD background events have a non-isolated muon due to the relative small masses of the b and c quarks, different from real $W \rightarrow \mu\nu$ events. As t_f in the cosmic background case, we use an isolation variable to measure the QCD background. The parameter we use is "halo energy" $E(0.2 \leq \Delta R \leq 0.6)$ which is the calorimeter energy deposition between the two cones with $\Delta R = 0.2$ and $\Delta R = 0.6$.

The signal events are the same as the $W \rightarrow \mu\nu$ events in the final sample with an additional cut that no jet is in the opposite half of the detector (in ϕ with respect to the muon). The background events pass the same cuts as the $W \rightarrow \mu\nu$ events in the final sample. However, their p_T is between 5 GeV and

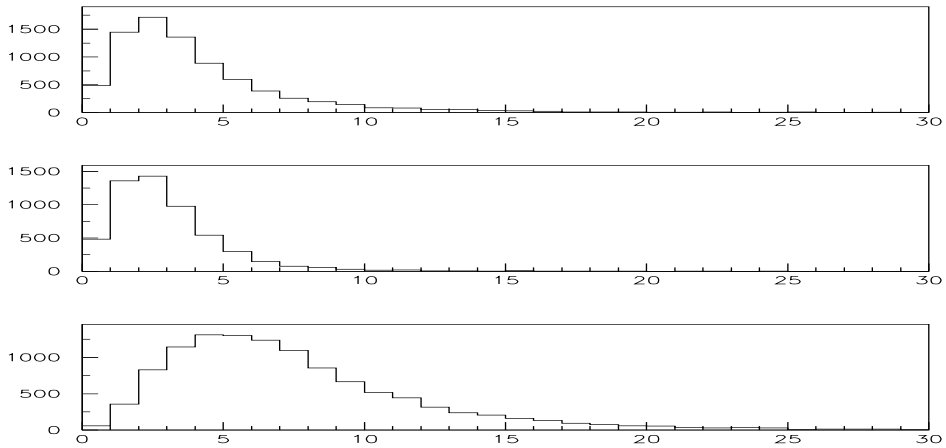

Figure 8.3: Halo energy distributions (for the CF only). The top figure is for the sample; the middle figure is for the signal muons; the bottom figure is for the background. The unit of the halo energy is GeV.

10 GeV (the low p_T muons are mostly from b and c decays [60]).

Figure 8.3 shows the sample, signal and background distributions of the halo energy. Figure 8.4 shows the fitted result. Since we do have the halo energy cut in the final sample, we need to take that factor into account in the background calculation.

The systematic error can be measured by using signal and background distributions from different run ranges and repeat the fit. We also vary the definition of the signal by requiring there are no jet at all in the event, and vary the definition of the background by requiring the p_T range to be between 10 GeV and 15 GeV. The differences between these results are a measurement of the systematic effect.

The systematic error can come from the following sources:

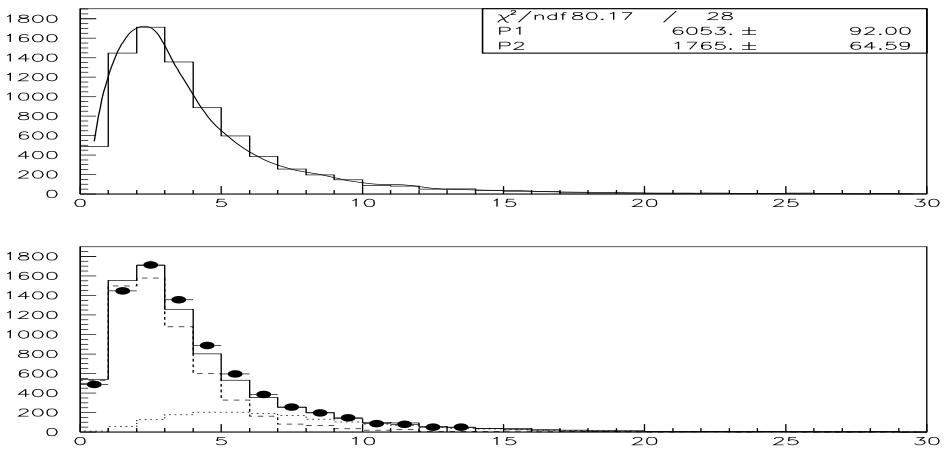

Figure 8.4: Fitted results (for the CF only). The top figure shows the fitted results. The bottom figure shows the data points, together with the sum of signal and background (the solid line), the signal (dashed line) is close to the solid line, and the background distribution (dotted line) is visible at the bottom. The unit of the halo energy is GeV.

- Different run periods: the change of conditions over the long runtime periods. This error is measured by repeating the fitting procedure for the pre-cleaning and post-cleaning periods, and also swapping the pre-cleaning and post-cleaning distributions (for example, use background distribution from the post-cleaning period in the fit for pre-cleaning sample). The differences in these fits give a measurement of the systematic error.

- Impurity of the signal distribution: we get the signal distribution by requiring no jet in the opposite half of the detector (in ϕ with respect to the muon). This requirement rejects most QCD events. To examine

the effect of remaining QCD background, we repeat the fitting procedure above requiring no jet at all in the event. We take the difference in the results as the systematic error due to impurity of the signal distribution.

- Impurity of the background distribution: since muons from the b and c decays dominate the spectrum in the low p_T range, we expect few muons from W decay in our background sample. To measure the effect of residual muons from W decay, we repeat the fit using a background sample in the p_T range between 10 to 15 GeV and take the difference as systematic error.

The QCD backgrounds in different regions are listed below. The quoted errors are the statistical errors and the the errors due to impurity of the signal distribution, impurity of the background distribution, and different run periods.

$$b_{QCD,CF} = (5.7 \pm 0.2 \pm 0.5 \pm 1.1 \pm 1.3)\%$$
$$b_{QCD,EF} = (11.4 \pm 1.4 \pm 2.0 \pm 0.7 \pm 3.8)\%$$

8.1.3 One-legged $Z \rightarrow \mu\mu$

If one of the muons in the $Z \rightarrow \mu\mu$ event is not detected, the event will have a high p_T and isolated muon with large $\not{E}_T$ and can fake a $W \rightarrow \mu\nu$ event. To measure this background, we use the Monte Carlo events (the generation of those events is described in Chapter 4). The background is measured by

the ratio of the acceptance of $Z \rightarrow \mu\mu$ (as a $W \rightarrow \mu\nu$ event) and $W \rightarrow \mu\nu$ and the ratio of the W, Z cross section (we use the world average value 10.9 ± 0.5 for R[11]).

$$b_{Z\rightarrow\mu\mu} = \frac{\mathcal{A}_{ZasW}}{\mathcal{A}_{W\rightarrow\mu\nu}}/R$$

The results are shown below (the errors are Monte Carlo statistical errors and systematic errors):

$$b_{one-legged-Z,CF} = (8.3 \pm 0.3 \pm 0.4)\%$$
$$b_{one-legged-Z,EF} = (8.4 \pm 0.3 \pm 0.4)\%$$

Calculating this background for the pre-cleaning and post-cleaning periods separately, we notice that the background is lower in the post-cleaning period. This is due to the cleaned muon chambers being more efficient at finding the other leg in $Z \rightarrow \mu\mu$ events, and thus reducing this background.

8.1.4 $W \rightarrow \tau \rightarrow \mu$ and $Z \rightarrow \tau\tau \rightarrow \mu$

For these events the muon p_T spectrum is much softer than that of the muons which come directly from the decay $W \rightarrow \mu\nu$ Therefore we expect that these events have a lower acceptance than that for $W \rightarrow \mu\nu$ in addition to the suppression due to the small branching ratio $Br(\tau \rightarrow \mu\nu) \sim 17\%$.

We generated about 20,000 $W \rightarrow \tau \rightarrow \mu$ events with ISAJET, then processed these through DØ GEANT (with MUSMEAR) and DØ RECO. We calculated the acceptance $\mathcal{A}_{W\rightarrow\tau\rightarrow\mu}$ for these decays (using the same $W \rightarrow \mu\nu$ acceptance cuts as for the final sample). The $W \rightarrow \tau \rightarrow \mu$ background is then

$$b_{W\rightarrow\tau\rightarrow\mu} = \frac{\mathcal{A}_{W\rightarrow\tau\rightarrow\mu}}{\mathcal{A}_{W\rightarrow\mu\nu}} \times Br(\tau \rightarrow \mu\nu)$$

The statistical error of $b_{W\rightarrow\tau\rightarrow\mu}$ can be calculated from the number of Monte Carlo events we have for the $W \rightarrow \tau \rightarrow \mu$ and $W \rightarrow \mu\nu$ decays. The systematic error is taken from the $W \rightarrow \mu\nu$ acceptance. This is conservative because the uncertainty in the two acceptances tends to cancel. The results for this background are:

$$b_{W\rightarrow\tau\rightarrow\mu,CF} = (5.3 \pm 0.44)\%$$

$$b_{W\rightarrow\tau\rightarrow\mu,EF} = (6.8 \pm 0.87)\%$$

The $Z \rightarrow \tau\tau \rightarrow \mu$ background is calculated in a similar way, giving

$$b_{Z\rightarrow\tau\tau\rightarrow\mu,CF} = (0.8 \pm 0.2)\%$$

$$b_{Z\rightarrow\tau\tau\rightarrow\mu,EF} = (1.3 \pm 0.4)\%$$

8.2 Z Backgrounds

We consider the following types of backgrounds: cosmic rays/combinatorics, general QCD processes, $Z \rightarrow \tau\tau \rightarrow \mu\mu$, and Drell-Yan production of dimuons.

8.2.1 Cosmic Rays

The method is similar to that used in the $W \rightarrow \mu\nu$ case. The difference is that at least one of the muons in the $Z \rightarrow \mu\mu$ event has to pass the $t_f \leq 100$ns cut. The fitting procedures are as for $W \rightarrow \mu\nu$. The cosmic/combinatoric background is listed below(the errors quoted are the statistical error and the systematic errors are due to different run periods and impurity of the signal):

$$b_{CFCF} = (1.8 \pm 1.7 \pm 0.9 \pm 1.1)\%$$

$$b_{CFEF} = (4.1 \pm 4.7 \pm 1.2 \pm 1.4)\%$$

8.2.2 QCD Processes

The method is similar to that used in the $W \rightarrow \mu\nu$ case. The difference is that at least one of the muons in the $Z \rightarrow \mu\mu$ event has to pass the $E(0.2 \leq \Delta R \leq 0.6) \leq 6$ cut. The fitting procedures are as for $W \rightarrow \mu\nu$.

The QCD backgrounds in different detector regions are listed below. The quoted errors are the errors due to impurity of the signal distribution, impurity of the background distribution, different run periods, and the statistical error.

$$b_{CFCF} = (4.10 \pm 1.13)\%$$

$$b_{CFEF} = (3.59 \pm 5.24)\%$$

8.2.3 $Z \to \tau\tau \to \mu\mu$

In these events the muon p_T is much softer than the muon p_T in $Z \to \mu\mu$ decays. Therefore we expect that these events have a lower acceptance than that for $Z \to \mu\mu$ in addition to the suppression due to the square of the small branching ratio $(Br(\tau \to \mu\nu))^2 \sim 0.029$.

We generated about 20,000 $Z \to \tau\tau \to \mu\mu$ events with ISAJET, then processed these through DØ GEANT (with MUSMEAR) and DØ RECO. We calculated the acceptance $\mathcal{A}_{Z\to\tau\tau\to\mu\mu}$ (using the same $Z \to \mu\mu$ acceptance cuts as for the final sample). The $Z \to \tau\tau \to \mu\mu$ background is then

$$b_{Z\to\tau\tau\to\mu\mu} = \frac{\mathcal{A}_{Z\to\tau\tau\to\mu\mu}}{\mathcal{A}_{Z\to\mu\mu}} \times Br(\tau \to \mu\nu) \times Br(\tau \to \mu\nu)$$

The statistical error of $b_{Z\to\tau\tau\to\mu\mu}$ can be calculated from the number of Monte Carlo events we have for $Z \to \tau\tau \to \mu\mu$ and $Z \to \mu\mu$. The systematic error is taken from the $Z \to \mu\mu$ acceptance. The results are:

$$\begin{aligned} b_{Z\to\tau\tau\to\mu\mu,CFCF} &= (0.7 \pm 0.1)\% \\ b_{Z\to\tau\tau\to\mu\mu,CFEF} &= (0.5 \pm 0.1)\% \\ b_{Z\to\tau\tau\to\mu\mu,EFEF} &= (0.7 \pm 0.3)\% \end{aligned}$$

8.2.4 Drell-Yan Background

The process $q\bar{q}' \to \gamma \to \mu\mu$ has a signature similar to $q\bar{q}' \to Z \to \mu\mu$. We are only interested in the later process. The former process and the correspond-

ing interference amplitude for both processes considered to be the Drell-Yan background. We estimated this background using Monte Carlo simulation. In the manner similar to that in the $Z \rightarrow \tau\tau \rightarrow \mu\mu$ background, we estimated the Drell-Yan background to be (for the CF and EF regions):

$$b_{Drell-Yan} = (1.7 \pm 0.3)\%$$

8.3 Summary of the Background

We calculate the cosmics/combinatorics and QCD backgrounds as a fraction of the candidate sample while the other backgrounds are estimated as fractions of the $W \rightarrow \mu\nu$ signal. Therefore, N_W is related to the number of observed candidates N_{obs} by:

$$N_W \times (1 + b_{Z\rightarrow\mu\mu} + b_{W\rightarrow\tau\rightarrow\mu} + b_{Z\rightarrow\tau\tau\rightarrow\mu}) = N_{obs} \times (1 - b_{cosmic} - b_{QCD})$$

We can easily convert this expression into the conventional formula to express the relationship between N_W and N_{obs}

$$\begin{aligned} N_W &= N_{obs} \times (1 - b) \\ &= N_{obs} \times (1 - b_{cosmic} - b_{QCD} - b'_{Z\rightarrow\mu\mu} - b'_{W\rightarrow\tau\rightarrow\mu} - b'_{Z\rightarrow\tau\tau\rightarrow\mu}) \end{aligned}$$

where

$$b'_{Z\rightarrow\mu\mu} = \frac{(1 - b_{cosmic} - b_{QCD})}{(1 + b_{Z\rightarrow\mu\mu} + b_{W\rightarrow\tau\rightarrow\mu} + b_{Z\rightarrow\tau\tau\rightarrow\mu})} \times b_{Z\rightarrow\mu\mu}$$

Background	W, CF	W, EF
cosmic/combinatorics	0.018 ± 0.008	0.065 ± 0.032
QCD	0.057 ± 0.018	0.114 ± 0.046
1-legged Z	0.068 ± 0.004	0.056 ± 0.004
$W \to \tau \to \mu$	0.044 ± 0.004	0.048 ± 0.006
$Z \to \tau\tau \to \mu\mu$	0.007 ± 0.002	0.009 ± 0.003
Total	0.19 ± 0.02	0.29 ± 0.06

Table 8.1: W Backgrounds

Background	Z, CFCF	Z, CFEF
cosmic/combinatorics	0.018 ± 0.018	0.041 ± 0.047
QCD	0.041 ± 0.011	0.036 ± 0.052
$Z \to \tau\tau \to \mu\mu$	0.006 ± 0.001	0.005 ± 0.001
Drell-Yan	0.016 ± 0.003	0.015 ± 0.003
Total	0.08 ± 0.02	0.10 ± 0.07

Table 8.2: Z Backgrounds

$$
\begin{aligned}
b'_{W\to\tau\to\mu} &= \frac{(1 - b_{cosmic} - b_{QCD})}{(1 + b_{Z\to\mu\mu} + b_{W\to\tau\to\mu} + b_{Z\to\tau\tau\to\mu})} \times b_{W\to\tau\to\mu} \\
b'_{Z\to\tau\tau\to\mu} &= \frac{(1 - b_{cosmic} - b_{QCD})}{(1 + b_{Z\to\mu\mu} + b_{W\to\tau\to\mu} + b_{Z\to\tau\tau\to\mu})} \times b_{Z\to\tau\tau\to\mu}
\end{aligned}
$$

The same procedure is used for the $Z \to \mu\mu$ backgrounds. Table 8.1 and 8.2 show all the backgrounds as fractions of the candidate sample.

Chapter 9

Results

9.1 W and Z Cross-sections

The cross-section for $W \to \mu\nu$ and $Z \to \mu\mu$ are calculated from the formula

$$\sigma \cdot B = \frac{N - B}{\mathcal{L}ARST}$$

where N is the number of W or Z candidates, B is the estimated background, $\mathcal{L}$ is the luminosity, A is the acceptance, and R, S, and T are the reconstruction, selection, and trigger efficiencies. All these numbers have been measured or calculated as explained in the previous sections.

In order to check for consistency, we consider four running periods and trigger combinations, as discussed in Chapter 4. If we have correctly taken into account all the variations due to changes in the detector and luminosity effects, the cross-sections from each of these periods should be equal. Table 9.1 shows that this is approximately the case. Three of the four data sets show consistent

results, but the 'Late-CENT' values are suspiciously low. The W cross-section is $13 \pm 4\%$ [72] below that for 'Late-MAX' which ran simultaneously with that filter. The prescales were higher for 'Late-MAX', and the data were taken at a lower luminosity. The average luminosity for W candidates for these two filters were $7 \times 10^{30} cm^{-2} sec^{-1}$ for 'Late-MAX' and $9 \times 10^{30} cm^{-2} sec^{-1}$ for 'Late-CENT'. By comparison, the 'Early' and 'Middle' result from runs which were not simultaneous, but ran without major detector changes, had a similar luminosity difference, $4 \times 10^{30} cm^{-2} sec^{-1}$ and $6 \times 10^{30} cm^{-2} sec^{-1}$.

RUNNING	W-CF	Z-CF/CF	Z-CF/EF
Early	2251 ± 66	175 ± 25	156 ± 32
Middle	2306 ± 54	219 ± 22	152 ± 26
Late-MAX	2278 ± 92	189 ± 36	181 ± 43
Late-CENT	1986 ± 46	147 ± 21	155 ± 21

Table 9.1: Cross-sections times the muonic branching ratio (in nb) for W and Z events where there was a good CF muon trigger. The errors are statistical only; the systematic error for each individual entry is typically 10%.

Due to concerns about high luminosity and multiple interaction effects we disregard the MU_1_CENT data and restrict our results in the post-cleaning period to data collected under the MU_1_MAX trigger. We also remove the pre-cleaning EF data, because they add only a minor gain in statistics but a large systematic error in the acceptance. Also, in order to minimize the systematic error in the ratio calculation, we require a good CF muon in the trigger. This restricts the W cross-section to a CF-only analysis, but allows

CF-EF Z candidates if the CF leg passed the trigger.

The cross sections times the muonic branching ratio are found to be (the errors quoted are statistical, systematic and luminosity errors):

$$\begin{aligned} \sigma_W \cdot Br(W \to \mu\nu) &= (2.283 \pm 0.038 \pm 0.161 \pm 0.194)nb \\ \sigma_Z \cdot Br(Z \to \mu\mu) &= (0.198 \pm 0.014 \pm 0.020 \pm 0.016)nb \end{aligned}$$

9.2 R_μ

The cross-section ratio R_μ $(= \frac{\sigma_W \cdot Br(W \to \mu\nu)}{\sigma_Z \cdot Br(Z \to \mu\mu)})$ is found to be (the errors quoted are statistical, systematic errors):

$$R_\mu = 11.55 \pm 0.87 \pm 0.81$$

In the calculation of R_μ, many systematic effects cancel partially or completely. The systematic error, which is 7% for the W cross-section and 10% for the Z cross-section (excluding the luminosity error), is only 7% on the ratio. The sources of systematic error for the W and Z cross-sections and R_μ are given in Table 9.2. The luminosity error cancels completely. The acceptance errors, the largest of which is the one for the Z cross-section, enter significantly into the calculation of R, and remain the largest systematic uncertainties. The next largest source of error comes from the background estimations, since these errors rather add than cancel. As a technical note, although we can use error

propagation to find the errors of R_μ, it is easier to do the calculation using Monte Carlo method[74].

ERROR	$\sigma \cdot BR(W)$	$\sigma \cdot BR(Z)$	Ratio
Statistics	$\pm$ 2%	$\pm$ 7%	$\pm$ 7%
Background	$\pm$ 2%	$\pm$ 2%	$\pm$ 3%
Acc-MC Stats	$\pm$ 1%	$\pm$ 3%	$\pm$ 3%
Acc-PDF Var	$\pm$ 1%	$\pm$ 3%	$\pm$ 2%
Acc-MUSMEAR	$\pm$ 3%	$\pm$ 6%	$\pm$ 3%
Reconstruction	$\pm$ 2%	$\pm$ 5%	$\pm$ 2%
Selection	$\pm$ 4%	$\pm$ 2%	$\pm$ 2%
Trigger	$\pm$ 3%	$\pm$ 3%	$\pm$ 2%
Systematics	$\pm$ 7%	$\pm$ 10%	$\pm$ 7%
Luminosity	$\pm$ 8%	$\pm$ 8%	—

Table 9.2: Sources of errors for the W and Z cross-section calculations and the error after the cancelation in the ratio. The systematic error is the quadratic sum of the five terms listed above in the table, but does not include the luminosity error.

We compare the results of this analysis with other analyses in the DØ experiment and theory (the errors quoted are statistical errors, systematic errors, and – for cross sections only – the luminosity errors):

1. This analysis (RUN1B, DØ, μ):

   - $\sigma_W \cdot Br(W \to \mu\nu) = 2.283 \pm 0.038 \pm 0.161 \pm 0.194$ nb
   - $\sigma_Z \cdot Br(Z \to \mu\mu) = 0.198 \pm 0.014 \pm 0.020 \pm 0.016$ nb

- $R = 11.55 \pm 0.87 \pm 0.81$

2. RUN1A, DØ, μ [76]:

   - $\sigma_W \cdot Br(W \to \mu\nu) = 2.09 \pm 0.06 \pm 0.22 \pm 0.11$ nb
   - $\sigma_Z \cdot Br(Z \to \mu\mu) = 0.178 \pm 0.022 \pm .021 \pm .010$ nb
   - $R = 11.8^{+1.8}_{-1.4} \pm 1.1$

3. RUN1B, DØ, e [77]:

   - $\sigma_W \cdot Br(W \to e\nu) = 2.38 \pm 0.01 \pm 0.09 \pm 0.20$ nb
   - $\sigma_Z \cdot Br(Z \to ee) = 0.235 \pm .003 \pm .005 \pm .020$ nb
   - $R = 10.12 \pm 0.14 \pm 0.42$

4. RUN1A, DØ, e [76]:

   - $\sigma_W \cdot Br(W \to e\nu) = 2.36 \pm 0.02 \pm 0.07 \pm 0.13$ nb
   - $\sigma_Z \cdot Br(Z \to ee) = 0.218 \pm .008 \pm .008 \pm .012$ nb
   - $R = 10.82 \pm 0.41 \pm 0.30$

5. The Standard Model prediction[76]:

   - $\sigma_W \cdot Br(W \to l\nu) = 2.42^{+0.13}_{-0.11}$ nb
   - $\sigma_Z \cdot Br(Z \to ll) = 0.226^{+0.011}_{-0.009}$ nb

The measurements are consistent with each other and the Standard Model prediction within the errors quoted.

9.3 $\Gamma(W)$

As discussed in Chapter 1, using the branching ratio $\Gamma(Z \to \mu\mu)/\Gamma(Z) = (3.367 \pm 0.006)\%$ [11] and the theoretical calculation of $\sigma_W/\sigma_Z = 3.33 \pm 0.03$ [17] where the error is due to the variations in the pdf chosen and the uncertainty in the W mass), we find

$$\Gamma(W \to \mu\nu)/\Gamma(W) \quad = \quad (11.68 \pm 0.49)\%$$

Combining this result with a Standard Model calculation of the partial width $\Gamma(W \to \mu\nu) = 225.2 \pm 1.5$ MeV[26], we obtain

$$\Gamma(W) = 1.93 \pm 0.20 \text{ GeV}$$

Comparing our result with the Standard Model prediction

$$\Gamma(W) \quad = \quad 2.077 \pm 0.014 GeV \quad [26]$$

we can set an upper limit of 307 MeV on the contribution of unexpected decays to $\Gamma(W)$ at 95% confidence level.

9.4 Lepton Universality

To compare the measured W cross sections in the muon and electron channel at DØ, we note that the two results have common errors which will cancel out when we calculate the ratio of the two: the luminosity error (due

to the common error of the Level 0 constant) and the errors due to parton distribution functions. The other errors are independent: the statistical errors, the systematic errors of the efficiencies (they are independently measured from different data. Although there are still some correlated errors because both analyses rely heavily on the CDC, we ignore them to be conservative). Below we list the results and the corresponding errors: (the errors quoted are statistical, independent systematic, common systematic, and luminosity errors) [77]:

$$\begin{aligned}
\sigma_W \cdot Br(W \to \mu\nu) &= (2.283 \pm 0.038 \pm 0.160 \pm 0.031 \pm 0.194) \text{ nb} \\
\sigma_W \cdot Br(W \to e\nu) &= (2.38 \pm 0.01 \pm 0.087 \pm 0.024 \pm 0.20) \text{ nb}
\end{aligned}$$

The ratio is then (the errors quoted are statistical, systematic errors)

$$\frac{\sigma_W \cdot Br(W \to \mu\nu)}{\sigma_W \cdot Br(W \to e\nu)} = 0.959 \pm 0.016 \pm 0.076$$

As discussed in Chapter 1, the ratio of the W-lepton coupling constants is then

$$\frac{g_\mu}{g_e} = 0.979 \pm 0.008 \pm 0.039$$

which is consistent with lepton universality statement that $g_\mu/g_e = 1$.

9.5 Conclusion

We have described the $W \to \mu\nu$ and $Z \to \mu\mu$ cross-section analysis for Run 1B (1994-1995) in the DØ experiment. The sample corresponds to a total integrated luminosity of 38.3pb^{-1}. The results are:

$$\begin{aligned}
\sigma_W \cdot Br(W \to \mu\nu) &= 2.283 \pm 0.038(stat) \pm 0.160(syst) \pm 0.194(lum) \text{ nb} \\
\sigma_Z \cdot Br(Z \to \mu\mu) &= 0.198 \pm 0.014(stat) \pm 0.020(syst) \pm 0.016(lum) \text{ nb} \\
R &= 11.55 \pm 0.87(stat) \pm 0.81(syst)
\end{aligned}$$

Using Standard Model inputs, we further find

$$\begin{aligned}
\Gamma(W \to \mu\nu)/\Gamma(W) &= (11.68 \pm 0.49)\% \\
\Gamma(W) &= 1.93 \pm 0.20 \text{ GeV}
\end{aligned}$$

This enables us to set an upper limit of 307 MeV on the contribution of the unexpected decays to $\Gamma(W)$ at 95% confidence level.

By comparing our results with the $\sigma_W \cdot Br(W \to e\nu)$ measurement at DØ, we find

$$\frac{g_\mu}{g_e} = 0.979 \pm 0.008 \pm 0.039$$

which is consistent with the lepton universality statement that $g_\mu/g_e = 1$.

Appendix A

A Note on Least Square Fit

When we use a Least Square fit to find the value of a quantity, we often want to know which of the input measurements is the most important and deserves the most attention, especially when resources are limited. This appendix briefly discusses this problem, while the full discussion can be found in reference [43].

A.1 The Problem

We first introduce some standard notation in a Least Square fit. Let the N measurements and their errors be $y_1, y_2, \cdots, y_N$ and $\sigma_1, \sigma_2, \cdots, \sigma_N$. Let the fitting parameters be $\theta_1, \theta_2, \cdots, \theta_L (L \leq N)$. To make the expressions short, we introduce matrix notation:

$$y \equiv \begin{pmatrix} y_1 \\ y_2 \\ \vdots \\ y_N \end{pmatrix}, \; V_y \equiv \begin{pmatrix} {\sigma_1}^2 & 0 & \dots & 0 \\ 0 & {\sigma_2}^2 & \dots & 0 \\ \vdots & \vdots & \ddots & \vdots \\ 0 & 0 & \dots & {\sigma_N}^2 \end{pmatrix}, \; \theta \equiv \begin{pmatrix} \theta_1 \\ \theta_2 \\ \vdots \\ \theta_L \end{pmatrix}$$

The fitted variables y_{fit} are related to θ by an $N \times L$ matrix A:

$$y_{fit} \equiv \begin{pmatrix} y_{fit1} \\ y_{fit2} \\ \vdots \\ y_{fitN} \end{pmatrix} = \begin{pmatrix} A_{11} & A_{12} & \dots & A_{1L} \\ A_{21} & A_{22} & \dots & A_{2L} \\ \vdots & \vdots & \ddots & \vdots \\ A_{N1} & A_{N2} & \dots & A_{NL} \end{pmatrix} \begin{pmatrix} \theta_1 \\ \theta_2 \\ \vdots \\ \theta_L \end{pmatrix} \equiv A\theta$$

The Least Square fit finds θ which minimizes $\chi^2 = (y - A\theta)^T {V_y}^{-1} (y - A\theta)$. It can be shown that the desired θ is (V_θ is the error matrix of θ):

$$\begin{aligned} \theta &= \left(A^T V_y^{-1} A\right)^{-1} A^T V_y^{-1} y \\ V_\theta &= \left(A^T V_y^{-1} A\right)^{-1} \end{aligned}$$

With the notation above, the original problem can be stated as:

Suppose we want to improve our result on θ_1. Which of the $\sigma_1, \sigma_2, \cdots, \sigma_N$ does the error σ_{θ_1} most sensitively depend on?

The next section lists the steps to sovle the above problem. The reasons behind the steps are discussed in [43], which also presents the solution to the problem in the more general case (in which we want to improve our result on $\phi = a_1\theta_1 + a_2\theta_2 + \ldots + a_L\theta_L$, where $a_1, a_2, \ldots, a_L$ are given constants, instead of θ_1).

A.2 The Solution

Follow these steps to find N "widths" $w_1, w_2, \cdots, w_N$ for θ_1. The most important measurement for θ_1 is the measurement corresponding to the smallest width in the sense that σ_{θ_1} is most sensitive on the improvement of that measurement.

1. Calculate $V_\theta = (A^T V_y^{-1} A)^{-1}$.

2. Find an orthogonal matrix C so that $V_\eta \equiv C^T V_\theta C$ is a diagonal matrix. This can be done with these steps:

   (a) Find the eigenvalues $\lambda_1, \lambda_1, \cdots, \lambda_L$ of V_θ and their corresponding eigenvectors $X_1 = \begin{pmatrix} x_{11} \\ x_{21} \\ \vdots \\ x_{L1} \end{pmatrix}, X_2 = \begin{pmatrix} x_{12} \\ x_{22} \\ \vdots \\ x_{L2} \end{pmatrix}, \cdots, X_L = \begin{pmatrix} x_{1L} \\ x_{2L} \\ \vdots \\ x_{LL} \end{pmatrix}$, so that

   $$V_\theta X_i = \lambda_i X_i, \qquad X_i^T X_j = \delta_{ij} \qquad \text{where } i, j = 1, 2, \cdots, L$$

   (b) Let

   $$C = (X_1, X_2, \cdots, X_L) \equiv \begin{pmatrix} x_{11} & x_{12} & \cdots & x_{1L} \\ x_{21} & x_{22} & \cdots & x_{2L} \\ \vdots & \vdots & \ddots & \vdots \\ x_{L1} & x_{L2} & \cdots & x_{LL} \end{pmatrix}$$

   Obviously $C^{-1} = C^T$. And

$$
\begin{aligned}
V_\eta &= C^T V_\theta C \\
&= \begin{pmatrix} \lambda_1 & 0 & \dots & 0 \\ 0 & \lambda_2 & \dots & 0 \\ \vdots & \vdots & \ddots & \vdots \\ 0 & 0 & \dots & \lambda_L \end{pmatrix}
\end{aligned}
$$

3. Define $\eta \equiv C^T\theta$ (therefore $\theta = C\eta$).

   Express θ_1 in η:

$$
\begin{aligned}
\theta_1 &= (1, 0, \cdots, 0)\theta \\
&= a'\eta, \qquad \text{where } a' \equiv \begin{pmatrix} a'_1 \\ a'_2 \\ \vdots \\ a'_N \end{pmatrix} = (1, 0, \cdots, 0)C
\end{aligned}
$$

   (in the general case when we are intersted in $\phi = a_1\theta_1 + a_2\theta_2 + \ldots + a_L\theta_L$ instead of θ_1, we need to replace $(1, 0, \cdots, 0)$ by $(a_1, a_2, \cdots, a_L)$.)

4. The widths are ($i = 1, 2, \cdots, N$):

$$
w_i = \frac{\sigma_i}{\sum_{l=1}^{L} (ACV_\eta^{1/2})_{il} a'_l \lambda_l^{\frac{1}{2}}}
$$

It is very straightforward to write a computer program to carry out those calculations [44].

The idea behind the above steps is to transform the L fitted parameters in the θ space (change the base vectors from θ to η), so that two goals are

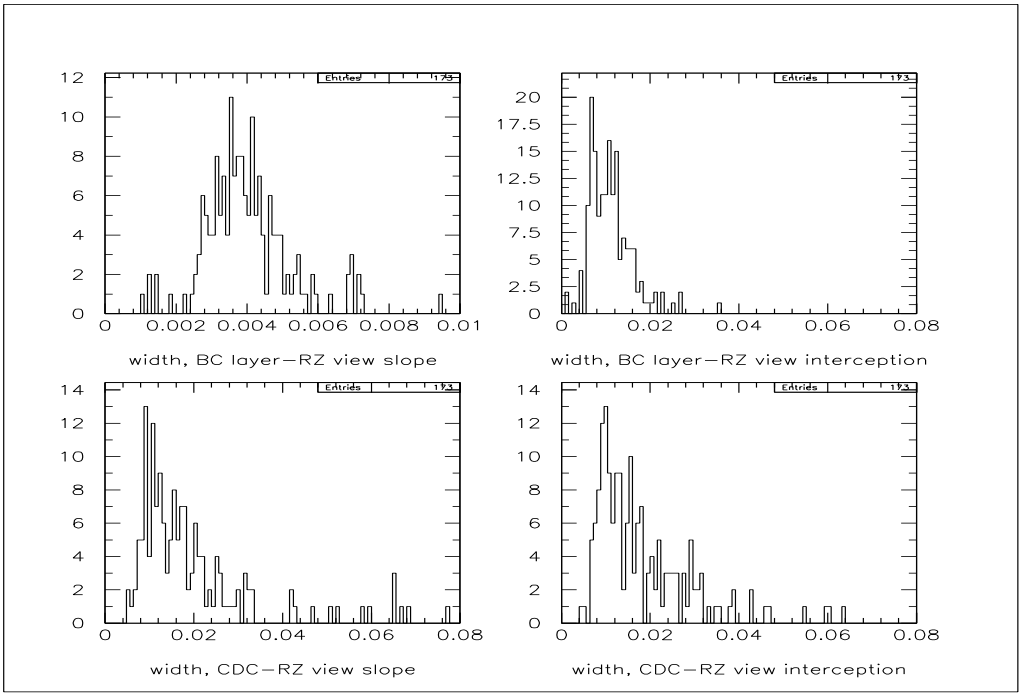

Figure A.1: The width (w_i) distributions for the parameters with the four smallest width for the muon global fit (momentum determination). Note the first plot has a different scale.

achieved: 1) θ_1 is one of the L base vectors; 2) the error matrix corresponding to the new base vector set η is diagonal. Then the relationship between measurements and base vector set becomes very simple, and the original problem can be solved [45].

Applying the method above to the muon global fit (see Chapter 3), we find that, for $1/p$, the bend view slope in the BC layer is most important.

Bibliography

[1] S.L. Glashow, "Partial Symmetries of Weak Interactions", Nucl. Phys. **B 22**, 579-588 (1961).

[2] S. Weinberg, "A Model of Leptons", Phys. Rev. Lett. **19**, 1264-1266 (1967).

[3] A. Salam, "Elementary Particle Physics", ed. by N. Svarthold (Almqvist and Wiksells, Stockholm, 1968), page 368.

[4] R. Cahn and G. Goldhaber, *The Experimental Foundations of Particle Physics*, (Cambridge University Press, New York, 1989 p. 379.

[5] UA1 Collaboration, *Phys. Lett.*, **122B**, p. 103 (1983)

[6] UA2 Collaboration, *Phys. Lett.*, **122B**, p. 476 (1983)

[7] UA1 Collaboration, *Phys. Lett.*, **126B**, p. 398 (1983)

[8] UA2 Collaboration, *Phys. Lett.*, **129B**, p. 130 (1983)

[9] F. Abe *et al.*, "Observation of Top Quark Production in $\bar{p}p$ Collisions", FERMILAB-PUB-95/022-E.

[10] S. Abachi *et al.*, "Observation of the Top Quark", Phys. Rev. Letters **74** 2632 (1995), FERMILAB PUB-95/028-E.

[11] Particle Data Group, Phys. Rev. **D50**, 1173 (1994).

[12] I. Aitchison, A. Hey, "Gauge Theories in Particle Physics", Adam Hilger, 1989.

[13] S.D. Drell and T.M. Yan, Phys. Rev. Lett. **25** 316 (1970).

[14] E.L. Berger, F. Halzen, C.S. Kim, S. Willenbrock, "Weak Boson Production at Fermilab Tevatron Energies", Phys. Rev. D **40** 83-91 (1989).

[15] CERN WWW home page: http://www.cern.ch/

[16] CERN Press Release: http://www.cern.ch/Press/Releases96/PR05.96ELEP2StartUp.html

[17] R. Hamberg, W.L. van Neerven and T. Matsuura, Nucl. Phys. **B359**, 343 (1991).

[18] W. L. van Neerven and E. B. Zijlstra, Nucl. Phys. **B382**, 11(1992).

[19] H.L. Lai *et al.*, Phys. Rev. **D51**, 4763 (1995);

[20] We used $M_W = 80.23 \pm 0.18$ GeV/c^2 from DØ Note 2115/CDF Note 2552, 1994 (unpublished).

[21] V. Barger and R. Phillips, "Collider Physics", 1987.

[22] A.D. Martin, R.G. Roberts and W.J. Stirling, "Parton Distributions Updated", Phys. Lett. **B306**, 145(1993); **B309**, 492(E)(1993).

[23] A.D. Martin, R.G. Roberts and W.J. Stirling, "Parton Distributions of the Proton", Rutherford Appleton Laboratory Preprint RAL-94-055, June 1994.

[24] V. Barger *et al.*, Phys. Rev. **D28**, 2912 (1983); M. Drees, C.S. Kim and X. Tata, Phys. Rev. **D37**, 784 (1988).

[25] T. Alvarez, A. Leites and J. Terrón, Nucl. Phys. **B301**, 1 (1988).

[26] J.L. Rosner, M.P. Worah and T. Takeuchi, Phys. Rev. **D49**, 1363 (1994).

[27] J. L. Rosner, M. P. Worah and T. Takeuchi, Enrico Fermi Institute preprint EFI-93-40(1993).

[28] F. Abe *et al.*, Phys. Rev. Lett 74 341 (1995). The result is $\Gamma(W) = 2.11 \pm 0.32$ GeV.

[29] S. Lami, Darien Wood, DØ note 1462, 1992.

[30] R.R. Wilson, "The Tevatron", Phys. Today **10**, 23-30 (1977).

[31] DØ Collaboration, S. Abachi *et al.*, Nucl. Instrum. Methods **A338**, 185 (1994).

[32] F. Sauli, "Principles of Operation of Multiwire Proportional and Drift Chambers", Addison-Wesley, Menlo Park, 1987.

[33] Konrad Kleinknecht, "Detectors for Particle Radiation", Cambridge University Press, 1987.

[34] Ryuji Yamada *et al.*, DØ Note 2023, 1994.

[35] Haowei Xu, "Search for the Top Quark in the Electron + Jets + Soft Muon Channel at DØ", PhD thesis, Brown University, 1996.

[36] William Joseph Thompson, "Search for the Top Quark in the Muon + Jets Channel at DØ", PhD thesis, SUNY at Stony Brook, 1994.

[37] Scott Stuart Snyder,"Measurement of the Top Quark Mass at DØ", PhD thesis, SUNY at Stony Brook, 1995.

[38] P. Martin, "Muon PDT Layout", DØ Note 416, 1986.

[39] Private communication with Darien Wood. This is for the DØ RECO version 12. The last term was $(0.01p[GeV/c])^2$ for the DØ RECO version 11. A DØ note is in preparation.

[40] C. Brown *et al.*, Nucl. Instrum. Methods **A279**, 331-338 (1989).

[41] Myungyun Pang, "Search for Top in $p\bar{p}$ Collisions at $\sqrt{s}$ = 1.8TeV by Constrained Kinematic Fitting", PhD thesis, Iowa State University, 1994.

[42] D. Hedin, "Muon Reconstruction Program", DØ Note 1325 (1992).

[43] Ting Hu, "How to Find the Most Important Measurement in Least-Square Fits, and Its Application in the Muon Momentum Determination

at DØ", DØ Note 1811 (1993)

(URL: http://d0sgi0.fnal.gov/d0notes/note1811)

[44] See d0sb15::usr$root3:[tinghu]widths_finder.for for a sample subroutine in Fortran. The central part of this program is a routine(from CERN library) which finds eigenvalues and eigenstates of a given matrix.

[45] Professor Tom Trippe(LBL) pointed out this relationship to me. I worked out the transformation part and the solution in the general case.

[46] M. Paterno, "A Study of the DØ Calorimeter $\not{E}_T$ Resolution Using Low E_T Jet Triggers", DØ Note 1782 (1993).

[47] N. Amos *et al.* , "A Luminosity-Independent Measurement of the $p\bar{p}$ Total Cross Section at $\sqrt{s} = 1.8$ TeV, Phys. Lett. **B 243**, 158(1990).

[48] F. Abe *et al.* , "Measurement of the $p\bar{p}$ Total Cross Section at $\sqrt{s} = 546$ and 1800 GeV, Phys. Rev. **D 50**, 5550 (1994).

[49] F. Abe *et al.* , "Measurement of Small Angle $p\bar{p}$ Elastic Scattering at $\sqrt{s} = 546$ and 1800 GeV, Phys. Rev. **D 50**, 5518 (1994).

[50] F. Abe *et al.* , "Measurement of the $p\bar{p}$ Single Diffractive Dissociation at $\sqrt{s} = 546$ and 1800 GeV, Phys. Rev. **D 50**, 5535 (1994).

[51] N. Amos *et al.*, "Luminosity Calculation for DØ", DØ Note 2031, 1994.

[52] J. Bantly *et al.*, "Improvement to the DØ Luminosity Monitor Constant", DØ Note 2544, 1995.

[53] F. Paige and S. Protopopescu, "ISAJET 6.49: A Monte Carlo Event Generator for pp and $\bar{p}p$ Interactions", FermiLab Computing Division, PM0059 (August 1992).

[54] H. Bengtsson and T.Sjöstrand, "PYTHIA, The Lund Monte Carlo for Hadronic Processes", Proceedings of Snowmass '86, p.311 (1986).

[55] G. Marchesini, et. al., "HERWIG: Version 5.1", Cavendish-Hep-91-26, May 1991.

[56] G. Fox and S. Wolfram, Nucl. Phys. B, 168, 285 (1980).

[57] Private communication with Paul Quintas. A DØ note is in preparation. The link between the Monte Carlo simulation and the data here is via the acceptance contribution due to the chamber inefficiencies, which are the dominant (see Table 5.1).

[58] Paul Quintas, Darien Wood,"Muon Calibration Procedures for T_0 and ΔT Constants in RUN 1A", DØ note 2103, 1994.

[59] Thorsten Bernhard Huehn, "A Measurement of Bottom Quark Production in $p\bar{p}$ Collisions at $\sqrt{s} = 1.8$TeV", PhD thesis, 1995.

[60] DØ Collaboration, S. Abachi *et al.*, "Inclusive mu and b-Quark Production Cross Sections in pbarp Collisions at $\sqrt{s} = 1.8$TeV", Phys. Rev. Letters 74 3548 (1995).

[61] Cecilia Gerber, Paul Quintas, "Muon Momentum Resolution from DØ Reco v10", DØ note 1985, 1993.

[62] F. Abe *et al.*, "The Charge Asymmetry in W-Boson Decays Produced in $p\bar{p}$ Collisions at $\sqrt{s} = 1.8$ TeV", Phys. Rev. Lett (1994).

[63] Ian, Adam, Eric Flattum *et al.*, DØ Electroweak Workshop at LBL, 1996.

[64] Private communication with Eric Flattum.

[65] Elizabeth Gallas, "The MTC Package", DØ Note 2066, 1994.

[66] Elizabeth Gallas *et al.*, "Testing MTC", DØ Note 2068, 1994.

[67] The online documents can be found on the FNALD0 cluster, TMP$ROOT228:[HEDIN.STA]CFSCAN.DOC and EFSCAN.DOC.

[68] Paul Z. Quintas, "Reconstruction and Selection Efficiencies for High p_T Muons in Run 1B", DØ Note 2865, 1996.

[69] Ting Hu, "Statistics of Tossing Coins", DØ Note 2406, 1994.
(URL: http://d0sgi0.fnal.gov/d0notes/note2406)

[70] Jeffrey Bantly, Qizhong Li-Demarteau, "Multiple Interaction Tool", DØ Note 1691, 1993.

[71] Jeffrey Bantly,"Multiple Interaction Tool Study", DØ Note 1849, 1993.

[72] Ting Hu, Paul Z. Quintas, "$W \to \mu\nu$ and $Z \to \mu\mu$ Cross-sections in Run 1B at DØ", DØ Note 2956(in preparation), 1996.

[73] Tom Marshall, Herman Haggerty, "Crud Removal From Muon Drift Chamber Wires Using "ZAP" Cleaning", DØ Note 2556, 1995.

[74] For an example fortran program for this calculation, see (on DØ ALpha cluster) USR$ROOT1:[QUINTAS.WZ.XSEC]SIMPLE5.FOR.

[75] Paul Z. Quintas, "Trigger Efficiency for $W \to \mu\nu$ in Run 1B", DØ Note 2712, 1995.

[76] DØ Collaboration, S. Abachi *et al.*, "W and Z Production in $p\bar{p}$ Collisions at $\sqrt{s} = 1.8$ TeV", Phys. Rev. Lett. **75**, 1456-1461, 1995.

[77] Paul Z. Quintas, "W and Z Production Cross Sections at DØ", XI Topical Workshop on $p\bar{p}$ Collider Physics, 1996.